Performance of OFDM and DFT-s-OFDM in the THz-Band Communications Channels

by

Erfan Khorram
B.Sc., University of Tehran, Iran, 2018

A Thesis Submitted in Partial Fulfillment of the
Requirements for the Degree of

MASTER OF APPLIED SCIENCE

in the Department of Electrical and Computer Engineering

Performance of OFDM and DFT-s-OFDM in the THz-Band Communications Channels

by

Erfan Khorram

B.Sc., University of Tehran, Iran, 2018

Supervisory Committee

Dr. Xiaodai Dong, Supervisor

(Department of Electrical and Computer Engineering)

Dr. Lin Cai, Departmental Member

(Department of Electrical and Computer Engineering)

Supervisory Committee

Dr. Xiaodai Dong, Supervisor

(Department of Electrical and Computer Engineering)

Dr. Lin Cai, Departmental Member

(Department of Electrical and Computer Engineering)

Abstract

The terahertz (THz) band is a promising frequency band that ranges from 300 GHz to 10 THz and being considered for the next generation of wireless networks due to the large available bandwidth and achievable ultra fast data rates. The first step in studying every wireless system is to accurately characterize the propagation channel. Therefore, in this thesis, a channel model is proposed with unique terahertz propagation characteristics that can be used to study candidate waveforms in the THz band. The next step is to study the candidate waveform designs. In this work, orthogonal frequency-division multiplexing (OFDM) and discrete Fourier transform-spread-OFDM (DFT-s-OFDM) are examined waveform candidates in the THz band. As OFDM is widely used in industry and thoroughly studied in the past couple of decades, it can be used as a benchmark for multi-carrier waveform designs. This study helps us to understand if OFDM can still be a reliable waveform in higher frequencies and how it compares with single carrier DFT-s-OFDM.

In the first part of the thesis, the multi-ray communication channel is modeled based on ray tracing methods which consists of line-of-sight (LoS), reflected, and scattered paths. This model is a modified version of an existing multi-ray channel model with improvement. The coded OFDM and DFT-s-OFDM systems are studied by simulation in terms of spectral efficiency, CP length, peak-to-average power ratio (PAPR), phase noise, etc. DFT-s-OFDM is shown to possess advantages over OFDM in scattering rich THz channels with better PAPR, error performance and tolerance to phase noise, making it a preferred candidate over OFDM.

Contents

List of Figures

List of Tables

Acknowledgments

I extend my deepest gratitude to my supervisor, Prof. Xiaodai Dong, for providing me with the exceptional opportunity to work under their supervision and for their outstanding mentorship, consistent guidance, and expert insights throughout the research process. Their priceless feedback and unwavering encouragement have played a pivotal role in shaping this thesis. I would also like to thank Prof. Lin Cai for her interest in my research, valuable guidance, and insightful feedback.

I would also like to thank all current and former members of Dr. Dong's Lab for their true friendship and support since day one of starting my journey at UVic. Their contributions and company have been truly appreciated.

I cannot thank my family enough for their precious love, support, and continuous encouragement, without which this achievement would have not been possible.

Dedication

To my mother and father

Chapter 1

Introduction

1.1 Terahertz

Over the past decade, the need for more bandwidth and higher data rate in wireless communication systems have increased drastically. One of the ways to address this challenge is to use higher frequencies. As a result, frequencies from 300 GHz to 1 THz are gaining more attention among researchers because of the wide unused spectrum. Moreover, these frequencies will help to open the doors to a new world of revolutionary applications that can benefit from the high carrier frequencies.

The frequency band from 30 GHz to 300 GHz is used in 5G wireless communication systems to address the spectrum shortage that is a limiting factor in 4G cellular communication systems which use the frequency band of below 6 GHz [7]. On the other hand, there are new applications such as virtual reality, self-driving cars, internet of things (IoT), and wireless backhaul will need much greater data rates than that of 5G communication systems [8], [9].

With the currently known digital modulation methods and hardware components used in transceivers, there is a limit on the symbol duration and achievable spectral efficiency. As of today, there is approximately 7 GHz of bandwidth available within the unlicensed wireless band of 60 GHz [10] which enables us to achieve data rates of 100 Gigabits per second (Gbps) if the spectral efficiency of a transmission scheme is at least 14 bit/s/Hz [1] which is below what is achievable considering the hardware

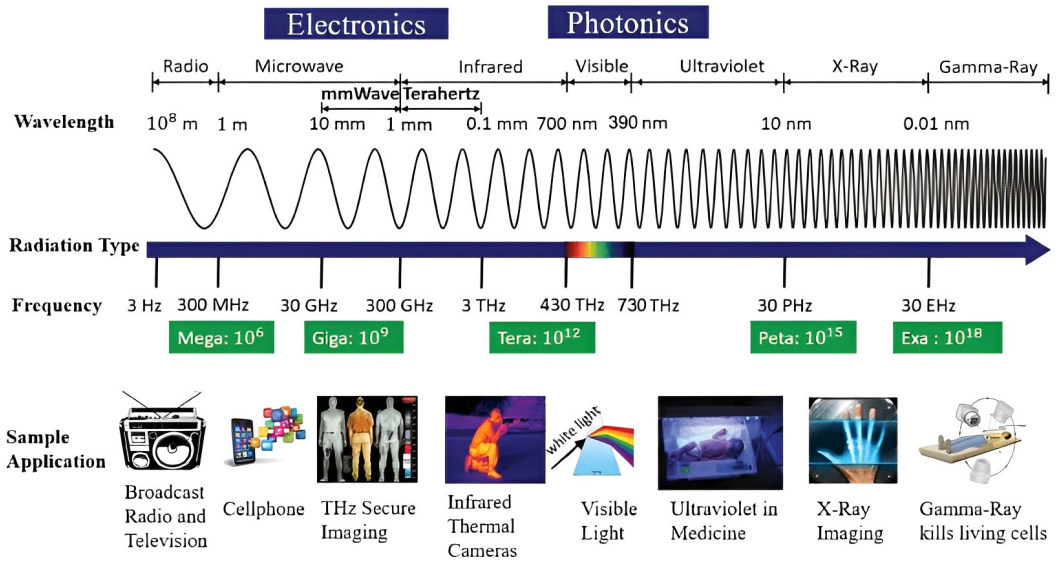

Figure 1-1: Examples of various applications for the electromagnetic spectrum as a function of frequency [1].

constraints [11], [12], and [13]. Hence, to achieve data rates on the order 100 Gbps, the frequencies above 100 GHz will be used where the availability of the spectrum is not an issue [14].

Figure 1-1 from [1] shows some examples of various applications and their relative frequency bands of operation. It also shows that THz frequencies are well below the visible light frequencies. Frequencies above visible light frequencies such as optical frequencies are not considered safe enough due to eye-safety limits to be used in wireless communication systems [15]. Moreover, there are a number of issues such as the "impact of atmospheric and water absorption on the signal propagation" [1], the ambient light noise due to sunlight and artificial lights, and high amount of diffuse scattering on rough surfaces that make these frequencies even less attractive for wireless communication systems [15]. Ultraviolet, X-Ray, and Gamma-Ray frequencies are known to have really high particle energy which can create free-radicals that can be a cause of cancer [16]. On the other hand, mmWave and THz radiation are not ionizing due to the low photon energy which is around 0.1 to 12.4 meV, and these levels of energy are more than three orders of magnitude less than ionizing photon energy levels. The typical level of photon energy required for ionization is around 12 eV [16] and [1].

Therefore, THz radiation does not impose health threats in terms of ionization which leaves heating to be the only main cancer risk [16]. To address the heating concern and its effect on human body, the Federal Communications Commission (FCC) and the International Commission on Non-Ionizing Radiation protection (ICNIRP) standards [17], [18] are designed to protect against these hazards particularly on parts of body that are most sensitive to heat from radiation.

The short wavelength at THz frequencies will not only allow high data rates of more than 100 Gbps, but also enable huge spatial multiplexing that can be used in hub and backhaul communications, super accurate sensing, imaging, and many more applications described in [19] - [20]. It can also be used in the military as it provides secure communication over highly sensitive links. This is possible because the THz band frequencies have very small wavelengths that enable very high gain antennas to be made in small physical dimensions [21].

1.2 Applications

As THz frequencies provide ultra-high data rates, they can be used for ultra-fast download speeds, autonomous vehicles, information shower [22], robotic controls, high-definition (HD) holographic gaming, and high-speed wireless communication in data centers [15]. Moreover, there are some other promising applications that are expected to evolve in 6^{th}-generation (6G) cellular networks. These applications fall into five main categories such as wireless cognition, sensing, imaging, wireless communication, and positioning [1].

1.2.1 Wireless Cognition

In some applications such as controlling a fleet of drones, it is likely that the drone itself may be super lightweight and small and as a result there is only limited hardware capabilities and power budget on the device. Therefore, conducting massive computations for highly complex tasks such as contextual awareness, vision, and perception may not be feasible on the device. In this situation, a wide channel bandwidth com-

bined with a super fast data rate can enable all those computations to be carried out on a fixed base station that is connected in real time to the drone fleet via a wireless link. This is just an example of the wireless cognition concept which means providing a wireless/remote communication link for devices that need massive computations [1]. Similarly, robots, autonomous vehicles, and other machines can benefit from this fast, secure, and reliable communication link to conduct the complex computations remotely [1]. This will relax design constraints of those machines and robots as power budget can be a limiting factor in designing such systems.

Moore's law says that the number of transistors in a dense integrated circuit (IC) doubles approximately every two years [23]. Based on this law and the observations in [24] and [25], it can be seen that by the year 2036 there will be devices that cost as low as 1000 USD that will be able to have computational capabilities on the order of the human brain. The following analysis from [1] shows that wireless remoting of human cognition will be feasible using Terahertz frequencies.

The human brain consists of about 100 billion (10^{11}) neurons that each has an update rate of 5 ms, and each neuron is connected to around 1000 other neurons which means that the computation speed of the human brain is approximately 20×10^{15} floating point operations per second (flops) [24], [25], [1], assuming that each operation is binary, the required data rate is calculated to be around 20,000 Terabits per second (Tbps):

Human brain computation speed =

$$20 \times 10^{15} \text{ flop/sec} = 20 \times 10^{15} \text{ flop/sec} \times 1 \text{ bit/flop} = 20,000 \text{ Tbps}. \tag{1.1}$$

Now, the storage can be calculated considering that each neuron can write to 1000 bytes as shown in [24], [25], [1]:

$$\text{Storage} = 10^{11} \text{ neurons} \times 10^{3} \text{ bytes/neuron} = 100 \text{ TB}. \tag{1.2}$$

Today's high-end 1000 USD devices can perform around 10^{12} computations per second. This value is four orders of magnitude less than the human brain speed

calculated in Eq. (1.1). It is anticipated that future wireless generations will allocate up to 10 GHz radio frequency (RF) channels for each user in the THz regime. If each user uses a digital modulation that has an order of at least 10 bits/symbol and the channel capacity increases by 1000 times, then it can be seen from Eq. (1.3) that data rates of at least 100 Terabytes per second (TBps) are achievable [1]:

$$R = 10 \text{ GHz channel} \times 10 \text{ bits}/(\text{sec . Hz}) \times 10^3 = 100 \text{ TBps}. \tag{1.3}$$

From Eq. (1.1)-(1.3), it can be seen that a 10 GHz channel bandwidth will enable $100/20,000 = 0.5\%$ of real time brain computational capacities. This computational capacity will increase linearly by increasing the channel bandwidth.

1.2.2 Sensing

Sensing applications will benefit from the sub-mm wavelength of THz frequencies and the frequency selectivity of the environment which they are measuring to gain knowledge about the environment. Those sensing applications that require very directional antennas can benefit from the fact that THz frequencies will enable the production of high gain antennas in a small physical form. As a result the spatial resolution will become considerably finer as wavelength becomes shorter [1].

One of the exciting examples in this case is creating a detailed 3-D map of a room or a complex environment in a matter of fractions of a second. This is because over the past few years electrical beam steering algorithms have improved a lot and they can be implemented in real time. On the other hand, the propagation times will be in the order of nano-seconds due to short distances in a room or even a more complex area. Hence, near real-time mapping of an environment will be feasible using THz frequencies. This means that future wireless devices will be able to do "wireless reality sensing" [26], [27].

One of the interesting properties of some materials and gasses is that they resonate at particular frequencies because they have vibration absorption at some THz frequencies. This property can be used by future THz devices to detect the presence

of a specific gas in the air or a specific item in a room based on frequency scanning. This means that future smart phones and mobile devices capable of 6G will have the potential to be used to detect the presence of certain gasses in the air, certain chemicals in food or drink, and detect other irregular materials in the world around us [1], [28].

Other sensing applications mentioned in the literature includes very small radars for gesture detection that can be used in touchless smart phones, spectrometers for gas sensing and explosive detection [28], THz body scanners for security reasons, air quality detection [20], precise time/frequency transfer, and wireless synchronization [15], [29], [30].

1.2.3 Imaging

As described in section 1.1, THz channel is less impacted by the ambient light and weather compared to visible light frequency channels. Thus, radar at THz frequencies will be more effective than infrared-based imaging such as Light detection and Ranging (LIDAR). One of the disadvantages of LIDAR is that it cannot be trusted when the weather condition is not ideal or it is foggy, raining, or cloudy [31]. Therefore, its high resolution will not be useful in those situations. On the other hand, THz radar is not affected by the weather, therefore it can be used in autonomous vehicles despite having a lower resolution compared to LIDAR [15], [19].

Another exciting feature that can be added to computer vision is to "view" non-line of sight (NLoS) objects around corners. This will be especially attractive to rescue and surveillance teams as well as researchers in the field of self-driving cars. As some building surfaces such as walls, doors, and floors behave as mirrors to THz radiations, thus NLoS imaging will be possible if there are enough reflection or scattering paths [32], [33]. Although the idea of NLoS imaging is not a new idea and has been exploited based on visible light and infrared light in [34], [35], [36], it is not very practical since it requires very complex hardware and computationally expensive algorithms because the optical wavelength is smaller than the roughness factor of most surfaces for distances below 5 metres (m) [1]. Lower frequencies below 10 GHz also can be

used for NLoS imaging. However, these systems have the disadvantage of not being able to deal with cluttered images due to strong multi-path reflections [37].

Since THz frequencies are higher than that of microwaves and lower than visible light frequencies, it comes to mind that THz waves can combine the advantage points of both of them. Firstly, THz waves have short wavelength and wide bandwidth which enable THz systems to capture high spatial resolution images [38]. Also, most building surfaces act very close to "electrical mirrors" when THz waves are the incident waves to the surfaces. This results in strong specular components that allow efficient NLoS imaging while spatial coherency and high spatial resolution are maintained [33]. The idea here is to illuminate the environment with THz waves and compute the time of flight (ToF) of the back-scattered signals. From there, a distorted 3-D image of the scene can be constructed. The distorted image can be corrected if the LoS surfaces act as mirrors because of the strong specular reflections by using mirroring transformations [32].

Fig. 1-2 and 1-3 from [2] depict the experimental setup and results of

1.2.4 Positioning

Future wireless communication systems operating in the THz band will be able to perform centimetre-level localization. An example of this application is illustrated in Fig. 1-2 and 1-3 from [2] showcasing the experimental setup and the corresponding results, respectively. The experiment clearly shows a very high accuracy even in NLoS scenarios. The setup for this experiment is shown in Fig. 1-2 which consists of the following components. The first one is a synthetic aperture radar (SAR) which has a 13-cm aperture linear antenna and operates in the frequency range between 220 GHz to 300 GHz. The mock-up environment also has two pieces of drywall, one in LoS and the other one in NLoS. There is also a single-antenna user. The localization is done by first constructing a mmWave image of the environment which can be done by rapid beam steering. Then, the user needs to estimate the angle of arrival (AoA) and time of arrival (ToA). This will be done by sending a pilot signal to the base station (BS). The final step is to use AoA and ToA to back-track the path of the

signal sent by the user on the constructed mmWave image in the first step. The user signal here experiences two reflections, however, the localization of the user was done with high accuracy. This method is unique in its own way since it does not need prior knowledge of the environment and it is ready to use without any prior calibration [2].

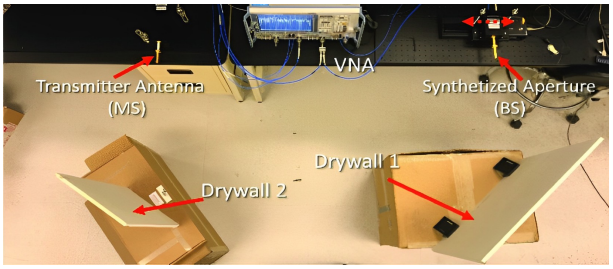

Figure 1-2: Experimental setup for centimeter-level positioning by using mmWave adopted from [2].

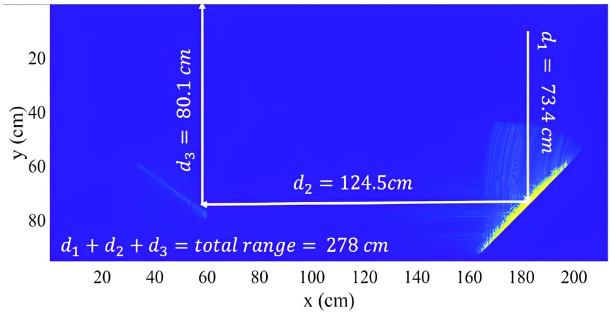

Figure 1-3: The user location is projected on the corrected 2D mmWave image [2].

1.3 Motivation and Contribution

THz channels exhibit unique characteristics due to the diffuse scattering from rough surfaces at THz frequencies, causing incident waves to scatter in random directions. This phenomenon results in highly frequency-selective channels, particularly when the carrier frequency is high and the distance between transmit and receive antennas and reflecting objects is short. Considering this frequency selectivity, it is worth investigating orthogonal frequency division multiplexing (OFDM)-based waveforms, which are widely used in 4G LTE and 5G NR, for THz channels. However, there is a lack of comprehensive studies on OFDM in THz channels with accurate channel

models, as most studies focus on sub-THz channels, which differ from THz channels. Moreover, OFDM is known to have a high peak-to-average power ratio (PAPR), and it is important to compare its performance with other options that have lower PAPR to determine if the higher PAPR is justified. Therefore, this thesis presents a thorough analysis of OFDM and DFT-s-OFDM (which has a lower PAPR compared to OFDM) performance in THz channels, serving as benchmark results for future waveform designs.

Over the past two decades, OFDM has gained significant interest from researchers and industry professionals alike, making it the most widely used signaling method in wireless channels [39]. It has been implemented in a vast array of wireless standards, including various adaptations of IEEE 802.11 and IEEE 802.16, third generation partnership program long-term evolution (3GPP-LTE) and LTE advanced, and 5G cellular communications [40]. Therefore, it is important to study the OFDM technique in an accurate THz channel and validate its performance as one of the potential candidate waveforms to be adopted in 6G cellular networks. However, to this day, a study on the performance and complexity trade-offs of OFDM and the single carrier version of that known as DFT-s-OFDM or pre-coded OFDM in THz channels still lacks in the literature. Both OFDM and DFT-s-OFDM have their own unique advantages and disadvantages. One of the main advantages of OFDM over DFT-s-OFDM is the simple equalization process at the receiver. As it will be discussed in Chapter 4, DFT-s-OFDM requires a minimum mean square error (MMSE) equalizer to have a good bit error rate (BER) performance. On the other hand, DFT-s-OFDM has the advantage of low PAPR compared to OFDM which makes it suitable for uplink transmission where the power is limited [41].

The rest of this thesis is organized as follows. In Chapter 2, a channel model is studied with unique terahertz propagation characteristics that can be used to study candidate waveforms in the THz band. This channel model is obtained based on a combination of ray tracing techniques and statistical methods. Chapter 3 outlines OFDM and DFT-s-OFDM waveforms that are used in the THz channel. Low density parity check (LDPC) coding that is used in 5G NR reviewed alongside with the

parameters that can potentially be used in 6G. Phase noise (PN) as a very important hardware impairment is studied in the same chapter. A phase noise model for THz frequencies is demonstrated. This model can be used to simulate the effect of phase noise on OFDM and DFT-s-OFDM in THz channels. The simulation results are presented in Chapter 4. Channel impulse response (CIR) of several THz channels are presented. A simulation based approach to determine the best cyclic prefix (CP) length is provided. The performance of OFDM and DFT-s-OFDM in terms of BER and block error rate (BLER) is studied. A modified phase noise estimation and compensation method is proposed for both OFDM and DFT-s-OFDM. Finally, Chapter 5 summarises the main conclusions of this thesis.

Chapter 2

THz Channel Model

2.1 Introduction

To analyze wireless communication systems, it is important to have a unified model that can be used in simulations. This model should be accurate enough by characterizing the wireless channel properties to match the measurements. Unlike at lower frequencies below 6 GHz that the propagated wave is mainly attenuated due to the molecular absorption in free space, at higher frequencies, since the wavelength becomes very short and comparable to the size of dust, rain, snow, and other materials in the air, the effect of scattering becomes much more severe [11]. Certain gasses in the atmosphere have resonance frequencies that are in the terahertz range. These gasses include but not limited to oxygen and hydrogen. The resonances of such gases at certain frequency bands will cause a significant absorption loss. This effect is called atmospheric absorption. As shown in Fig. 2-1, the frequency bands of 183 GHz, 325 GHz, 380 GHz, 450 GHz, 550 GHz, and 760 GHz, experience a much greater attenuation in typical air due to the atmospheric absorption in addition to the Friss' free space loss. This effect makes these frequency bands very attractive for very short range and secure wireless communications where the signal attenuates very fast. On the other hand, there are some frequency bands such as frequencies below 300 GHz that do not suffer more than 10 dB/km of additional loss due to atmospheric absorption. These frequency bands have the potential to be used for high speed 6G cellular

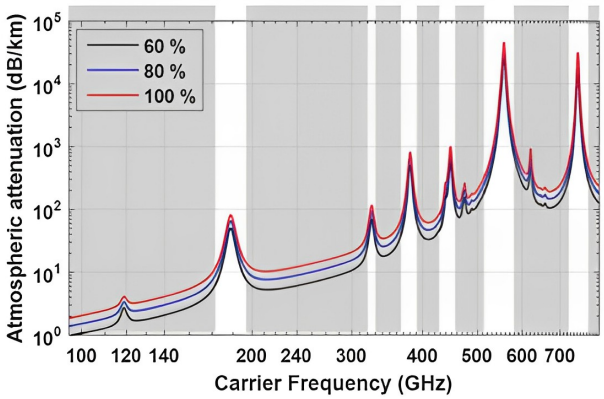

Figure 2-1: Atmospheric absorption versus carrier frequency for different humidity conditions [3].

networks with coverage range of up to several kilometers [7], [1]. The other interesting frequency band ranges from 600 GHz to 800 GHz. The atmospheric absorption in this band is between 100 to 200 dB/km. This means that over a 100 m distance, which is the typical radius of a small cell, the loss will be between 10 to 20 dB. This level of atmospheric absorption will be easily handled by high gain directional antennas, which makes this frequency band very practical for the next generation of cellular networks.

The channel models for lower frequency bands like 60 GHz [42] are not suitable for Terahertz simulations as they do not model the very high molecular and atmospheric absorption or the very high reflection loss. Some existing channel models for the THz band such as [13], [43], [44], [45] are only limited to characterize the multi-path channel at 300 GHz. These models have the advantage of considering the atmospheric absorption of LoS and NLoS rays as well as scattering loss from rough surfaces. One of the disadvantages of these models is that they are based on measurements, which means these models are subject to the specific environment and settings.

In this chapter, a brief overview of the THz band channel model based on ray tracing methods is given. Using this model, the channel characteristics in the THz band such as distance-varying and frequency-selective nature of the THz band channels are analyzed. Additionally, the coherence bandwidth and the importance of the delay spread of the Terahertz channels are studied.

2.2 Multi-Ray Channel Model

In this section, the multi-ray channel model that was developed using ray tracing methods in [46] is introduced. The ray tracing methods are generally optic approaches but as the wavelength in the THz band is very short, we can use ray tracing to accurately model the LoS, reflected, diffusely scattered, and diffracted electromagnetic (EM) waves.

The multi-ray propagation model in the THz band is combined of many individual sub-bands that are considered to be narrow enough to have a flat frequency response. Then, the superposition theory can be used to get the narrow band channel impulse response (CIR) that consists of N_i rays in the m^{th} frequency sub-band. Among those N_m rays, the n^{th} ray will go through an attenuation of $\alpha_{m,n}$ that is frequency-dependent to get to the receiver after a propagation delay of τ_n. Finally, the time-domain CIR for the m^{th} frequency sub-band is given by:

$$h_m(\tau) = \sum_{n=1}^{N_m} \alpha_{m,n} \delta(\tau - \tau_n). \tag{2.1}$$

Different rays that form the multi-ray channel model are LoS, reflected, scattered, and diffracted rays. Fig. 2-2 from [4] shows four scenarios for a ray that can reach to the receiver.

Assuming that the LoS can be either present or not, the indicator $\mathbb{I}_{LoS}$ is equal to 0 if the LoS path is not available, or is equal to 1 if the LoS path does exist. $N_{Ref}^{(m)}$ is the number of reflected rays, $N_{Sca}^{(m)}$ is the number of scattered rays, and $N_{Diff}^{(m)}$ is the number of diffracted rays in the m^{th} frequency sub-band. The channel model in time domain can be written as shown in [4]:

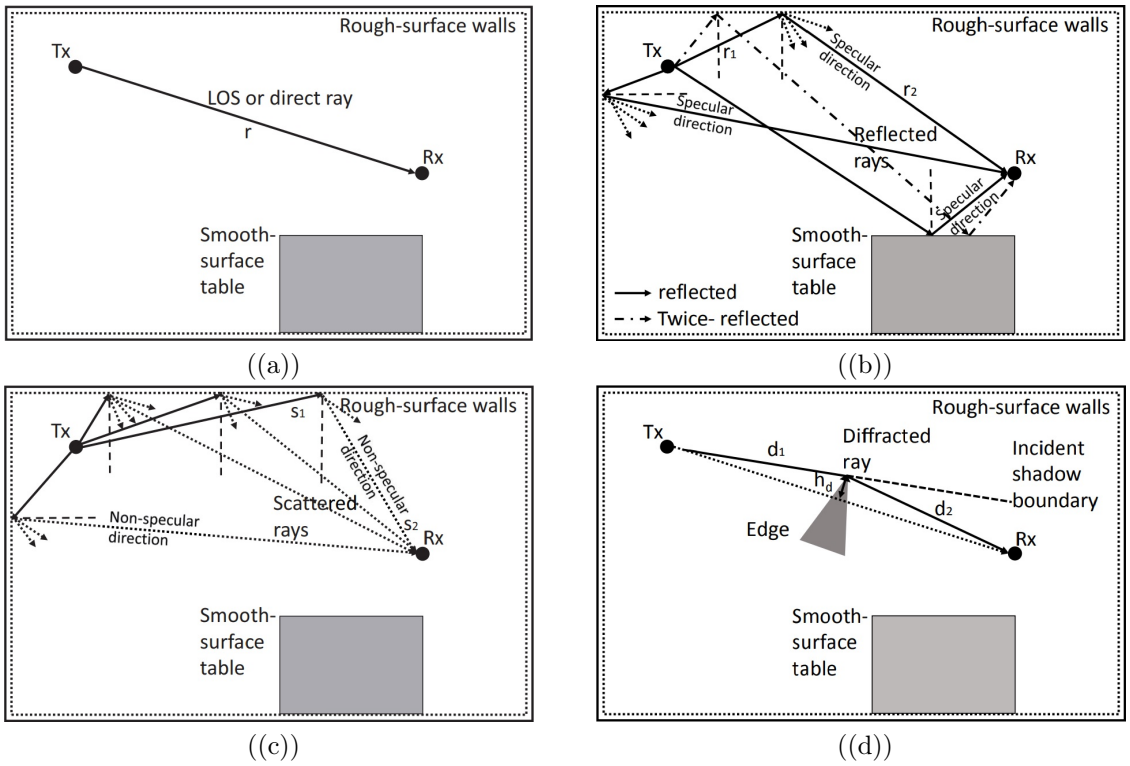

Figure 2-2: Propagation rays between Tx and Rx. (a): LoS ray, (b): Reflected rays, (c): Scattered rays, and (d): Diffracted rays [4].

$$h_m(\tau) = \alpha_{LoS}^{(m)}\delta(\tau - \tau_{LoS})\mathbb{I}_{LoS} + \sum_{l=1}^{N_{Ref}^{(m)}} \alpha_{Ref}^{(m,l)}\delta(\tau - \tau_{Ref}^{(l)}) + \sum_{q=1}^{N_{Sca}^{(m)}} \alpha_{Sca}^{(m,q)}\delta(\tau - \tau_{Sca}^{(q)}) + \sum_{u=1}^{N_{Diff}^{(m)}} \alpha_{Diff}^{(m,u)}\delta(\tau - \tau_{Diff}^{(u)}), \tag{2.2}$$

where $\alpha_{LoS}^{(m)}$ is the attenuation that the LoS ray experiences, and τ_{LoS} is the propagation delay. Similarly, for the l^{th} reflected ray, $\alpha_{Ref}^{(m,l)}$ is the attenuation and $\tau_{Ref}^{(l)}$ is the propagation delay. Finally, for the q^{th} scattered path and u^{th} diffracted path, $\alpha_{Sca}^{(m,q)}$ and $\alpha_{Diff}^{(m,u)}$ are the attenuation coefficients and the propagation delays are expressed as $\tau_{Sca}^{(q)}$ and $\tau_{Diff}^{(u)}$, respectively.

In the next sections, the transfer function of each of the scenarios depicted in Fig. 2-2 in frequency domain is presented. The frequency-domain transfer function, then can be converted to time-domain and using the superposition theory, the channel impulse response in time domain will be given.

2.2.1 Line of Sight (LoS)

The LoS channel transfer function in frequency domain is denoted by H_{LoS} which is made out of two types of losses, namely, the spreading loss and the molecular absorption loss.

The spreading loss, H_{Spr}, is due to the free space path loss that is related to the carrier frequency, f, and the transmission distance, r, between the transmitter (Tx) and the receiver (Rx). This transfer function is given by

$$H_{Spr}(f,r) = \sqrt{2Z_0}\frac{c}{4\pi.f.r}, \tag{2.3}$$

where $Z_0 = 120\pi\ \Omega$ is the impedance of free space, c is the speed of light and is equal to 299,792,458 m/s, f and r stand for the carrier frequency and the transmission distance, respectively.

To derive the transfer function of the molecular absorption loss, we can use the Beer-Lambert law. This law relates to the attenuation of light to the properties of the material of the space that the light is travelling through. Reference [47] provides a data base called HITRAN (HIgh resolution TRANsmission molecular absorption) database. This database helps to compute attenuation of travelling waves. The authors in [48] have used the HITRAN database, the Beer-Lambert law, and radiative transfer theory [49] to derive the transmittance of the medium as a function of the carrier frequency and the medium β given as [48]:

$$\beta(f,r) = \frac{P_0}{P_i} = e^{-k(f).r}, \tag{2.4}$$

where P_i and P_0 stand for the incident and radiated powers, respectively. f is the carrier frequency and r is the total path length. k is the medium absorption coefficient

that is highly dependent on the composition of the medium and is defined as [48]:

$$k(f) = \sum_{i,g} k^{(i,g)}(f), \tag{2.5}$$

where f is the frequency of the wave and $k^{(i,g)}$ is the individual absorption coefficient for the isotopologue i of gas g. Isotopologue is a molecule that only is different from another in its isotopic composition. In the THz band, different types of gas have different resonating isotopologues. The detail explanations about $k^{(i,g)}$ is given in [48]. Finally, the transfer function of the absorption loss is given by [4]:

$$H_{Abs}(f, r) = e^{-\frac{1}{2}k(f)r}. \tag{2.6}$$

Finally, the overall transfer function for the LoS rays, H_{LoS} is given by:

$$H_{LoS}(f, r) = \mathbb{I}_{LoS} H_{Spr}(f, r).H_{Abs}(f, r)F_t^{LoS}F_r^{LoS}.e^{-j2\pi f\tau_{LoS}}, \tag{2.7}$$

where F_t^{LoS}, F_r^{LoS} is the antenna radiation pattern factor between Tx and Rx, f is the carrier frequency, r is the transmission distance between Tx and Rx, and τ_{LoS} is the propagation delay of the LoS ray.

2.2.2 Specular Reflection

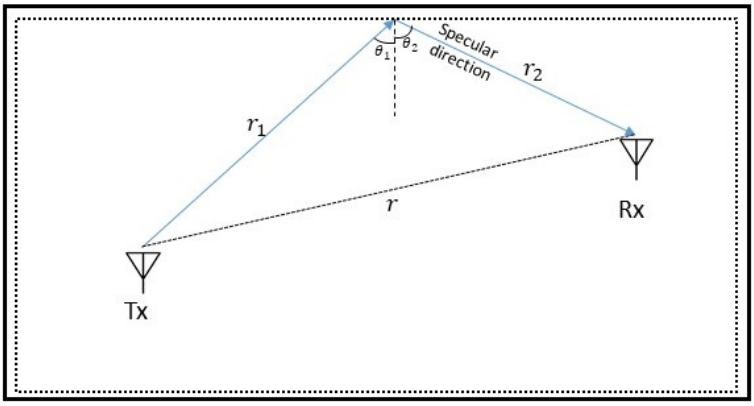

Figure 2-3: Specular reflection.

Fig. 2-3 shows an example of a specular reflection. In specular reflection, the

incident angle, θ_1, is equal to the reflection angle, θ_2, i.e., $\theta_1 = \theta_2 = \theta_i$. The transfer function of the reflected ray propagation, H_{Ref}, is given by [6]:

$$H_{Ref}(f) = (\sqrt{2Z_0}\frac{c}{4\pi f.(r_1+r_2)})F_t^{Ref}F_r^{Ref}e^{-j2\pi f\tau_{Ref}-\frac{1}{2}k(f)(r_1+r_2)}.R(f), \tag{2.8}$$

where F_t^{Ref}, F_r^{Ref} is the antenna radiation pattern factor between Tx and Rx, the time-of-arrival (ToA) of the reflected ray is given by $\tau_{Ref} = (r_1 + r_2)/c$. $Z_0 = 120\pi\ \Omega$ is the intrinsic impedance of free space.

$R(f)$ is the reflection loss for a rough surface that can be obtained using the Kirchhoff theory as a multiplication of the smooth surface reflection coefficient obtained from the Fresnel equations, γ_{TE}, with the Rayleigh roughness factor, ρ:

$$R(f) = \gamma_{TE}(f).\rho(f). \tag{2.9}$$

The Fresnel reflection coefficient for transverse electric (TE) polarized waves onto a smooth surface is given by [50]:

$$\begin{aligned}\gamma_{TE} &= \frac{cos(\theta_1) - \sqrt{n^2 - sin^2(\theta_1)}}{cos(\theta_1) + \sqrt{n^2 - sin^2(\theta_1)}} \\ &= \frac{cos(\theta_1) - n\sqrt{1 - (\frac{1}{n}sin(\theta_1))^2}}{cos(\theta_1) + n\sqrt{1 - (\frac{1}{n}sin(\theta_1))^2}} \\ &\approx -(1 + \frac{-2cos(\theta_1)}{\sqrt{n^2-1}}) \\ &\approx -exp(\frac{-2cos(\theta_1)}{\sqrt{n^2-1}}),\end{aligned} \tag{2.10}$$

where θ_1 is the angle of the incident wave as shown in Fig. 2-3 and can be calculated based on the trigonometry rules and the locations of the transmitter, the reflection point, and the receiver. n is the complex refractive index of the surface, which is a frequency and material dependent parameter [51]. The Rayleigh factor, ρ, is given by [51]:

$$\rho(f) = exp(-\frac{8\pi^2 f^2 \sigma_h^2 cos^2(\theta_1)}{c^2}), \tag{2.11}$$

where the height of the rough surface is modeled as a Gaussian distribution with the standard deviation of σ_h.

2.2.3 Scattered Rays

The wavelength of the carrier in the THz band is very short and it is smaller than 1 mm for frequencies above 0.3 THz. Therefore, a surface that might be considered a smooth surface in mm-Wave or lower frequency bands, will act as a rough surface in the THz band. Modeling the rough surface is very important in the THz band as most surfaces appear as rough surfaces in this band. A rough surface will reflect the incident wave in many different random directions, hence, scattering the rays. Fig. 2-2 (c) shows the scattered rays from a rough surface. To model the scattering components, the illuminated area around the reflection point is divided into small rectangular tiles as shown in Fig. 2-4. The geometrical parameters corresponding to each tile is shown on Fig. 2-5 depicts the i^{th} tile of the rough surface. The parameters that first need to be calculated for each tile are the transmission distance from the transmitter to the i^{th} tile, $s_t^{(i)}$, the incident angle, $\theta_1^{(i)}$, the elevation angle, $\theta_2^{(i)}$, the azimuth angle, $\theta_3^{(i)}$, the distance from the tile to the receiver, $s_r^{(i)}$, the angles of departure (AoD) at the transmitter antenna, $\theta_{TX}^{(i)}$ and $\varphi_{TX}^{(i)}$, and the angles of arrival (AoA) at the receiver, $\theta_{RX}^{(i)}$, $\varphi_{RX}^{(i)}$. The total number of tiles for a rough surface is N.

The scattering on a rough surface with a Gaussian-like height distribution without sharp irregularities is considered.

The transfer function of the scattered ray propagation for the i^{th} tile, $H_{Sca}^{(i)}$, is given by:

$$H_{Sca}^{(i)}(f) = \frac{\sqrt{2Z_0}}{2\pi} F_t^i F_r^i (\frac{l_x l_y}{s_t^{(i)} s_r^{(i)}}) e^{-j2\pi f \tau_{Sca}^{(i)} - \frac{1}{2}k(f)(s_t^{(i)} + s_r^{(i)})} . S^{(i)}(f), \tag{2.12}$$

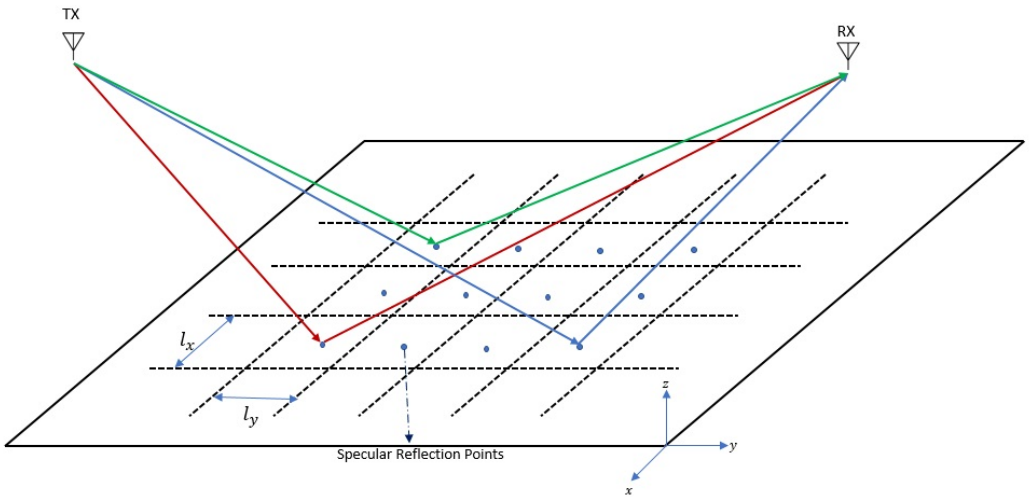

Figure 2-4: The illuminated rough surface divided into small tiles.

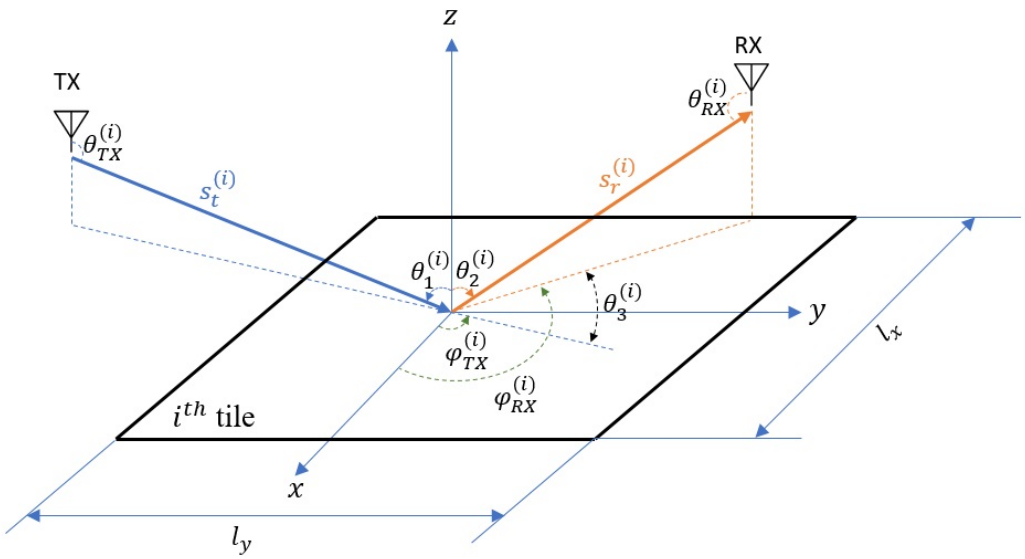

Figure 2-5: The i^{th} tile of the rough surface.

where F_t^i and F_r^i is the antenna radiation pattern factor between Tx and Rx, l_x and l_y are the dimensions of each tile, $s_t^{(i)}$ and $s_r^{(i)}$ are the distance from the i^{th} tile to the transmitter and receiver antenna, respectively. $\tau_{Sca}^{(i)} = (s_t^{(i)} + s_r^{(i)})/c$ is the time of arrival of the scattered ray, and $S^{(i)}(f)$ is the scattering coefficient that is given in [6] as:

$$S^{(i)}(f) = \left|R_{Fres}^{(i)}\right| \sqrt{\langle \rho\rho^* \rangle_{\infty}^{(i)}} \left| cos(\theta_1^{(i)}) \right| e^{j\Psi_i}, \tag{2.13}$$

where Ψ_i is a random phase variable with uniform distribution over $[0, 2\pi]$ for the i^{th} tile. $R_{Fres}^{(i)}$ is the Fresnel field reflection coefficient of a smooth surface for the i^{th} tile that consists of vertical and horizontal polarization terms given by [50] as shown in Eq. (2.14)

$$\left|R_{Fres}^{(i)}\right|^2 = \left|R_{Fres,v}^{(i)}\right|^2 \kappa_i^2 + (1-\kappa_i^2) \left|R_{Fres,h}^{(i)}\right|^2 \tag{2.14a}$$

$$R_{Fres,v}^{(i)} = \frac{cos\theta_1^{(i)} - \sqrt{n^2 - sin\theta_1^{(i)}}}{cos\theta_1^{(i)} + \sqrt{n^2 - sin\theta_1^{(i)}}} \tag{2.14b}$$

$$R_{Fres,h}^{(i)} = \frac{-ncos\theta_1^{(i)} + \sqrt{1 - n^2 sin\theta_1^{(i)}}}{ncos\theta_1^{(i)} + \sqrt{1 - n^2 sin\theta_1^{(i)}}} \tag{2.14c}$$

where $\kappa = E_v^{in}/E^{in}$ is the ratio of the vertical component to the total electric field. $\langle \rho\rho^* \rangle_{\infty}^{(i)}$ is the average power reflection coefficient of a perfect electric conductor (PEC) tile with a Gaussian-distributed rough surface and is given in [50] based on Beckmann-Kirchhoff theory:

$$\langle \rho\rho^* \rangle_{\infty}^{(i)} = e^{-g_i} \left((\rho_0^{(i)})^2 + \frac{\pi l_{corr}^2 F_i^2}{l_x l_y} \sum_{m=1}^{\infty} \frac{g_i^m}{m!m} e^{-\frac{v_i^2 l_{corr}^2}{4m}} \right), \tag{2.15}$$

where l_{corr} is the correlation length of the rough surface and larger than the wavelength of the carrier frequency. Other parameters are also given in [50]

$$g_i = \frac{4\pi^2 \sigma_h^2}{\lambda^2} (cos\theta_1^{(i)} + cos\theta_2^{(i)})^2 \tag{2.16a}$$

$$\rho_0^{(i)} = sinc(v_x^{(i)} l_x) \times sinc(v_y^{(i)} l_y) \tag{2.16b}$$

$$F_i = \frac{1 + cos\theta_1^{(i)} cos\theta_2^{(i)} - sin\theta_1^{(i)} sin\theta_2^{(i)} cos\theta_3^{(i)}}{cos\theta_1^{(i)}(cos\theta_1^{(i)} + cos\theta_2^{(i)})} \tag{2.16c}$$

$$v_i = \sqrt{(v_x^{(i)})^2 + (v_{y,i}^{(i)})^2}, \tag{2.16d}$$

where

$$v_x^{(i)} = \frac{2\pi}{\lambda}(sin\theta_1^{(i)} - sin\theta_2^{(i)} cos\theta_3^{(i)}) \tag{2.17a}$$

$$v_y^{(i)} = -\frac{2\pi}{\lambda} sin\theta_2^{(i)} sin\theta_3^{(i)} \tag{2.17b}$$

where λ is the wavelength of the carrier frequency. The standard deviation of the surface height, σ_h in Eq. (2.16a), determines the scattering behaviour of the surface. The correlation length, l_{corr} in (2.15), shows the roughness of the surface. In other words, larger l_{corr} means that the surface is smoother and smaller l_{corr} means that the surface is rougher as there is sharper variations in the surface height function.

So far, the transfer function of the channel for N_l tiles and N_{Obj} objects can be written as

$$\begin{aligned}
H(f) &= \mathbb{I}_{LoS} H_{LoS}(f) + \sum_{k=1}^{N_{Obj}} H_{Ref}^{(k)}(f)\delta(\theta_1 - \theta_2)\delta(\theta_3) + \sum_{k=1}^{N_{Obj}} \sum_{i=1}^{N_l} H_{Sca}^{(i,k)}(f) \\
&= \mathbb{I}_{LoS} \sqrt{2Z_0} \frac{c}{4\pi f r} . e^{-\frac{1}{2}k(f)r} F_t^{LoS} F_r^{LoS} . e^{-j2\pi f \tau_{LoS}} \\
&+ \sum_{k=1}^{N_{Obj}} \sqrt{2Z_0} \frac{c}{4\pi f . (r_1^{(k)} + r_2^{(k)})} F_t^{Ref} F_r^{Ref} e^{-j2\pi f \tau_{Ref}^{(k)} - \frac{1}{2}k(f)(r_1^{(k)} + r_2^{(k)})} . R^{(k)}(f) . \delta(\theta_1 - \theta_2)\delta(\theta_3) \\
&+ \sum_{k=1}^{N_{Obj}} \sum_{i=1}^{N_l} \frac{\sqrt{2Z_0}}{2\pi} \left(\frac{l_x l_y}{s_t^{(i,k)} s_r^{(i,k)}}\right) F_t^i F_r^i e^{-j2\pi f \tau_{Sca}^{(i,k)} - \frac{1}{2}k(f)(s_t^{(i,k)} + s_r^{(i,k)})} \left| R_{Fres}^{(i,k)} \right| \sqrt{\langle \rho \rho^* \rangle_\infty^{(i,k)}} \left| cos(\theta_1^{(i,k)}) \right| e^{j\Psi_{i,k}}
\end{aligned} \tag{2.18}$$

Discussion on Tile Size

The formulation of the rough surface presented in [50], known as Beckmann-Kirchhoff, is only for one rough surface that is illuminated by a plane wave. In a real world indoor environment, this assumption is not true since there are multiple objects such as the walls, tables in a room, and ceiling that can reflect the NLoS rays. To overcome this challenge, each surface is divided into equal tiles. Each tile has a dimension of $l_x \times l_y$. If these tiles are small enough compared to the distance between the transmitter antenna and the illuminated object, the electric field can be considered as a plane wave [52]. The requirement for this condition is that each tile should be in the far-field region of the transmitter and receiver antennas. To meet this condition we should have the following [6]

$$max(l_x, l_y) \leq \sqrt{\frac{\lambda}{2}r}. \tag{2.19}$$

The size of each tile is important since it affects the time resolution of the multi-path components. A rule of thumb to select the size of the tile is that it has to be larger than the correlation length, l_{corr}, as given in [50], i.e., $min(l_x, l_y) \gg l_{corr}$. This condition will also make sure that the tile size is much greater than the wavelength as $l_{corr} \gg \lambda$. This means that the edge effect will not affect the validity of Beckmann-Kirchhoff formulations [50].

2.2.4 Diffracted Rays

The diffraction model can be approximated using the Fresnel Knife Edge Diffraction (KED) theory. The diffraction channel transfer function for one object is given by [4]. However, this formula needs to be modified to make it consistent with our formulation. Therefore, the Z_0, antenna radiation pattern factors between Tx and Rx, F_t^{Diff} and F_r^{Diff} has to be added to the original formula. Eq. (2.20) is the diffraction channel transfer function, $H_{Diff}(f)$, for one object

$$H_{Diff}(f) = \sqrt{2Z_0}\frac{c}{4\pi f(d_1+d_2)}F_t^{Diff}F_r^{Diff}e^{-j2\pi f\tau_{Dif}-\frac{1}{2}k(f)(d_1+d_2)}.L(f), \tag{2.20}$$

where d_1 and d_2 are the distance between the transmitter antenna and the diffracting point and the distance between the diffracting point and the receiver antenna, respectively. Time-of-arrival of the diffracted ray is $\tau_{Dif} = \tau_{LoS} + \Delta d/c$. If $\nu(f) = \sqrt{\frac{2f\Delta d}{c}}$ where Δd can be calculated based on the geometry of the environment in Fig. 2-2 (d), as $\Delta d = \frac{h_d^2(d_1+d_2)}{2d_1d_2}$. This means that the diffracted path will be slightly longer than the LoS path length. This extra distance is approximated by Δd. The diffraction coefficient, $L(f)$, can be derived by an approximation to the Fresnel integral as shown in [4], as

$$L(f) = \begin{cases} \mu_1(f).(0.5e^{-0.95\nu(f)}) & 0 < \nu(f) \leq 1, \\ \mu_2(f).\left(0.4 - \sqrt{0.12 - (0.38 - 0.1\nu(f))^2}\right) & 1 < \nu(f) \leq 2.4, \\ \mu_3(f).(0.225/\nu(f)) & \nu(f) > 2.4, \end{cases} \tag{2.21}$$

where the parameters $\mu_1(f), \mu_2(f)$, and $\mu_3(f)$ that are frequency-dependent, are chosen to best fit the data presented in [53].

The overall channel model including the diffracted rays can be written as

$$\begin{aligned} H(f) = \mathbb{I}_{LoS}H_{LoS}(f) + \sum_{k=1}^{N_{Obj}} H_{Ref}^{(k)}(f)\delta(\theta_1-\theta_2)\delta(\theta_3) + \sum_{k=1}^{N_{Obj}}\sum_{i=1}^{N_l} H_{Sca}^{(i,k)}(f) \\ + \mathbb{I}_{Dif}\sum_{l=1}^{N_{Dif}} H_{Diff}^{(l)}(f) \end{aligned} \tag{2.22}$$

where $\mathbb{I}_{Dif}$ is an indicator of the existence of diffracting objects in the environment. If the indicator is $\mathbb{I}_{Dif} = 0$, it means that there is no diffracting object. On the other hand, if it is equal to 1, it means that at least one diffracting point is present in the environment. N_{Dif} is the number of diffracting points, N_l is the number of tiles on

one surface, and N_{Obj} is the number of reflecting objects in the environment.

Finally, the channel transfer function in time domain for the m_{th} frequency band is given by

$$
\begin{aligned}
h_m(\tau) &= \mathbb{I}_{LoS}\sqrt{2Z_0}\frac{c}{4\pi f_m r}.e^{-\frac{1}{2}k(f_m)r}F_t^{LoS}F_r^{LoS}.\delta(\tau-\tau_{LoS}) \\
&+ \sum_{k=1}^{N_{Obj}}\sqrt{2Z_0}\frac{c}{4\pi f_m.(r_1^{(k)}+r_2^{(k)})}F_t^{Ref}F_r^{Ref}e^{-\frac{1}{2}k(f_m)(r_1^{(k)}+r_2^{(k)})}.R^{(k)}(f_m).\delta(\theta_1-\theta_2)\delta(\theta_3)\delta(\tau-\tau_{Ref}^{(k)}) \\
&+ \sum_{k=1}^{N_{Obj}}\sum_{i=1}^{N_l}\frac{\sqrt{2Z_0}}{2\pi}(\frac{l_x l_y}{s_t^{(i,k)}s_r^{(i,k)}})F_t^iF_r^ie^{-\frac{1}{2}k(f_m)(s_t^{(i,k)}+s_r^{(i,k)})}\left|R_{Fres}^{(i,k)}\right|\sqrt{\langle\rho\rho^*\rangle_\infty^{(i,k)}}\left|cos(\theta_1^{(i,k)})\right|e^{j\Psi_{i,k}}\delta(\tau-\tau_{Sca}^{(i)}) \\
&+ \mathbb{I}_{Dif}\sum_{l=1}^{N_{Dif}}\sqrt{2Z_0}\frac{c}{4\pi f_m(d_1^{(l)}+d_2^{(l)})}F_t^{Diff}F_r^{Diff}e^{-\frac{1}{2}k(f_m)(d_1^{(l)}+d(l)_2)}.L^{(l)}(f_m)\delta(\tau-\tau_{Dif}^{(l)})
\end{aligned}
\tag{2.23}
$$

2.3 Conclusion

In this chapter, a channel model that was originally based on Beckmann-Kirchhoff theory [50] was studied. The ray-tracing technique was adopted to develop this channel model [46]. However, the model presented in [46] lacks an accurate scattering model since the power of the channel changes while varying the tile size which is not physically correct. Therefore, a new scattering model that was introduced in [6], is incorporated in the original multi-ray channel model. On the other hand, the channel model introduced in [6], is shown to be accurate enough for LoS, specular reflection, and scattering rays. Therefore, the effect of diffraction was not studied in [6]. Hence, in this chapter, we unified both models to have the most accurate channel model so far. However, for simulation purposes, we do not consider any diffracting objects. Therefore, the diffraction indicator, $\mathbb{I}_{Dif}$, will be set to zero in Chapter 4.

Chapter 3

OFDM and DFT-s-OFDM in the THz Band

Single-carrier and multi-carrier waveforms each have their own advantages and disadvantages over a wireless communication channel. In the THz band channels, the number of multi-path components will be limited due to the high path loss that is a direct result of using high frequencies as carriers. Therefore, the communication channel will have some frequency-flat features. In this situation, low-complexity wide-band single-carrier systems will be favourable. On the other hand, the molecular absorption loss that is a frequency-dependant variable, and the geometry of an indoor environment which will result in the existence of multi-path components, can make the channel to be frequency-selective. If the channel coherence bandwidth, B_c, is smaller than transmitted signal bandwidth, B_s, the channel will introduce frequency-selective fading to the transmitted signal. In this situation, a multi-carrier waveform such as orthogonal frequency-division multiplexing (OFDM) will be more favourable as multi-carrier waveforms handle the frequency-selectivity effects better than single-carrier systems. Various configurations of single/multi-carrier designs will have different THz spectrum utilization. However, the THz band has ultra-large bandwidth resources and therefore, spectral efficiency is not the main concern. The main concerns in designing a communication system in the THz band include, but are not limited to, baseband complexity, power efficiency, and hardware impairment constraints like phase noise.

In this chapter, we provide a comprehensive study of two main single-carrier and multi-carrier waveforms. The single-carrier waveform that will be studied in this chapter is called discrete Fourier-transform spread OFDM (DFT-s-OFDM).

In the following sections, we aim to describe the modulation and demodulation steps of each candidate single-carrier and multi-carrier waveform.

3.1 Effect of Frequency-Selective Fading

The received signal in time domain at the receiver can be described as follows

$$r(t) = u(t) * h(t) + n(t), \tag{3.1}$$

where $u(t)$ is the baseband transmitted signal, $h(t)$ represents the channel impulse response, and $n(t)$ is the additive white Gaussian noise (AWGN) in time domain. For a digital wireless transmission system, the data symbol s_i is transmitted over each symbol period after pulse shaping. The transmitted baseband signal is given by

$$u(t) = \sum_{i=-\infty}^{+\infty} s_i g(t - iT_s), \tag{3.2}$$

where $g(t)$ is the pulse shaping filter and T_s is the symbol period.

Assuming that the receiver applies matched filter detection with filter response $g^*(T_s - t)$ and choosing the proper $g(t)$ so that the overall response of pulse shaping and matched filter, $g(t) * g^*(T_s - t)$, satisfies the Nyquist criterion, it can be shown that the received baseband signal over the i^{th} symbol period is given by [54]

$$r_i = \sum_{l=0}^{L-1} h_l s_{i-l} + n_i, \tag{3.3}$$

where L is the number of channel taps. As it can be seen, the received symbol is the linear convolution of the transmitted symbols with the channel taps plus AWGN samples n_i. Moreover, the received symbols can be re-written in a way to distinguish the desired transmitted symbol, s_i, from the rest of transmitted symbols as follows

$$r_i = h_0 s_i + \sum_{l=1}^{L-1} h_l s_{i-l} + n_i, \tag{3.4}$$

The term $\Sigma_{l=1}^{L-1} h_l s_{i-l}$ is the interference that comes from other symbols due to multipath fading and is referred to as "intersymbol interference" (ISI). To detect the desired transmitted symbol, s_i, it is crucial to effectively handle the ISI. Failure to do so can significantly degrade the performance of the system. Equalization is the process of removing the effect of frequency-selective fading channel. As a result, the ISI effect will be mitigated after the received signal is properly equalized.

By taking the Fourier transform, the baseband received signal in frequency domain, $R(f)$, can be written as follows

$$R(f) = \mathcal{F}\{u(t) * h(t) + n(t)\} = U(f) \times H(f) + N(f), \tag{3.5}$$

where $\mathcal{F}\{.\}$ denotes the Fourier transform operation, $U(f)$ is the spectrum of $u(t)$, $H(f)$ is the channel frequency response, and $N(f)$ represents the noise spectrum.

The frequency response of a simple equalizer is designed to be the inverse of the channel frequency response, i.e.,

$$H_{eq}(f) = \frac{c}{H(f)}, \tag{3.6}$$

where c is a normalizing constant that depends on the output power constraint of the equalizer.

The baseband received signal after equalization in frequency domain is given by

$$Y(f) = H_{eq}(f) \times R(f) = c \times U(f) + H_{eq}(f) \times N(f). \tag{3.7}$$

As a result, the ISI effect will be completely eliminated.

3.2 Multi-carrier Transmission

Multi-carrier transmission is a widely used digital wireless transmission technology over frequency-selective fading channels. The idea is to divide the wide-band selective channel into many parallel narrow-band sub-channels. Then, over each of those sub-channels, a low rate sub-stream will be transmitted. By increasing the number of sub-channels, i.e., reducing the bandwidth of each sub-channel, we can make sure that each sub-stream experiences a frequency flat fading sub-channel. In this case, the bandwidth of each sub-channel will be less than the channel coherence bandwidth. Conventionally, to implement the multi-carrier transmission, we needed to use multiple narrow-band modulators and demodulators which would highly increase the complexity of the system. In the 1990s, when the discrete implementation of multi-carrier transmission was developed, it became more efficient to use the discrete version of OFDM as a multi-carrier transmission that preserves all the good features of multi-carrier transmission by only using a single modulator and demodulator pair. As a result, OFDM becomes the main waveform widely used in wireless communication systems and can be seen as a benchmark for the newly designed waveforms.

3.2.1 OFDM

As it can be seen, the subcarriers in a multi-carrier transmission system are non-overlapping. Therefore, at the receiver they can be distinguished. The main disadvantage of this approach is that the spectral efficiency of the system will be low. Especially, in environments that the bandwidth is limited, a conventional multi-carrier system can face a lot of challenges. To address this issue, it is suggested to use subcarriers that are orthogonal to each other over a sub-channel symbol period. Hence, the subcarriers can still be distinguished at the receiver and also the transmitted signal will use less bandwidth in frequency domain.

Thanks to the advancements in the implementation of digital signal processing (DSP) techniques, such as the discrete Fourier transform (DFT) and inverse DFT (IDFT), we can calculate both DFT and IDFT very efficiently using fast Fourier

transform (FFT) and inverse FFT (IFFT) algorithms.

Assuming the transmission of N modulated data symbols, $\{s_0, s_1, ..., s_{N-1}\}$, over a frequency selective-fading channel with channel impulse response, $h_n, n = 0, 1, ..., L-1$ and the length of L, the effect of ISI will be removed by using a multi-carrier transmission. Therefore, the input/output relation is given by [54]

$$y_i = H(i) \times s_i + n_i, i = 0, 1, ..., N-1, \tag{3.8}$$

where y_i is the decision statistics corresponding to data symbol s_i, n_i is the AWGN noise, and $H(i)$ is the channel frequency response at frequency $f_i = f_c + i/T_N$, where T_N is the sub-channel symbol period. By taking N-point DFT of the channel impulse response, h_n, we can get $H(i)$ given by

$$H(i) = DFT_N\{h_n\} = \sum_{n=0}^{L-1} h_n e^{-j2\pi ni/N}, i = 0, 1, ..., N-1. \tag{3.9}$$

If we neglect the AWGN noise term, the received symbol in time domain can be written as

$$r_n = IDFT_N\{y_i\} = IDFT\{H(i).s_i\} = h_n \circledast x_n, \tag{3.10}$$

where x_n is the N-point IDFT of s_i, given by

$$x_n = IDFT_N\{s_i\} = \frac{1}{N} \sum_{i=0}^{N-1} s_i e^{j2\pi ni/N}, n = 0, 1, ..., N-1, \tag{3.11}$$

where $h_n \circledast x_n$ represents the circular convolution of h_n and x_n given by

$$r_n = \sum_{k=0}^{L-1} h_k x_{(n-k)_N}, \tag{3.12}$$

and $(n-k)_N$ denotes $n-k$ modulo N.

As a summary we can say that the desired input/output relation for multi-carrier transmission can be achieved if we follow the following steps: (a) transmit the IDFT of data symbols, x_n, (b) get the circular convolution of x_n and h_n at the receiver, r_n,

and (c) perform DFT on r_n [54].

To get the circular convolution, we need to copy a portion of the tail of the signal in the beginning of the signal. This copied part is called *cyclic prefix* (CP). CP makes not only the convolution of two finite sequences to be circular but also protects the signal against *inter-block interference* (IBI) which will happen when two consecutive blocks are sent through a multi-path fading channel. Fig. 3-1 shows how CP is inserted for two OFDM blocks. The length of CP is an important parameter that needs to be carefully chosen to get the best results. A general rule of thumb is that CP duration has to be greater than the root mean square (RMS) delay spread of the channel. In Chapter 4 more details will be given with regards to CP length and its relation to the THz channel.

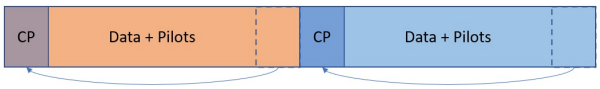

Figure 3-1: Illustration of the placement of CP for two consecutive OFDM blocks.

After inserting the CP to the signal, a pulse-shaping filter which is usually a root-raised-cosine (RRC) filter is applied. The frequency response of such a filter is given in Eq. (3.13)

$$G(f) = \begin{cases} \sqrt{T} & \left(0 \leq |f| \leq \frac{1-\beta}{2T}\right), \\ \sqrt{\frac{T}{2}\{1 + cos[\frac{\pi T}{\beta}\left(|f| - \frac{1-\beta}{2T}\right)]\}} & \left(\frac{1-\beta}{2T} \leq |f| \leq \frac{1-\beta}{2T}\right), \\ 0 & (|f| > \frac{1-\beta}{2T}), \end{cases} \tag{3.13}$$

So far, at the transmitter of an OFDM system, the information bits go through a symbol mapping block, then IDFT will be applied, the result that is a time domain signal will go through a CP block that copies a portion of the tail of the signal to the beginning of the signal. Finally, the signal will go through the RF block to be prepared to be transmitted over the THz channel. The RF block includes a pulse shaping filter and a digital to analog converter (DAC). At the receiver, the received signal passes through an analog to digital (ADC) converter.

3.2.2 CP-DFT-s-OFDM

The DFT-s-OFDM, also known as Precoded Orthogonal Frequency Division Multiplexing, has gained widespread popularity as an uplink solution in 4G-LTE/5G-NR communication systems, and is a promising candidate for the Terahertz (THz) frequency band. The integration of a Discrete Fourier Transform block at the transmitter serves to reduce the Peak-to-Average Power Ratio (PAPR) while preserving the benefits of single-carrier modulation, with only a minor increase in computational complexity. The primary advantage of this approach is the reduction of power consumption and cost associated with power amplifiers at the user terminal. When data symbol blocks are assigned to multiple users, the DFT-s-OFDM reduces to Single Carrier Frequency Division Multiple Access (SC-FDMA) in these scenarios.

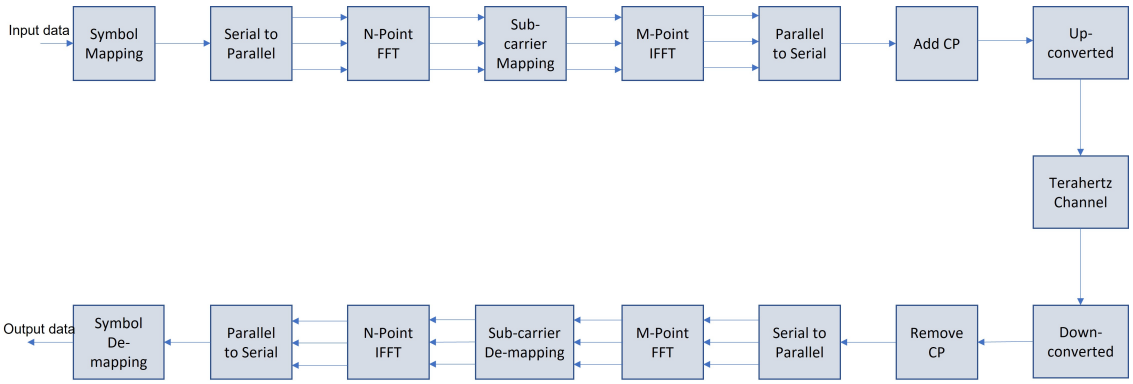

Figure 3-2: Block diagram of a DFT-s-OFDM system.

As illustrated in Fig. 3-2, the data symbols are first passed through a DFT-precoding component. The output of this component consists of complex symbols that modulate the OFDM subcarriers. In the case where $N = M$, the system reduces to a simple single carrier transmission. However, we are particularly interested in the scenario where $N < M$, as this allows us to take advantage of the benefits of multi-carrier transmission. The $M - N$ unused subcarriers, also known as inactive subcarriers, are set to zero. The frequency domain data then passes through an M-point IFFT block to convert the symbols to the time domain. Finally, after adding a cyclic prefix to the serial data stream, the signal is up-converted and sent through the communication channel. At the receiver side, the opposite process is done to

get the output data. However, the block diagram shown in Fig. 3-2 is a simple yet comprehensive version what an actual DFT-s-OFDM looks like. The diagram will have more components in Chapter 4 where the simulation results are presented. Particularly, channel coding will be used.

3.2.3 Subcarrier Mapping

There are two approaches to subcarrier mapping in DFT-s-OFDM, namely localized subcarrier mapping and interleaved subcarrier mapping which are used in localized frequency division multiple access (LFDMA) and interleaved frequency division multiple access (IFDMA) systems, respectively.

Localized subcarrier mapping assigns the data symbols to consecutive subcarriers in the frequency domain, resulting in a contiguous block of subcarriers being assigned to each user. This approach results in low PAPR and has low computational complexity.

Interleaved subcarrier mapping, on the other hand, assigns data symbols to subcarriers that are separated by a certain distance in the frequency domain, resulting in data symbols being spread out among multiple subcarriers. This approach provides improved frequency diversity and is less vulnerable to channel fading. However, it results in a higher PAPR and has higher computational complexity compared to localized subcarrier mapping.

Both techniques have their advantages and disadvantages, and the choice between the two approaches depends on the specific requirements of the communication system and the trade-off between PAPR, computational complexity, and frequency diversity.

The ratio $Q = \frac{M}{N}$ is called *spreading factor*. Fig. 3-3 shows an example of how subcarrier mapping is done for $N = 4$ and $M = 12$. In this example the spreading factor, $Q = 3$.

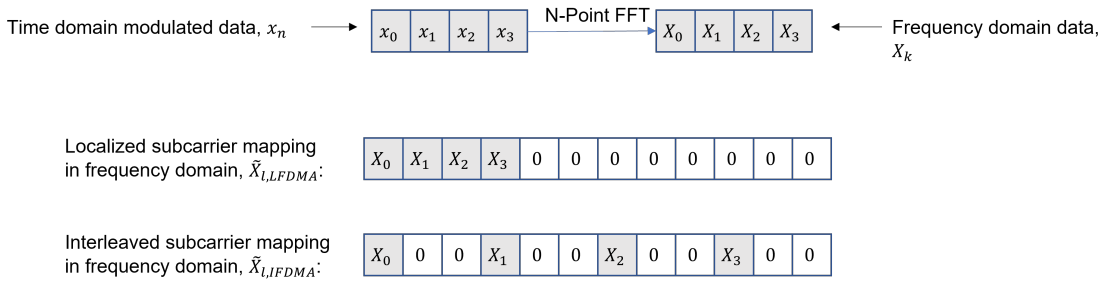

Figure 3-3: Localized vs. interleaved subcarrier mapping.

3.3 Peak-to-Average Power Ratio (PAPR)

PAPR is a measure of the peak power of an OFDM signal compared to its average power. Mathematically, it is defined as the ratio of the maximum instantaneous power of an OFDM signal to the average power of the signal, and is given by the formula:

$$PAPR = \frac{max(|x(n)|^2)}{(\frac{\sum(|x(n)|^2)}{N})}, \tag{3.14}$$

where $x(n)$ is the complex envelope of the OFDM signal, and N is the number of subcarriers in the OFDM signal.

In the terahertz band, the high PAPR values can cause nonlinear distortion in the power amplifier, which can lead to reduced system efficiency, increased error rate, and even signal degradation. Additionally, high PAPR values also require higher crest factors in the power amplifiers, which can lead to increased power consumption and cost. It is also worth mentioning that in the terahertz band, the propagation characteristics of the signal are different from lower frequency bands, so the PAPR reduction techniques that are effective in lower frequency bands may not be effective in the terahertz band. Crest factor is a measure of the PAPR of a signal, specifically the ratio of the peak power to the RMS power of the signal. It is commonly used to evaluate the dynamic range of a signal and is an indicator of the level of distortion that might be expected when amplifying the signal.

It is worth mentioning that PAPR is a statistical measure, and it is usually defined in dB, so $PAPR_{dB} = 10\log_{10}(PAPR)$. In addition to the formula above, there are several other ways to calculate PAPR. One of the most common methods is to

calculate the complementary cumulative distribution function (CCDF) of the PAPR. The CCDF is defined as the probability that the PAPR is greater than a certain threshold value.

Another way to calculate PAPR is to use the average power of the complementary signal, which is defined as the average power of the signal that exceeds a certain threshold value.

3.4 Channel Coding

In modern wireless communication systems, channel coding plays a crucial role in ensuring the reliability and efficiency of data transmission. In particular, OFDM systems, which are widely used in various communication standards, benefit greatly from the application of channel coding techniques.

The primary objective of channel coding in OFDM systems is to mitigate the detrimental effects of the channel, such as noise, interference, and fading, on the transmitted data. Channel coding is utilized to achieve error correction and detection, which enables the reliable recovery of the original data at the receiver. Furthermore, by adding redundant information to the data, channel coding allows for the efficient use of the available bandwidth, thus improving the overall efficiency of the communication system. In addition to its error-correction capability, channel coding also enhances the robustness of OFDM systems, allowing them to operate in adverse channel conditions.

In OFDM systems, channel coding is typically applied at the bit or symbol level, and it is often combined with other techniques such as interleaving and modulation to further improve the performance of the system. Commonly used channel coding techniques in OFDM systems include convolutional coding, low-density parity-check (LDPC) coding, and turbo coding.

Convolutional coding, as a well-established channel coding technique, has been widely used for many decades. It works by encoding the data stream into a coded sequence, which is then transmitted over the channel. The Viterbi decoder is used to

decode the received data and recover the original information. Convolutional coding provides good error correction performance, especially in noisy channels.

LDPC coding, a relatively new channel coding technique, has gained popularity in recent years due to its excellent error correction performance and low complexity. LDPC codes are linear error-correction codes that use a sparse parity-check matrix to define the code structure. The parity-check matrix defines a set of linear equations that must be satisfied by the coded data. The receiver uses an iterative decoder to decode the received data and recover the original information.

In OFDM systems, both convolutional coding and LDPC coding can be used to provide error correction and enhance the robustness of the system. However, the choice between the two techniques depends on various factors, including the required error correction performance, computational complexity, and implementation cost.

LDPC coding is generally favored in OFDM systems due to its excellent error correction performance and low complexity, especially in high-speed wireless communication systems. On the other hand, convolutional coding is favored in applications that require low complexity and low implementation cost, such as low-speed wireless communication systems.

Overall, the application of channel coding techniques in OFDM systems is a crucial aspect of modern wireless communication systems, and it plays a vital role in ensuring the reliability and efficiency of data transmission.

3.4.1 Low-Density Parity-Check Codes

Low-Density Parity-Check (LDPC) codes are a type of linear block codes that feature large codeword lengths, typically in the range of thousands. The defining characteristic of LDPC codes is their parity-check matrix, $\mathbf{H}$, which is sparse, meaning that there are relatively few 1s compared to 0s in the matrix. As a result, the codes are referred to as low density, reflecting the low density of 1s in the matrix.

A regular LDPC code can be defined as a linear block code with a sparse parity-check matrix that satisfies the following properties [55]:

1. Each row of $\mathbf{H}$, contains w_r 1s, where $w_r \ll \min\{m, n\}$.

2. Each column of $\mathbf{H}$, contains w_c 1s, where $w_c \ll \min\{m, n\}$.

where $\mathbf{H}$ has a dimension of $m \times n$ and n is the length of the codeword.

As it can be seen, these conditions require the parity check matrix to be very large. Below, a parity check matrix $\mathbf{H}$ is shown as an example. This matrix has a dimension of 4×8 and has four and two 1s in each column and row, respectively. The notation used to describe this matrix is $\mathbf{H}$ of $(8, 4, 2)$.

$$\mathbf{H} = \begin{bmatrix} 0 & 1 & 0 & 1 & 1 & 0 & 0 & 1 \\ 1 & 1 & 1 & 0 & 0 & 1 & 0 & 0 \\ 0 & 0 & 1 & 0 & 0 & 1 & 1 & 1 \\ 1 & 0 & 0 & 1 & 1 & 0 & 1 & 0 \end{bmatrix} \tag{3.15}$$

In the next step, the coding rate, R, needs to be defined. By definition, the coding rate is the ratio between the number of message bits, k, and number of transmitted bits, n, as shown in Eq. (3.16). It is obvious that $0 < R \leq 1$ and $R = 1$ means that no coding is being done.

$$R = \frac{k}{n}. \tag{3.16}$$

In Eq. (3.15), each row of $\mathbf{H}$ represents a check node and each column indicates a variable node. In this context, variable nodes represent the components of the code word, while check nodes indicate a collection of parity checks. The $\mathbf{H}$ matrix displays connections between check nodes and variable nodes as represented by the presence of a 1 in the matrix.

The matrix $\mathbf{H}$ can be represented using the *tanner graph* representation as shown in Fig. 3-4. A connection between a check node, u_i, and a variable node, v_j, is made when the corresponding entry in the parity check matrix, $h_{i,j}$ is 1. For the matrix $\mathbf{H}$ in Eq. (3.15), there are four check nodes and eight variable nodes.

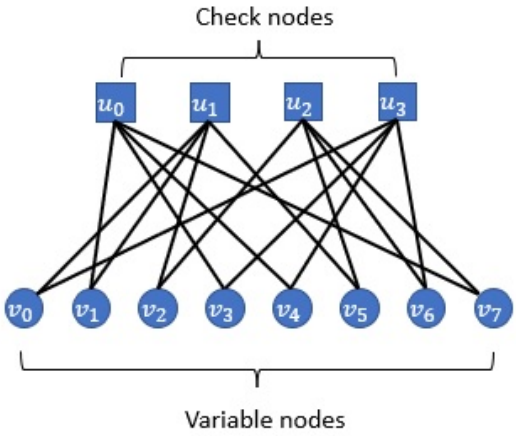

Figure 3-4: Tanner graph representation of **H** in Eq. (3.15).

LDPC Encoding

The most common way of encoding encoding a data stream using LDPC is called *linear block code encoding*. A codeword of a linear block code, $C_{1\times n}$, is comprised of both message bits and parity bits, which can be represented as follows:

$$C_{1\times n} = [m_{1\times k}|P_{1\times n-k}]. \tag{3.17}$$

where $m_{1\times k}$ is the message bits and $P_{1\times n-k}$ is the parity vector. Like other types of linear block codes, the following equation will be used to find the parity vector $P_{1\times n-k}$:

$$C.\mathbf{H}^T = \bar{0}, \tag{3.18}$$

where $\bar{0}$ is a vector of zeros with dimension of $1 \times m$. In other words, the codeword $C_{1\times n}$ satisfies all the m constraints represented by the rows of the parity check matrix **H**.

LDPC Decoding

One of the most widely used decoding methods for Low Density Parity Check (LDPC) codes is the Belief Propagation (BP) algorithm. It is an iterative method that makes use of the sparse structure of LDPC codes to correct errors in the transmitted data.

In the BP algorithm, the decoding process is performed by exchanging messages between the variable nodes and the check nodes of the LDPC code. At each iteration, the messages are updated based on the information received from the neighboring nodes. The messages are updated based on the following two rules:

1. Check node to variable node message update: Let u be the index of a check node and v be the index of a variable node connected to the check node. Then, the message $m_{u\to v}$ is updated based on the messages received from all other variable nodes connected to the check node u. The updated message $m_{u\to v}$ can be expressed as follows:

$$m_{u\to v}(x_v) = \prod_{j\in N_u \text{ and } j\neq v} m_{j\to u}(x_v) \tag{3.19}$$

where N_u is the set of variable nodes connected to the check node u, and $m_{j\to u}(x_v)$ is the message sent from the variable node j to the check node u.

2. Variable node to check node message update: Let v be the index of a variable node and u be the index of a check node connected to the variable node. Then, the message $m_{v\to u}$ is updated based on the channel information and the messages received from all check nodes connected to the variable node v. The updated message $m_{v\to u}$ can be expressed as follows:

$$m_{v\to u}(x_v) = \frac{1}{Z_{v,u}} \prod_{d\in N_v \text{ and } d\neq u} m_{d\to v}(x_v) \cdot p_{ch}(y_v|x_v) \tag{3.20}$$

where N_v is the set of check nodes connected to the variable node v, $Z_{v,u}$ is a normalization constant, $m_{d\to v}(x_v)$ is the message sent from the check node d to the variable node v, and $p_{ch}(y_v|x_v)$ is the conditional probability of receiving the value y_v given that the transmitted symbol was x_v.

The decoding process continues until either a valid codeword is found or a maximum number of iterations is reached. If a valid codeword is found, then the decoding process is successful, otherwise, it is considered as a failure.

The BP algorithm is a powerful decoding method for LDPC codes due to its ability to effectively exploit the sparse structure of the code. However, its performance can

be affected by the presence of loops in the Tanner graph representation of the code, as well as by the presence of channel noise.

LDPC Codes in 5G Standard

In communication standards, LDPC codes are frequently implemented using a specific type of construction called *protograph* construction. This is because protograph construction provides several benefits for LDPC coding, such as low implementation complexity, low decoding latency, and the ability to customize the code structure to meet specific requirements, such as error correction performance and code rate. The protograph construction method works by defining a small base matrix called base graph, BG, that is then used as a building block to generate a larger, full-sized matrix for the actual code. This base matrix is referred to as a protograph and it encapsulates the structural information of the code. The full-sized matrix is created by replicating the protograph multiple times which is defined in the standard as the *expansion factor*, making it possible to achieve a desired code rate and performance. The base matrices have the property of being expandable, which means they can be expanded to larger matrices through the application of right shift permutation matrices. This feature allows for the creation of LDPC codes with a wide range of rates, making them suitable for various communication systems and applications.

In the 5G standards, there are two base graph constructions that are used, namely BG_1 and BG_2. The dimensions of these base matrices are defined as 46×68 for BG_1 and 42×52 for BG_2. Both base matrices have a block structure as shown below:

$$BG = \begin{bmatrix} A & E & O \\ B & C & I \end{bmatrix} \tag{3.21}$$

where for BG_1 the sub-matrix A has a dimension of (4×22), E is a (4×4) matrix, and O is a matrix made of all -1's that will be replaced with a matrix of all zeros with the dimension of (4×42) after the base graph is expanded. B and C are matrices with dimension of (42×22) and (42×4), respectively. Additionally, the identity matrix I has a dimension of (42×42). Similarly, for BG_2 the sub-matrix A has a

dimension of (4×10), E is a (4×4) matrix, and O is a matrix made of all -1's that will be replaced with a matrix of all zeros with the dimension of (4×38) after the base graph is expanded. B and C are matrices with dimension of (38×10) and (38×4), respectively. The identity matrix I has a dimension of (38×38). As per the standards, the expansion factors for these base graphs are also defined. In simulations, the program receives the index of the base graph, and based on the codeword length, it determines the correct expansion factor.

Rate Matching and Rate Recovering for LDPC Codes

In the 5G standard, there is two possible base graphs available to be used. As mentioned in the previous section, these base graphs have a fixed size and will be expanded using an extension factor, Z, to get the actual parity check matrix, $\mathbf{H}$. Each of these base graphs is only capable of achieving a specific coding rate. Assume BG_1 is to be used by the communication system. This matrix has a dimension of 46×68. As defined in the standard, the first 22 columns are corresponding to the message bits and the other 46 columns are corresponding to the parity bits. It is worth mentioning that the first 2 columns of the matrix will be punctured during the transmission. Therefore, after the expansion the number of message bits will be $22Z$ that the first $2Z$ are punctured. The total number of codeword bits will be $68Z$ and since the first $2Z$ are punctured, there will be $66Z$ codeword bits in total. Hence, the coding rate is calculated to be

$$R = \frac{\text{Number of message bits}}{\text{Number of codeword bits}} = \frac{22Z}{66Z} = \frac{1}{3}. \tag{3.22}$$

This rate is the lowest rate achievable using BG_1 regardless of the expansion factor.

Similarly, for BG_2, which is a 42×52 matrix that the first 10 columns represent the message bits and the other 42 columns represent the parity bits, the lowest rate possible is calculated to be

$$R = \frac{\text{Number of message bits}}{\text{Number of codeword bits}} = \frac{10Z}{50Z} = \frac{1}{5}. \tag{3.23}$$

The use of a different coding rate than the base rate defined in Eq. (3.22) and Eq. (3.23) may be necessary in various scenarios. For instance, the communication system may require a higher coding rate for a better spectral efficiency, or a lower coding rate to trade-off between error correction capability and data rate. Additionally, the specific channel conditions, such as the signal-to-noise ratio, may demand a specific coding rate. Moreover, the available bandwidth and the target data rate may also drive the choice of the coding rate. Hence, the selection of the coding rate is a trade-off between various factors, and the specific requirements of the communication system should dictate the desired coding rate. In these situations, it is necessary to use a technique named *Rate Matching*. This can be done by not transmitting a portion of the parity bits. As an example, let's assume we would like to have a coding rate of 2/3 while using BG_1. In this case, we will have $22Z$ columns for the message bits and $13Z$ columns for the parity bits. Therefore the coding rate is calculated as follows

$$R = \frac{\text{Number of message bits}}{\text{Number of codeword bits}} = \frac{22Z}{22Z + 13Z - 2Z} = \frac{2}{3}. \tag{3.24}$$

Note that the $2Z$ of the first two columns are punctured therefore not included in the total number of codeword bits. Similarly, other higher rates can be achieved by not transmitting a portion of the parity bits.

At the receiver side, a process called *Rate Recover* will be implemented. Assume that $R = 2/3$ and BG_1 is used . This means that only $13Z$ parity bits were sent. Therefore, in the decoder, we only use the $13Z \times 35Z$ top left part of the parity check matrix, $\mathbf{H}$. Note that in the decoder, the punctured columns will also be used. That's why the dimension of the sub-matrix to be used is $13Z \times 35Z$.

3.5 Phase Noise

A fully functional communication system requires various physical components. At the transmitter side, a digital signal processing unit is utilized to convert digital bits into modulated symbols, which are then fed to a digital-to-analog converter (DAC). The DAC output signal is then mixed with a local oscillator signal, resulting in a radio frequency (RF) signal ready for transmission. This RF signal is amplified using a power amplifier (PA) before being transmitted via an antenna. At the receiver side, the signal undergoes the reverse process to detect the data bits.

All components of a communication system are comprised of electronic devices, such as transistors, diodes, resistors, and more. However, in reality, no two components are identical due to factors such as temperature, age, and pressure variations, as well as component mismatch. As a result, hardware impairments are inevitable, which can negatively impact system performance. These impairments can include amplifier nonlinearities, I/Q imbalances, quantization noise, and phase noise (PN) in RF oscillators [56].

Phase noise can randomly rotate transmitted symbols, resulting in low bit error rates and poor performance. This random rotation in the frequency domain can cause signal errors and adversely affect signal detection.

Let us consider a single-input single-output (SISO) communication system. The transmitted signal $x(t)$ is

$$x(t) = \sum_{n=0}^{N-1} s[n]p(t - nT), \tag{3.25}$$

where $s[n]$ is the modulated symbol from constellation C, $p(t)$ is a root-raised cosine shaping pulse function with unit energy, and T is the symbol duration. The received baseband signal, $r(t)$, which is affected by the transmitter and receiver oscillator phase noise can be written as

$$r(t) = (x(t)e^{j\phi_t(t)} \circledast h(t))e^{j\phi_r(t)} + w(t) \tag{3.26}$$

where $h(t)$ denotes the channel impulse response in time domain. $\phi_t(t)$ and $\phi_r(t)$ denote the transmitter phase noise and receiver phase noise in time domain, respectively. $w(t)$ is the additive white Gaussian noise (AWGN). For simplicity, we only consider the phase noise at the receiver. Therefore, Eq. (3.26) simplifies to the following equation

$$r(t) = (x(t) \circledast h(t))e^{j\phi(t)} + w(t) \tag{3.27}$$

Assuming that the CP length sufficient to avoid ISI, the received signal in frequency domain is given below

$$R[k] = X[k]H[k]J[0] + \sum_{l=0, l\neq k}^{N-1} X[l]H[l]J[k-l]_N + Z[k], k \in 0, 1, ..., N-1, \tag{3.28}$$

where $[.]_N$ represents modulo N, k is the subcarrier index, N is the size of FFT, $X[k]$ is the k-th transmit symbol in frequency domain, $H[k]$ is the k-th component of the channel frequency response, and Z is the discrete Fourier transform of AWGN. J is the discrete Fourier transformation of the phase noise complex exponential as given below

$$J[l] = \frac{1}{N}\sum_{n=0}^{N-1} e^{j\phi[n]}e^{-\frac{j2\pi nl}{N}}. \tag{3.29}$$

Equation (3.28) highlights the influence of the common phase error (CPE) and inter-carrier interference (ICI) on a system, which results in a PN-dependent rotation of all subcarriers and adjacent interference from other subcarriers within an OFDM symbol, causing potential signal distortion. In practice, pilot subcarriers are frequently utilized to compensate the effects of PN [57]. However, such methods are typically employed for lower carrier frequencies that are less susceptible to ICI as compared to THz frequencies. In Chapter 4, one of these methods from the literature will be reviewed and modified to better accommodate the specific THz band needs in terms of PN.

Table 3.1: Parameters of phase noise model equation [5].

Parameter	Value	Parameter	Value
PSD_0	0.2		
$f_{z,1}$	10^3	$\alpha_{z,1}$	1.4
$f_{z,2}$	200×10^3	$\alpha_{z,2}$	1
$f_{z,3}$	300×10^6	$\alpha_{z,3}$	2.2
$f_{p,1}$	1	$\alpha_{p,1}$	2.2
$f_{p,2}$	650×10^3	$\alpha_{p,2}$	2.5

To model PN accurately, we refer to the 3GPP TR 38.808 document [5]. However, this model only covers carrier frequencies ranging from 52.6 GHz to 71 GHz, and thus is not applicable for THz frequencies. To address this, we use Leeson's equation, as presented in [58], to obtain the PN model for THz frequencies. The PN model in [5] is expressed using a pole-zero model, shown in Eq. (3.30), and the parameters are described in Table 3.1.

$$S(f_o) = PSD_0 . \frac{\prod_{n=1}^{N}(1 + (\frac{f_o}{f_{z,n}}))^{\alpha_{z,n}}}{\prod_{m=1}^{M}(1 + (\frac{f_o}{f_{p,m}}))^{\alpha_{p,m}}}, \tag{3.30}$$

where S is the single sideband phase noise power spectral density, f_o is the offset frequency, $f_{z,1}, ..., f_{z,N}$ are the zeros of the system, $f_{p,1}, ..., f_{p,M}$ are the poles of the system, $\alpha_{z,1}, ..., \alpha_{z,N}$ are the order of the zeros, and $\alpha_{p,1}, ..., \alpha_{p,M}$ are the order of the poles. To fit Eq. (3.30) to the experimental results, the parameters in Table 3.1 were suggested by [5] to be used.

Leeson's expression [58] for single-sideband (SSB) phase noise in dBc/Hz is given in (3.31)

$$L(f_m) = 10log \left[\frac{1}{2} \left(\left(\frac{f_0}{2Q_l f_m} \right)^2 + 1 \right) \left(\frac{f_c}{f_m} + 1 \right) \left(\frac{FkT}{P_s} \right) \right] \tag{3.31}$$

where f_0 is the output frequency, Q_l is the loaded quality factor, f_m is the offset from the output frequency (Hz), f_c is the $1/f$ corner frequency, F is the noise factor of the amplifier, k is Boltzmann's constant in joules/kelvin, T is absolute temperature in kelvins, and P_s is the available power at the sustaining amplifier input.

Based on Eq. (3.31), we can see that if all the parameters and variables stay the

same for two different carrier frequencies f_{0_1} and f_{0_2}, the SSB phase noise ratio of the two different frequencies will be as shown in Eq. (3.32).

$$\begin{aligned}
\frac{10^{\frac{L_2(f_m)}{10}}}{10^{\frac{L_1(f_m)}{10}}} &= \frac{\left(\frac{f_{0_2}}{2Q_l f_m}\right)^2 + 1}{\left(\frac{f_{0_1}}{2Q_l f_m}\right)^2 + 1} \\
&\approx \frac{\left(\frac{f_{0_2}}{2Q_l f_m}\right)^2}{\left(\frac{f_{0_1}}{2Q_l f_m}\right)^2} \\
&\approx \left(\frac{f_{0_2}}{f_{0_1}}\right)^2 \\
&\implies L_2(f_m) - L_1(f_m) \approx 10\log\left(\frac{f_{0_2}}{f_{0_1}}\right)^2 \\
&\implies L_2(f_m) \approx L_1(f_m) + 20\log\left(\frac{f_{0_2}}{f_{0_1}}\right)
\end{aligned} \tag{3.32}$$

In case of using the model provided in [5] for a carrier frequency of 70 GHz, the SSB of the phase noise is the blue curve shown in Fig. 3-5. Using Eq. (3.32), we can get the red curve which is the SSB of the phase noise for a carrier frequency of 300 GHz. Similarly, we can get the phase noise model for other frequencies required for our simulations presented in Chapter 4.

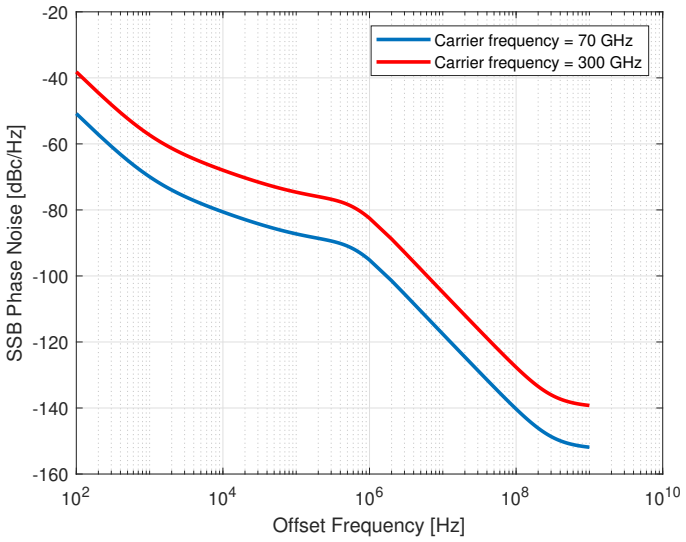

Figure 3-5: SSB of phase noise for two different carrier frequencies. The blue and red curves represent 70 GHz and 300 GHz carrier frequencies, respectively.

Chapter 4

Simulation Results

This chapter presents the simulation results obtained to study the behavior of OFDM and DFT-s-OFDM in the THz band. Through these simulations, we gain a comprehensive understanding of the performance characteristics of these waveforms. The insights gained from these results can be useful for future research and serve as a reference point for the development of other possible waveforms for THz band wireless communication.

4.1 Channel Impulse Response

This chapter simulates the channel impulse responses using the formula presented in Chapter 2. A ray-tracing method is utilized to perform the simulation, with a large room that has four objects such as tables inside it featuring four rough walls serving as the simulation environment. To simplify the simulation, it is assumed that the ceiling and floor do not reflect signals, although parameters for these surfaces could be added with minimal effort. The simulation environment, as depicted in Fig. 4-1, consists of a room measuring $35.9m \times 16.75m \times 5m$. The position of the transmitter antenna (Tx) is $(5m, 5m, 2.5m)$ which means that the Tx antenna is 5 m away from the front wall, 5 m away from the right wall, and 2.5 m away from the ceiling. The receiver antenna (Rx) is d m away from the Tx antenna and the angle between the Tx and the Rx antenna is assumed to be $\pi/3$. This means that the distance between

Table 4.1: The position of each object for different scenarios when the transmission distance (d) varies.

$d = 3$ m	
Object number	Position (m)
1	$(4, 3.2679)$
2	$(3.1519, 7.7990)$
3	$(9.2141, 4.2990)$
4	$(10.75, 14.9593)$
$d = 6$ m	
Object number	Position (m)
1	$(4, 3.2679)$
2	$(3.9019, 9.0981)$
3	$(9.9641, 5.5981)$
4	$(10.75, 14.9593)$
$d = 10$ m	
Object number	Position (m)
1	$(4, 3.2679)$
2	$(4.0359, 11.3301)$
3	$(14.4282, 5.3301)$
4	$(10.75, 14.9593)$

the Rx antenna and the front wall is $5 + d \times sin(\pi/3)$. Similarly, the distance to other walls can be calculated. Based on the transmission distance between the Tx and Rx antennas (d), the position of the other four objects is shown in Table 4.1. It is assumed that these objects do not obstruct the reflections from the walls.

By using this simulation setup, the channel models used in this study are well-defined, enabling a thorough analysis of OFDM and DFT-s-OFDM performance in the THz band. The simulation parameters are summarized in Table 4.2.

Table 4.2: Simulation parameters for THz channel [6].

Wallpaper surfaces	
Parameter	**Value**
Carrier Frequency (f_c)	300 GHz
Correlation Length (l_{corr})	2.3 mm
RMS Height (σ)	0.13 mm

Refractive Index n	$1.53 - j0.059$
Tile Size($l_x = l_y$)	5 cm
Number of Tiles ($M = N = 51$)	51
Wallpaper surfaces	
Parameter	**Value**
Carrier Frequency (f_c)	700 GHz
Correlation Length (l_{corr})	2.3 mm
RMS Height (σ)	0.13 mm
Refractive Index n	$1.45 - j0.1$
Tile Size($l_x = l_y$)	3.5 cm
Number of Tiles ($M = N = 51$)	51

To show the channel impulse response, we also use a root-raised cosine (RRC) pulse to better demonstrate the CIR. The number of samples per pulse is set to be 8. Moreover, the bandwidth of the channel (BW) is set to be 10 GHz. Therefore, the sampling rate (f_s) will be 80 GHz.

Fig. 4-3 depicts all the channel impulse responses used in this thesis for further simulations for six different scenarios.

The line-of-sight (LoS) path is always the strongest path in wireless communication systems. As evidenced in Fig. 4-3, the power of the LoS path is consistently higher than that of other paths. However, this path weakens as the frequency increases, in accordance with Eq. (2.3), which predicts a decrease in the power of the LoS path with higher frequency. In addition, the distance between the transmitter and receiver is a critical factor affecting the strength of the LoS path, as shown by the appearance of distance in the denominator of Eq. (2.3). Therefore, the power of the LoS path depends on both the frequency and the distance between the transmitter and receiver.

These observations have important implications for the design and deployment of wireless communication systems. For example, in order to maintain reliable commu-

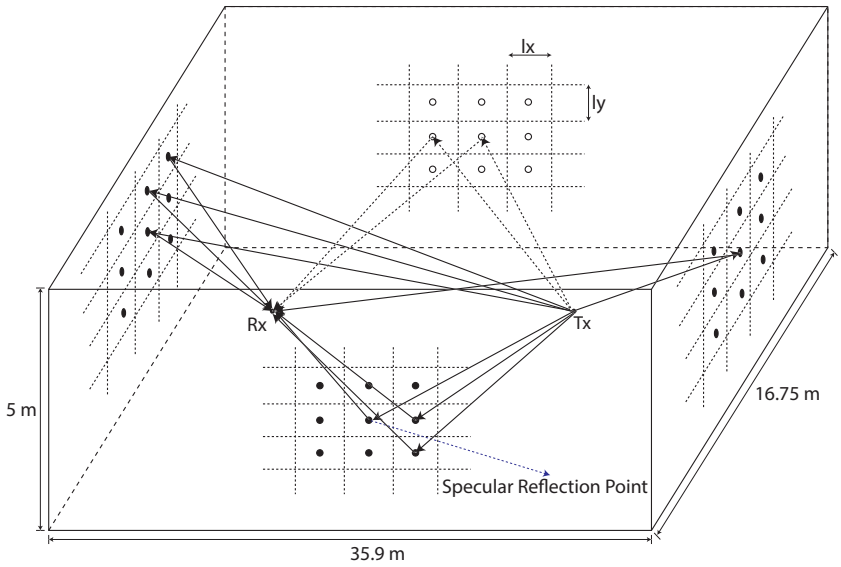

Figure 4-1: Simulation environment without the extra objects.

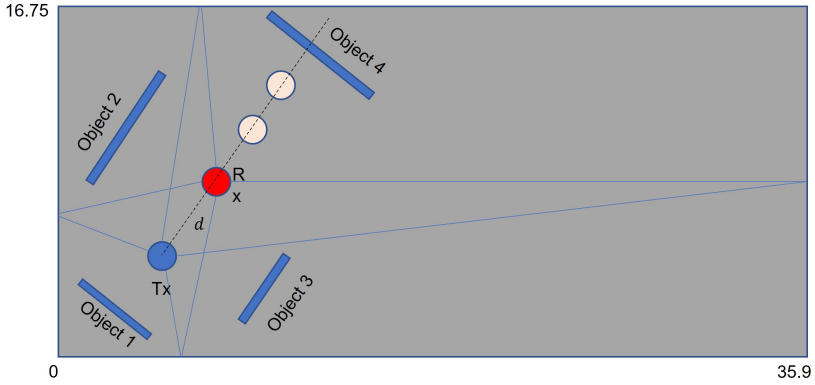

Figure 4-2: Top view of the simulation environments with the extra objects for $d = 3$.

nication, the LoS path may need to be actively maintained by strategic placement of the transmitter and receiver, especially in urban environments where obstacles can obstruct the LoS path. Moreover, since the strength of the LoS path decreases with increasing frequency, communication systems operating at higher frequencies may require more complex signal processing techniques to compensate for the reduced signal strength.

In summary, the power of the LoS path is an important factor to consider in wireless communication systems, and its dependence on frequency and distance highlights the need for careful consideration of these factors in the design and deployment of such systems.

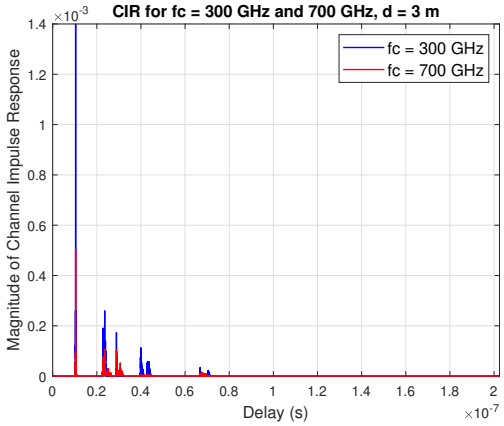

(a) CIR, $f_c = 300$ GHz (blue) and 700 GHz (red) and $d = 3$ m.

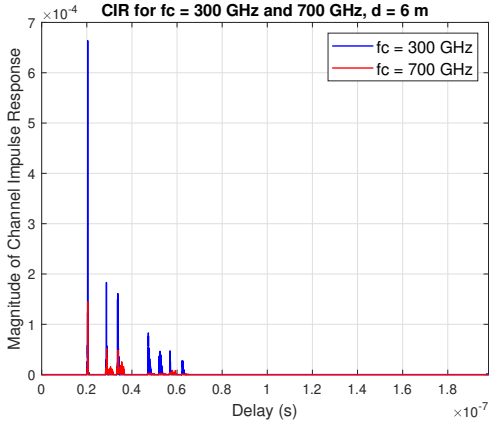

(b) CIR, $f_c = 300$ GHz (blue) and 700 GHz (red) and $d = 6$ m.

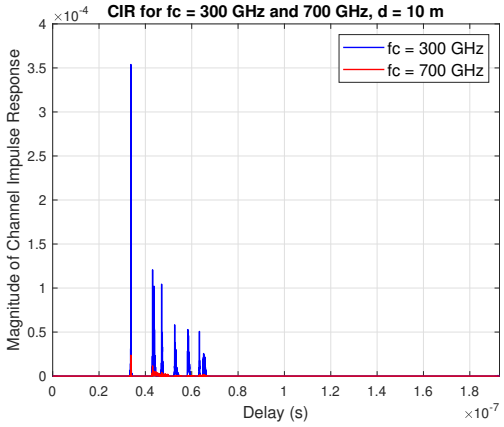

(c) CIR, $f_c = 300$ GHz (blue) and 700 GHz (red) and $d = 10$ m.

Figure 4-3: CIR for three different transmission distances $(3, 6, 10)$ m and two different frequencies $(f_c = 300, f_c = 700)$ GHz.

Another noteworthy observation is that, in general, the power of all paths is lower for the channel that utilizes a carrier frequency of 700 GHz as compared to 300 GHz, as shown in Fig. 4-3. This finding aligns with the formulas presented in Chapter 2, such as Eq. (2.23). Specifically, increasing the carrier frequency results in a higher attenuation of the wireless signal, which can be attributed to various physical phenomena, such as scattering and absorption.

This observation has significant implications for the design and implementation of wireless communication systems that utilize high-frequency carrier waves. In particular, it underscores the importance of signal amplification and other techniques for compensating for the attenuation of the wireless signal.

4.1.1 Root Mean Square (RMS) Delay Spread

In this subsection, we will discuss the RMS delay spread, which is an important metric for characterizing the wireless communication channel's behavior. The RMS delay spread provides information on the spread of signal arrival times, which can help system designers determine the appropriate modulation scheme, coding, and equalization techniques to use in the wireless communication system.

The RMS delay spread is defined as the square root of the second central moment of the power delay profile (PDP) of the wireless channel. The power delay profile is a measure of the power of the received signal as a function of the delay between the original transmitted signal and its various copies. Mathematically, the RMS delay spread (σ_τ) can be expressed as shown in Eq. (4.1) [59]

$$\sigma_\tau = \sqrt{\frac{\sum_k \left((t_k - t_a) - \tau_m\right)^2 a_k^2}{\sum_k a_k^2}}, \tag{4.1}$$

where

$$\tau_m = \sum_k \frac{(t_k - t_a) a_k^2}{\sum_k a_k^2} \tag{4.2}$$

where t_k is the arrival time of path k, the amplitude of path k is shown as a_k, and t_a is the arrival time of the first path.

The RMS delay spread can be used to determine the amount of inter-symbol interference (ISI) that can occur in a wireless communication system due to the spread of the signal arrival times. As the RMS delay spread increases, the duration of the transmitted signal increases, leading to increased ISI and a decrease in the system's capacity. Therefore, the RMS delay spread is an important consideration when designing wireless communication systems.

The length of the cyclic prefix (CP) in a wireless communication system is often determined based on the RMS delay spread. By selecting an appropriate CP length, it is possible to mitigate the effects of inter-symbol interference caused by the time dispersion of the wireless channel.

Table 4.3 presents the RMS delay spread values for various channels at different frequencies and transmission distances, highlighting the importance of carefully considering this parameter when developing wireless communication systems.

Table 4.3: RMS delay spread of various channels.

f_c	d	RMS delay spread (σ_τ)
300 GHz	3 m	7.505 ns
	6 m	9.23 ns
	10 m	8.73 ns
700 GHz	3 m	8.13 ns
	6 m	7.15 ns
	10 m	6.48 ns

As seen in Table 4.3, the RMS delay spread for THz channels simulated in this thesis ranges from 6.48 ns to 9.23 ns. For instance, the RMS delay spread is calculated as 7.505 ns for $f_c = 300$ GHz and $d = 3$ m. This means that the symbol rate for this particular channel is limited to $0.1/\sigma_\tau = 0.013$ Gbit/s to avoid ISI for signals that are linearly modulated. Additionally, the coherence bandwidth is given by $0.2/\sigma_\tau = 0.026$ GHz = 260 MHz. Interestingly enough, the RMS delay spreads for all of these channels are very close to each other with a small difference. The range of the RMS delay spread values reported in Table 4.3 is calculated as $9.23 - 6.48 = 2.75$ ns. Table 4.3 demonstrates that, in general, the root-mean-square (RMS) delay spread decreases as the frequency increases because of the multi-path effect that reduces due to high

path loss for non-line-of-sight (NLoS) rays. However, there is one exception when the transmission distance is 3 meters. Under this condition, the RMS delay spread slightly increases with an increase in frequency. This phenomenon can be explained by referring to Fig. 4-3 (a), where it is observed that the specular reflections are weaker for the 700 GHz channel, but the diffuse scattering is more pronounced, thereby resulting in a slightly larger RMS delay spread. Therefore, we can conclude that the RMS delay spread decreases with the increase in frequency. However, it is essential to consider the environment's geometry in which the channel is simulated.

4.2 Effect of Scattering

One of the unique characteristics of THz channels is the dense diffuse scattering from rough surfaces. The effect of diffuse scattering shall be examined as it can cause a performance gap between OFDM and DFT-s-OFDM. To model no scattering effect, it means that there is only one specular tile on each object that reflects the incident wave. When the effect of scattering is considered, i.e., more than one tile on each object, the incident wave will be scattered in different random directions. As a result, there are more NLoS closely spaced scattered rays.

To study the impact of scattering in the THz band, we deliberately select a channel with a higher carrier frequency of $f_c = 0.7$ THz. Channels with higher carrier frequencies tend to exhibit more pronounced scattering effects [6]. Furthermore, based on the information provided in Table 4.3, it can be observed that among the channels with a carrier frequency of 0.7 THz, the channel with the shortest transmission distance has the largest RMS delay spread. Hence, this particular channel is chosen for investigating the effects of scattering.

It can be seen from Fig. 4-4 that both schemes are adversely affected by scattering, however DFT-s-OFDM is more resilient to the scattering effect of the channel compared to OFDM, making DFT-s-OFDM more suitable for scattering rich THz channels.

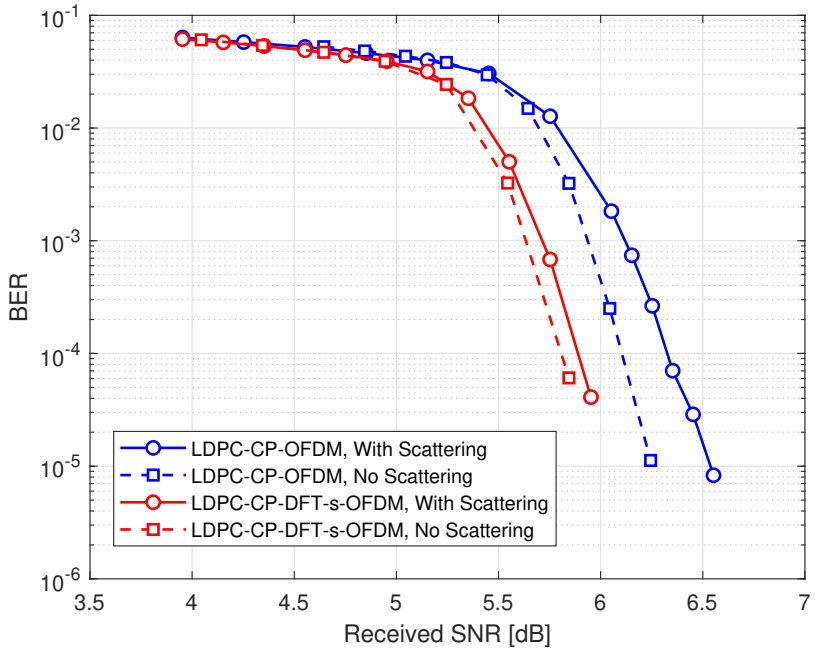

Figure 4-4: BER of LDPC-OFDM (blue) with and without scattering effect compared to LDPC-DFT-s-OFDM (red). $f_c = 0.7$ THz, $d = 3$ m. FFT length = 4096 and CP = 10% of FFT length. Coding Rate = $\frac{2}{3}$.

4.3 CP-OFDM

As a crucial first step in our analysis, we need to determine the appropriate CP length required by the system to avoid or minimize the ISI effect. To accomplish this, we will utilize a simple OFDM code and run it across several different THz channels, as illustrated in Figure 4-3. By analyzing the results of these simulations, we will be able to select the optimal CP length for our system. The specific simulation parameters that we will use for these tests are listed in Table 4.4. By carefully selecting the appropriate CP length based on these simulations, we can ensure that our system operates effectively and minimizes the potential for ISI.

As shown in Table 4.3, the largest RMS delay spread for the channels under test in this chapter is approximately 9.23 ns. Considering a sampling rate of 80 GHz, this delay spread corresponds to 738.4 samples. Assuming an FFT length of 4096, as presented in Table 4.4, the required CP length will be roughly 18% of the FFT length.

Table 4.4: Simulation parameters for an OFDM system.

Parameter	Value
Carrier frequency (f_c)	0.3 and 0.7 THz
Transmission distance	3, 6, and 10 m
Number of objects in the room	4
Number of the walls	4
Material of the surfaces	Wallpaper
FFT Size	4096
Subcarrier spacing	2.44 MHz
Number of samples per pulse	8
Modulation	QPSK-OFDM

We analyze the bit-error-rate (BER) performance of simulated CP-OFDM systems with varying CP lengths. Specifically, we evaluate the system's BER at a specific signal-to-noise ratio (SNR) and measure the impact of CP length changes from 0% up to 25% of the FFT length, in increments of 1%.

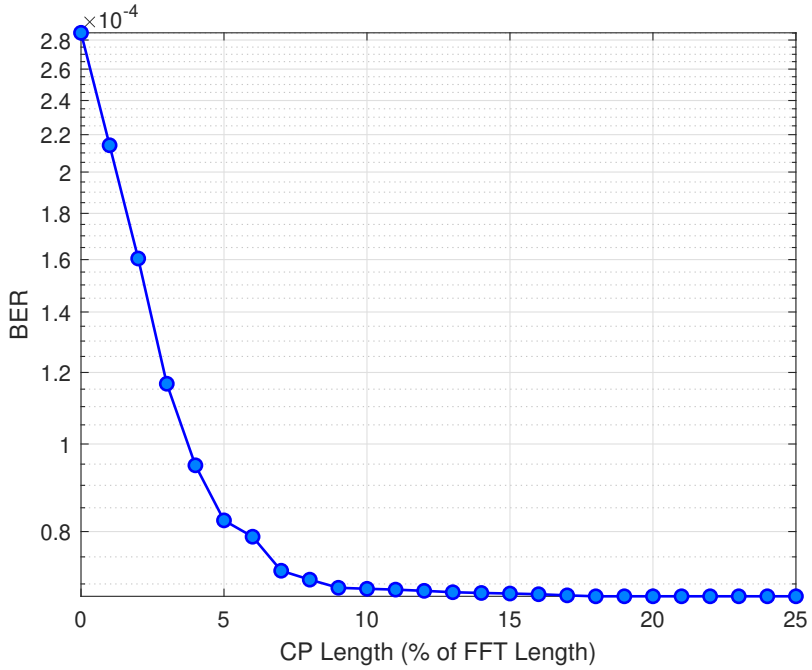

Figure 4-5: Effect of CP Length (0-25% of FFT length) on CP-OFDM BER at SNR = 12.18 dB for $f_c = 300$ GHz, and $d = 3$ m.

In Figure 4-5, we observe the bit error rate (BER) performance of a CP-OFDM system at an SNR of 12.18 dB, with a carrier frequency of 300 GHz and a 3 m distance

between the transmitter and receiver. Notably, increasing the CP length beyond 10% of the FFT length does not result in a significant performance improvement. Hence, we shall use a 10% CP length for future simulations in this specific channel. Further, Figures 4-6 and 4-7 demonstrate the results for channels with a carrier frequency of 300 GHz, and a distance of 6 m and 10 m between the transmitter and receiver, respectively. Therefore, it is safe to use 10% for all simulations when $f_c = 300$ GHz.

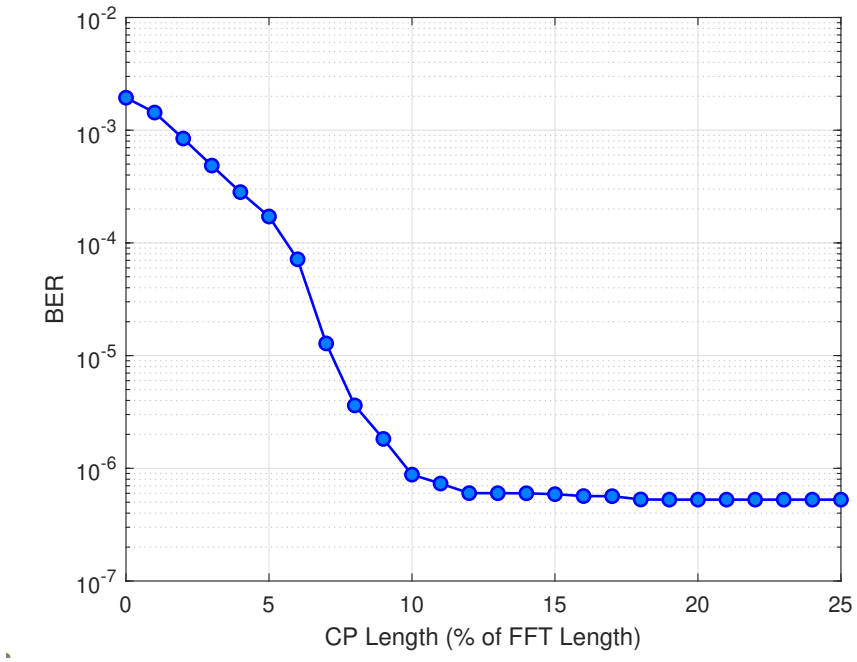

Figure 4-6: Effect of CP Length (0-25% of FFT length) on CP-OFDM BER at SNR = 28.35 dB for $f_c = 300$ GHz, and $d = 6$ m.

Figure 4-8 displays the bit error rate (BER) performance of a CP-OFDM system at an SNR of 18.95 dB, while utilizing a carrier frequency of 700 GHz and sustaining a 3 m distance between the transmitter and receiver. Significantly, increasing the CP length beyond 6% of the FFT length does not result in a substantial performance enhancement. Thus, we recommend implementing a 9% CP length for future simulations in this particular channel. In addition, Figures 4-9 and 4-10 showcase the outcomes for channels with a carrier frequency of 700 GHz, and a distance of 6 m and 10 m between the transmitter and receiver, respectively. It is important to note that this information supports the adoption of a 9% CP length for all simulations when

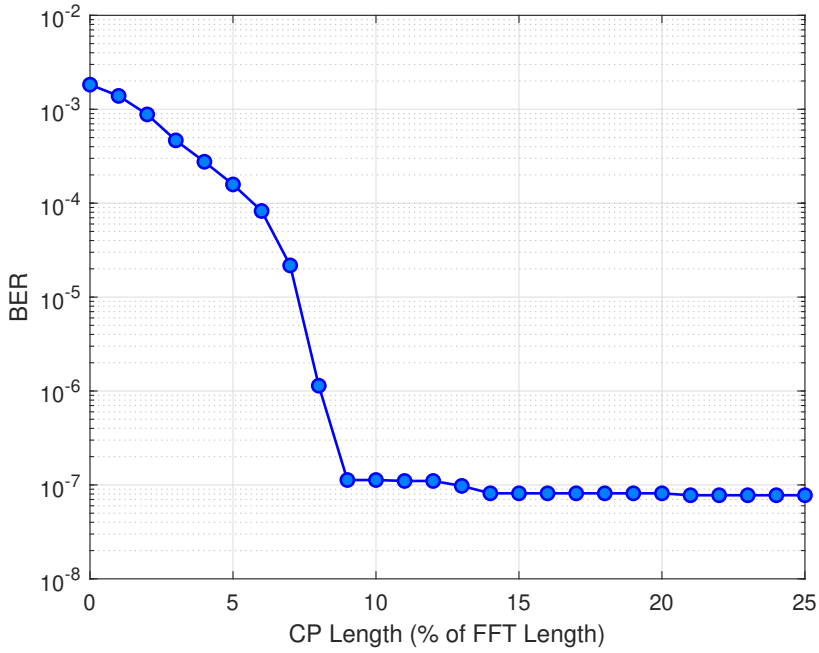

Figure 4-7: Effect of CP Length (0-25% of FFT length) on CP-OFDM BER at SNR = 23.47 dB for $f_c = 300$ GHz, and $d = 10$ m.

$f_c = 700$ GHz.

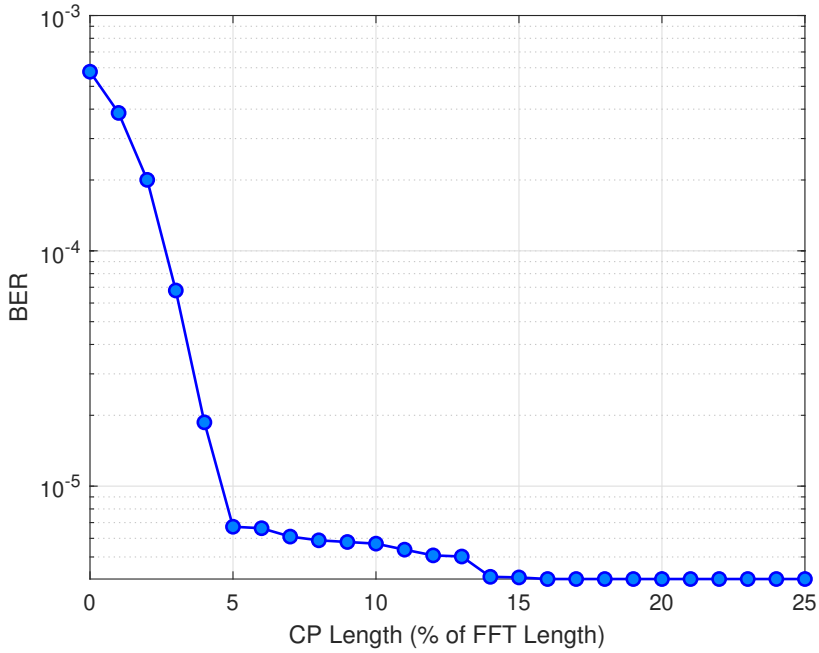

Figure 4-8: Effect of CP Length (0-25% of FFT length) on CP-OFDM BER at SNR = 18.95 dB for $f_c = 700$ GHz, and $d = 3$ m.

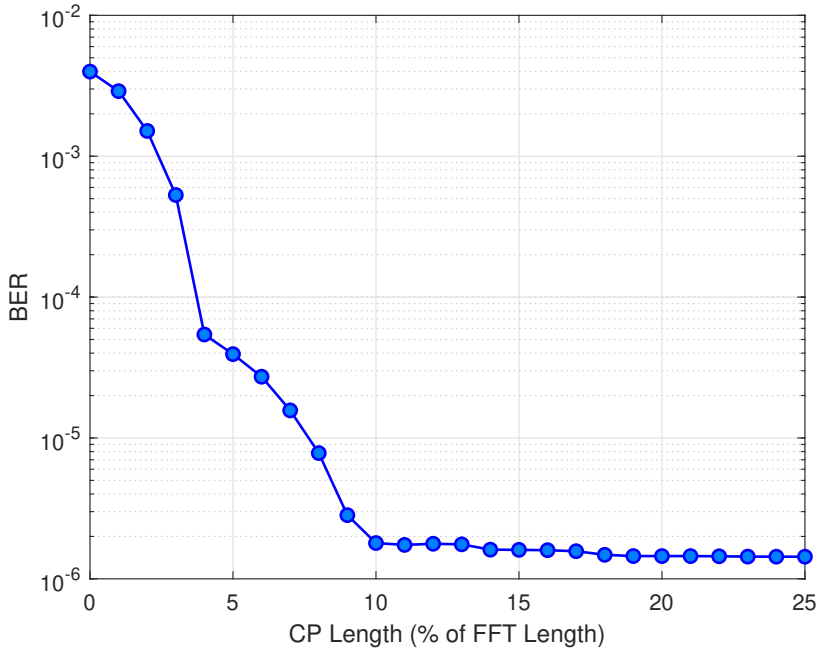

Figure 4-9: Effect of CP Length (0-25% of FFT length) on CP-OFDM BER at SNR = 37.31 dB for $f_c = 700$ GHz, and $d = 6$ m.

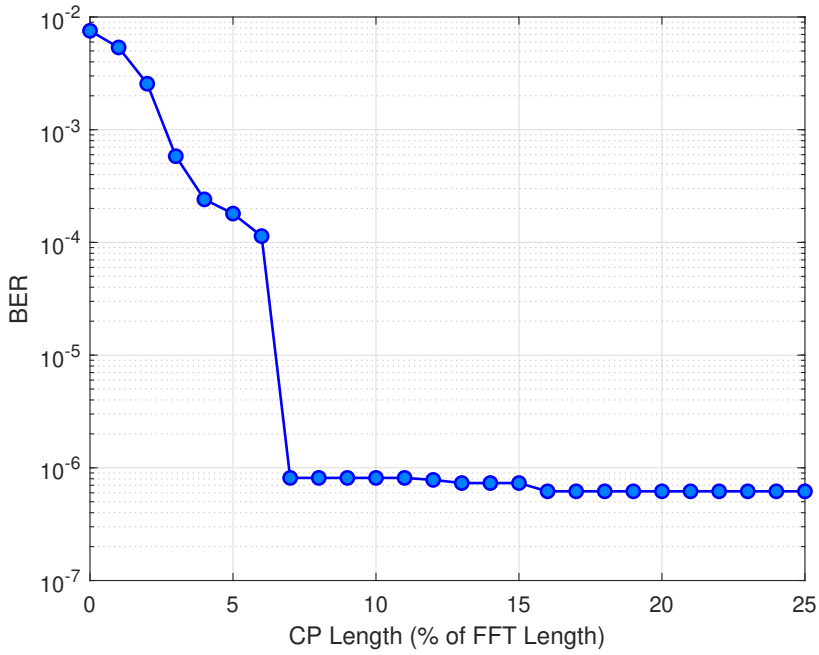

Figure 4-10: Effect of CP Length (0-25% of FFT length) on CP-OFDM BER at SNR = 41.55 dB for $f_c = 700$ GHz, and $d = 10$ m.

By analyzing the bit error rate (BER) performance of CP-OFDM systems at dif-

ferent carrier frequencies and distances, we can draw a conclusion about the optimal cyclic prefix (CP) length for future simulations. In particular, based on the experiments presented in Figures 4-5 and 4-8, it is evident that increasing the CP length beyond 10% and 9% of the FFT length, respectively, does not result in significant performance improvements. Therefore, it is recommended to use a 10% CP length for simulations with a carrier frequency of 300 GHz and a 9% CP length for simulations with a carrier frequency of 700 GHz. Overall, these results suggest that it is safe to use a 10% CP length for all simulations.

Another way of analyzing the CP length is to use spectral efficiency (η_{SE}) instead of BER. When we change the CP length and run the simulations, it means that we are sending a transmission block with a different length. For example, when CP = 0% of the FFT length and the FFT length = 4096, it means that the transmitted block has 4096 symbols. Now, assume the CP length is increased to 25% of the FFT length. Therefore, the length of the transmitted block is calculated as $(1+0.25)\times 4096 = 5120$. Therefore, the energy used to transmit those blocks is not the same. Therefore, one may say that the energies should be the same to perform the BER comparison. To do so, we can calculate the spectral efficiency based on Eq. (4.3)

$$\eta_{SE} = \frac{(1 - BLER) \times N_b}{BW \times T_{tot}}, \tag{4.3}$$

where

$$N_b = log_2(M) \times N_{es} \times R_c \tag{4.4}$$

where N_{es} is the number of effective modulated symbols in one OFDM block, M is the modulation order, and R_c is the channel coding rate which will be equal to 1 for this part of the simulations.

Figures 4-11 to 4-16 depict the spectral efficiency (SE) for different channels. To determine the appropriate cyclic prefix (CP) length for our simulations, we must consider both the SE and bit error rate (BER) curves. For example, when the carrier frequency is 300 GHz and the distance is 3 m, the SE curve in Fig. 4-11 suggests a CP length of 8% of the fast Fourier transform (FFT) length yields the highest SE.

Table 4.5: CP length for CP-OFDM in various THz channels.

f_c	d	CP Length for Highest SE (% of FFT Length)
0.3 THz	3 m	8%
	6 m	9%
	10 m	8%
0.7 THz	3 m	5%
	6 m	9%
	10 m	8%

However, a CP length of 10% achieves the best BER (Fig. 4-5). Ultimately, selecting the optimal CP length requires a trade-off between SE and BER. In this study, we found that a CP length of 10% of the FFT length provides a good balance between BER and SE for the channels under investigation. We will use this CP length in our future simulations.

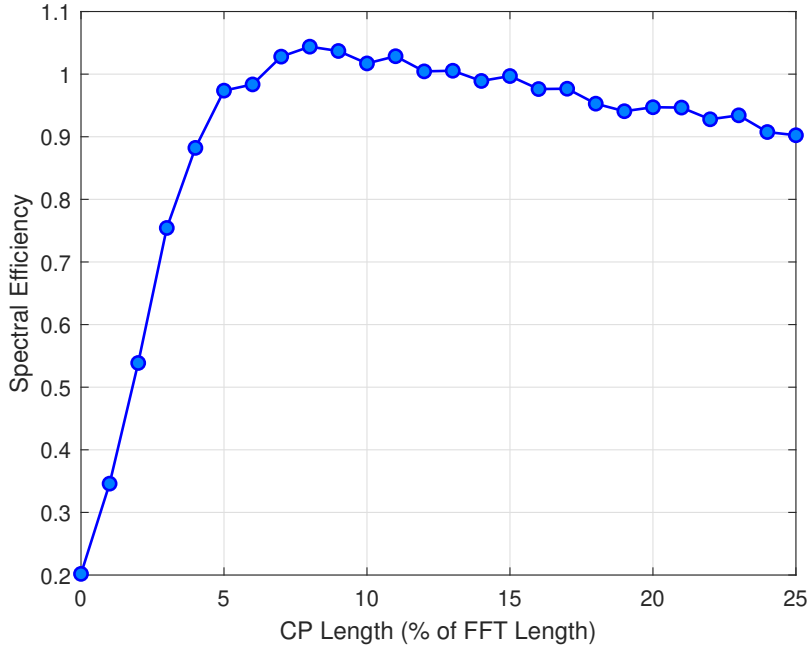

Figure 4-11: Effect of CP Length (0-25% of FFT length) on CP-OFDM spectral efficiency at SNR = 12.18 dB for $f_c = 300$ GHz, and $d = 3$ m.

Table 4.5 summarizes the best CP lengths obtained for each channel based on the SE curves.

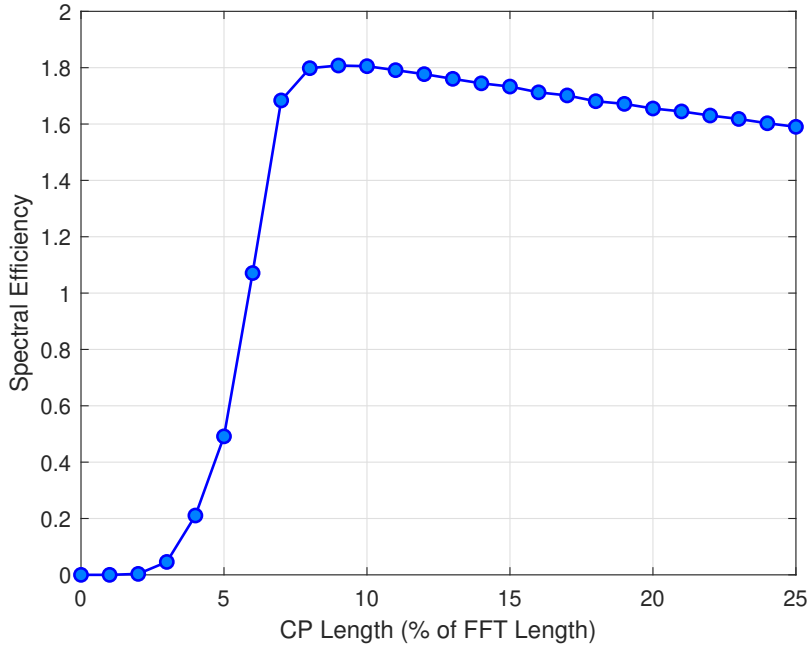

Figure 4-12: Effect of CP Length (0-25% of FFT length) on CP-OFDM spectral efficiency at SNR = 28.35 dB for $f_c = 300$ GHz, and $d = 6$ m.

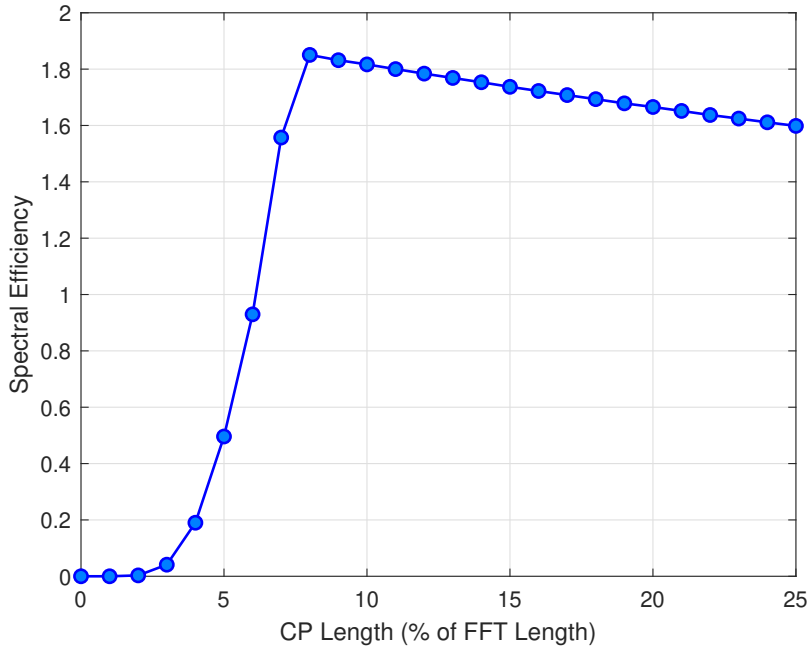

Figure 4-13: Effect of CP Length (0-25% of FFT length) on CP-OFDM spectral efficiency at SNR = 23.47 dB for $f_c = 300$ GHz, and $d = 10$ m.

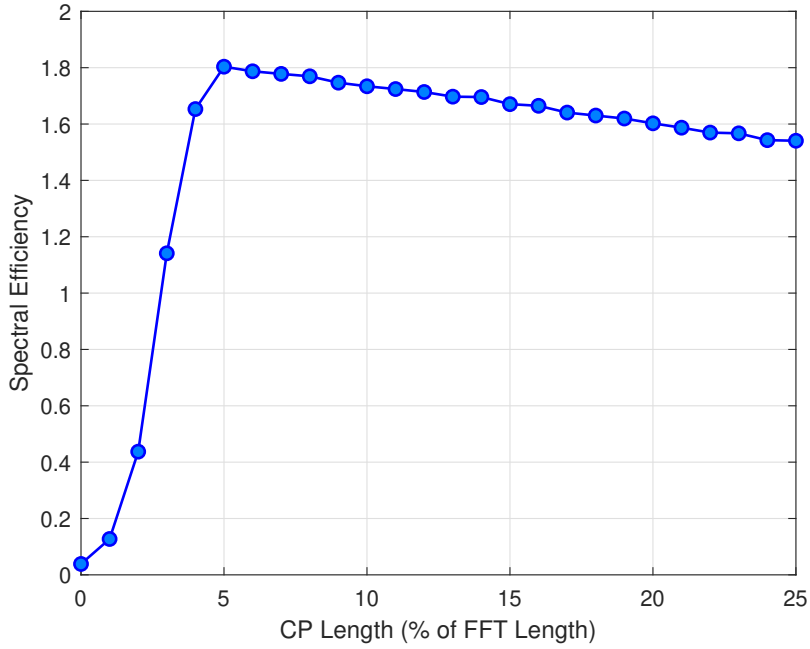

Figure 4-14: Effect of CP Length (0-25% of FFT length) on CP-OFDM spectral efficiency at SNR = 18.95 dB for $f_c = 700$ GHz, and $d = 3$ m.

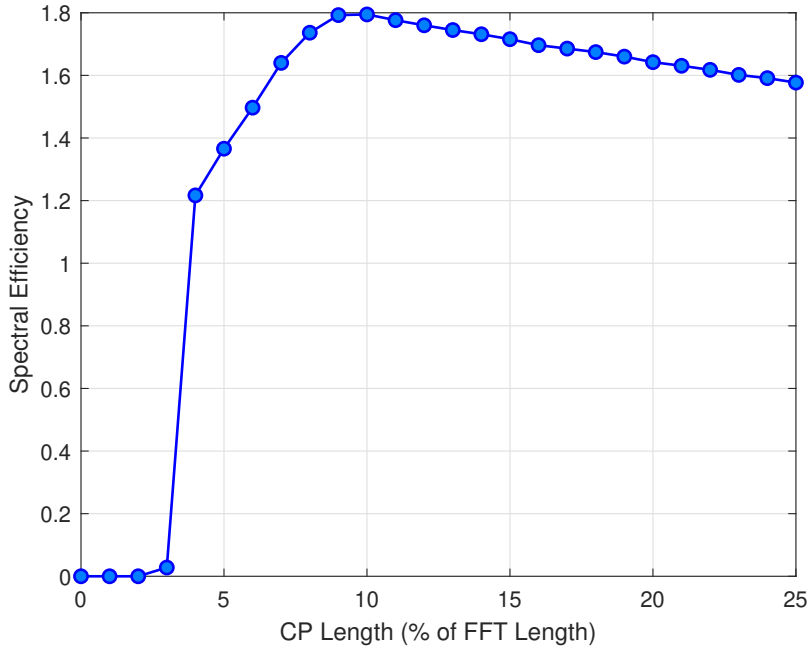

Figure 4-15: Effect of CP Length (0-25% of FFT length) on CP-OFDM spectral efficiency at SNR = 37.31 dB for $f_c = 700$ GHz, and $d = 6$ m.

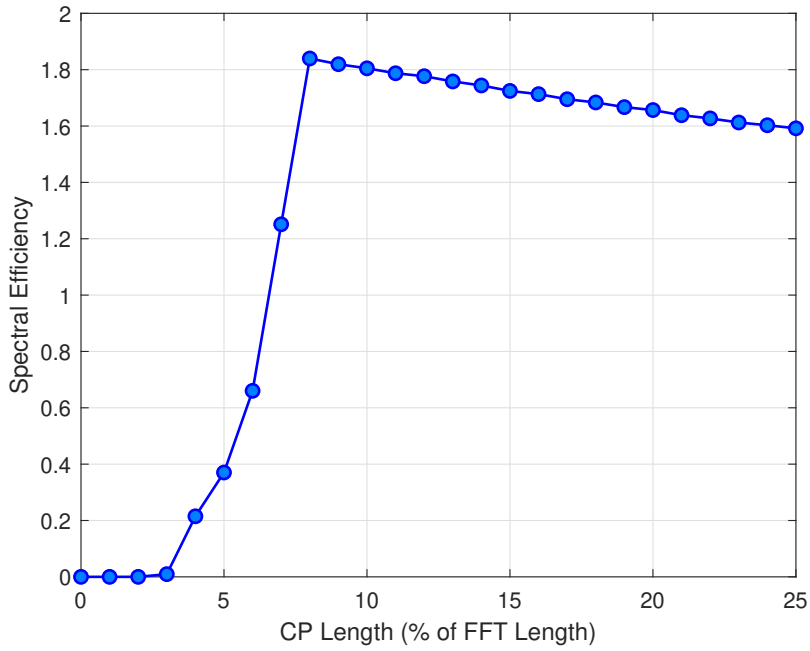

Figure 4-16: Effect of CP Length (0-25% of FFT length) on CP-OFDM spectral efficiency at SNR = 41.55 dB for $f_c = 700$ GHz, and $d = 10$ m.

4.4 CP-DFT-s-OFDM

Based on the findings presented in the previous section, it has been determined that the suitable CP length for CP-DFT-s-OFDM simulation is 10% of the FFT length. The simulation parameters used in this study have been summarized in Table 4.6.

Table 4.6: Simulation parameters for CP-DFT-s-OFDM system.

Parameter	Value
Carrier frequency (f_c)	0.3 and 0.7 THz
Transmission distance	3, 6, and 10 m
Number of objects in the room	4
Number of the walls	4
Material of the surfaces	Wallpaper
FFT Size	4096
Subcarrier spacing	2.44 MHz
CP Length	10% of FFT length
Modulation	QPSK-DFT-s-OFDM
Number of Users	1
Subcarrier Mapping	LFDMA, IFDMA
Equalization Type	ZF, MMSE

Additionally, we have undertaken a comparison of two widely utilized equalization techniques, namely zero forcing equalization (ZF) and minimum mean-square equalization (MMSE). The MMSE method, as per [11], is represented by Eq. (4.5):

$$\mathbf{H}_{\text{mmse}} = (\mathbf{H}^*\mathbf{H} + \frac{\sigma_n^2}{\sigma_x^2}\mathbf{I})^{-1}\mathbf{H}^* \tag{4.5}$$

where $\mathbf{H}_{\text{mmse}}$ is the MMSE equalizer in the frequency domain, $\mathbf{H}$ is the channel frequency response in the DFT domain, σ_n^2 is the noise variance, σ_x^2 is the signal power, and $\mathbf{I}$ is the identity matrix. Alternatively, if the ZF method is chosen, the equalizer in the frequency domain can be represented by a simple expression of $\frac{1}{\mathbf{H}}$.

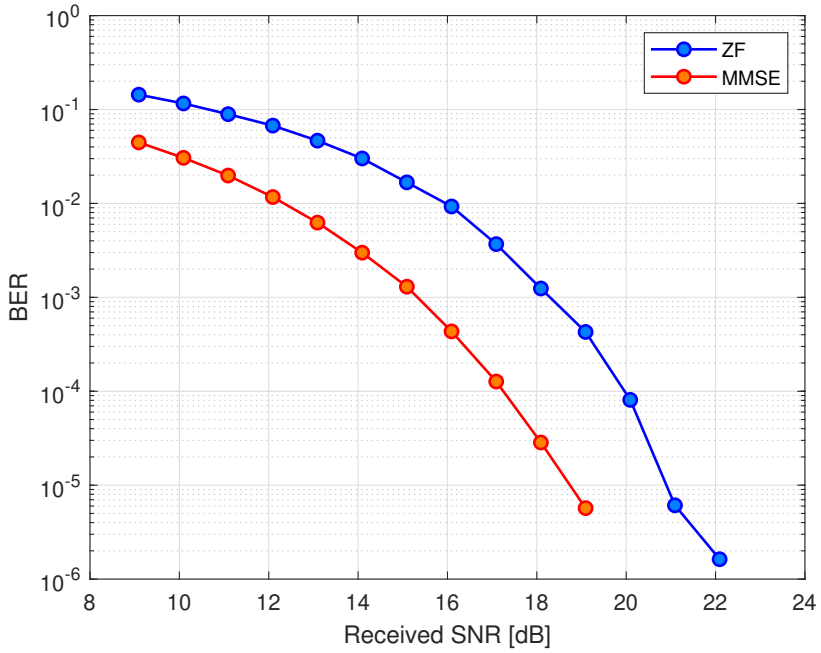

Figure 4-17: BER performance of CP-DFT-s-OFDM when ZF (blue) and MMSE (red) is used. $f_c = 700$ GHz, $d = 6$ m. CP length = 10% of FFT length.

The performance comparison of the MMSE and ZF equalization techniques, as presented in the Fig. 4-17, indicates that the MMSE method exhibits superior performance over the ZF method, especially in situations characterized by low SNR. The reason for the observed performance difference between the MMSE and ZF equalization methods can be attributed to the fact that the MMSE technique, as demonstrated by Eq. (4.5), is better adapted to address noisy environments. In low SNR scenarios,

the impact of noise is lessened within the MMSE equation, while the ZF method tends to magnify the impact of noise, resulting in reduced performance. From now on, only MMSE equalizer will be used.

4.4.1 IFDMA vs. LFDMA

When there is only one user, IFDMA and LFDMA have the same BER, as shown in Fig. 4-18. This graph compares the BER performance of CP-DFT-s-OFDM when using either IFDMA (in blue) or LFDMA (in red) with a CP length equal to 10% of the FFT length, and a spreading factor of $Q = 1$ under the conditions of $f_c = 300$ GHz and $d = 3$ m. The reason is that both IFDMA and LFDMA will occupy the same number of subcarriers in an exactly similar fashion.

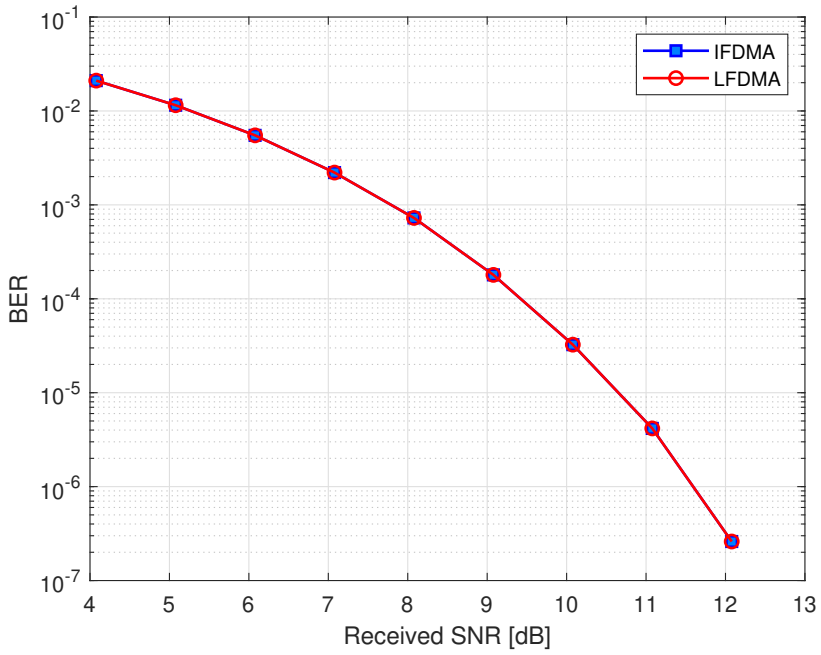

Figure 4-18: BER performance of CP-DFT-s-OFDM when IFDMA (blue) and LFDMA (red) is used. $f_c = 300$ GHz, $d = 3$ m. CP length = 10% of FFT length. Spreading factor $Q = 1$.

However, if the number of users is more than 1, such as when $Q = 4$, then IFDMA and LFDMA will not be the same.

The comparison between the two techniques in terms of their BER performance

for DFT-s-OFDM is not straightforward. The choice between LFDMA and IFDMA depends on the specific system requirements and the trade-offs between various performance parameters such as spectral efficiency, power efficiency, complexity, and flexibility.

By allocating subcarriers that are adjacent to each other to the same user, LFDMA can reduce the interference between the subcarriers and improve the system's performance. LFDMA can also be more flexible in terms of frequency allocation, allowing for more efficient use of the available frequency spectrum.

On the other hand, IFDMA may suffer from higher inter-carrier interference due to the interleaving of subcarriers from different users. The interleaving can lead to subcarriers that are far apart from each other being allocated to the same user, which can result in higher interference between the subcarriers and degrade the system's performance. However, IFDMA can be more power-efficient than LFDMA, as it can reduce the PAPR of the signal. IFDMA can also be more flexible in terms of time-domain resource allocation, as it allows interleaving of subcarriers from different users.

Therefore, the choice between LFDMA and IFDMA for DFT-s-OFDM depends on the specific system requirements and the trade-offs between various performance parameters.

The simulation results presented below were obtained with a spreading factor of $Q = 4$, while keeping all other simulation parameters constant to ensure a fair comparison of bit error rate (BER).

To compare the PAPR of LFDMA and IFDMA and demonstrate that LFDMA has a higher PAPR, we can plot the Complementary Cumulative Density Function (CCDF) against a threshold, denoted as $PAPR_0$. From Fig. 4-22, it can be seen that IFDMA has the best PAPR out of the three waveforms namely IFDMA, LFDMA, and OFDM.

There is a trade-off between achieving a good BER performance and minimizing the PAPR when it comes to using IFDMA or LFDMA. Although the BER performance of LFDMA is slightly better than that of IFDMA, we choose IFDMA for future

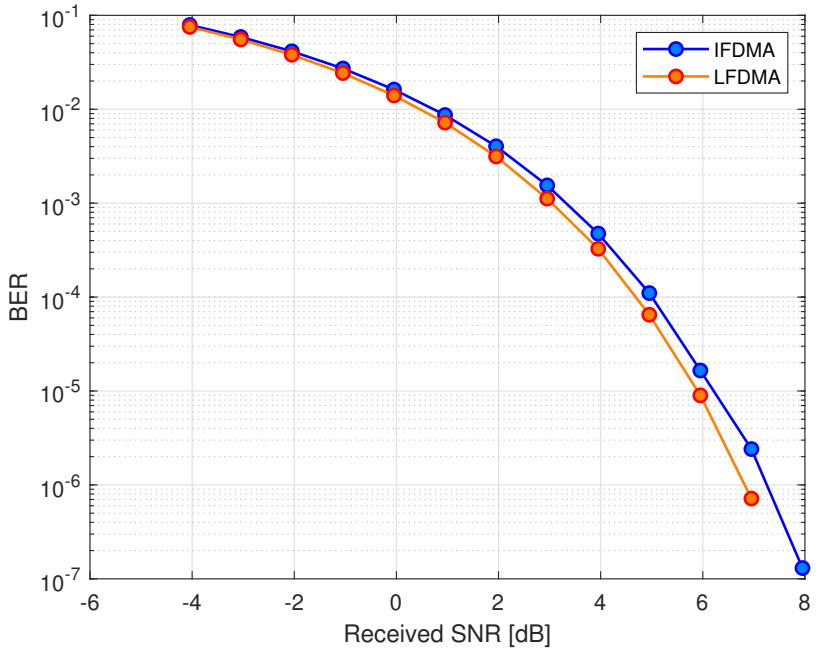

Figure 4-19: BER performance of CP-DFT-s-OFDM when IFDMA (blue) and LFDMA (red) is used. $f_c = 700$ GHz, $d = 3$ m. CP length = 10% of FFT length. Spreading factor $Q = 4$.

simulation results because it exhibits a lower PAPR than LFDMA and the BER is also not that much worse than that of LFDMA.

4.4.2 CP-OFDM vs. CP-DFT-s-OFDM

In this subsection, we evaluate and compare the performance of CP-OFDM and CP-DFT-s-OFDM in various channels under identical simulation conditions. First of all, the BER comparison in AWGN channel is shown in Fig. 4-23. As seen in the mentioned figure, both CP-OFDM and CP-DFT-s-OFDM have the same BER as expected.

CP-OFDM and CP-DFT-s-OFDM have the same BER in AWGN channels because in AWGN channels, the primary source of errors is additive noise, rather than multipath fading or inter-symbol interference (ISI).

In AWGN channels, the signal experiences a flat frequency response and the noise power is distributed equally across all frequencies. This means that all subcarriers

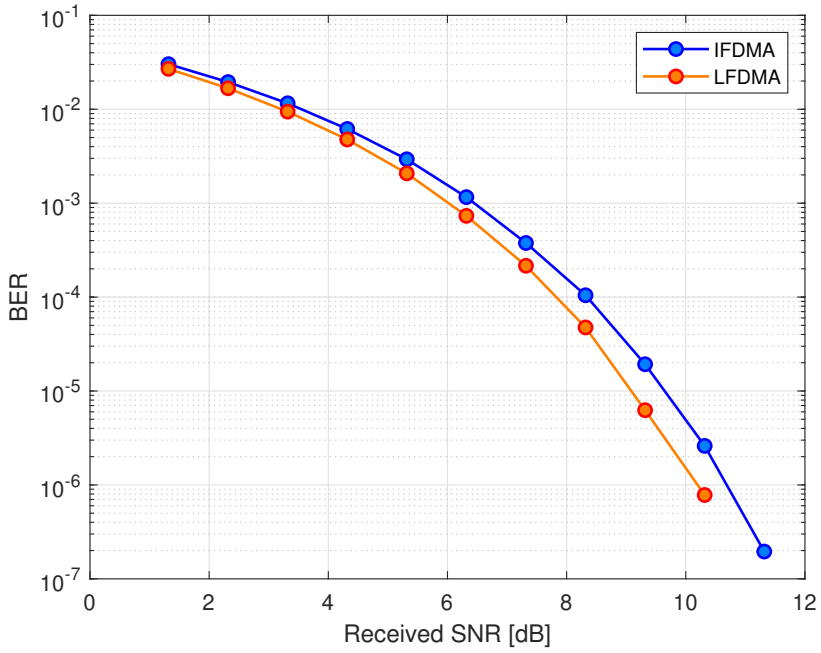

Figure 4-20: BER performance of CP-DFT-s-OFDM when IFDMA (blue) and LFDMA (red) is used. $f_c = 700$ GHz, $d = 6$ m. CP length = 10% of FFT length. Spreading factor $Q = 4$.

in both CP-OFDM and CP-DFT-s-OFDM are affected equally by noise, and neither technique has an inherent advantage over the other in terms of noise tolerance.

In CP-OFDM, the orthogonal subcarriers are designed to be perfectly orthogonal, which means that there is no interference between subcarriers in the absence of noise. In the presence of noise, however, some subcarriers may experience higher noise levels than others, leading to a higher BER.

In CP-DFT-s-OFDM, the DFT-spread technique distributes the signal energy across multiple subcarriers, which can provide better frequency diversity and improve noise tolerance compared to CP-OFDM. However, in AWGN channels, this advantage is not significant, as the noise is uniformly distributed across all subcarriers.

Therefore, in AWGN channels, CP-OFDM and CP-DFT-s-OFDM have the same BER, as the primary factor affecting the BER is the noise, which affects both techniques equally.

Figures 4-24 to 4-26 demonstrate that CP-DFT-s-OFDM outperforms CP-OFDM in terms of BER. This is due to the fact that CP-DFT-s-OFDM employs frequency

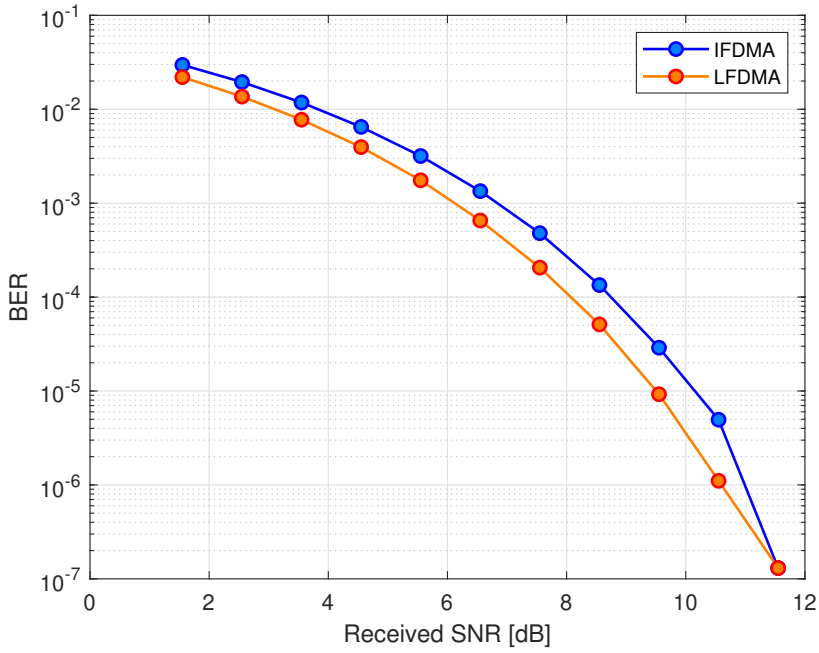

Figure 4-21: BER performance of CP-DFT-s-OFDM when IFDMA (blue) and LFDMA (red) is used. $f_c = 700$ GHz, $d = 10$ m. CP length = 10% of FFT length. Spreading factor $Q = 4$.

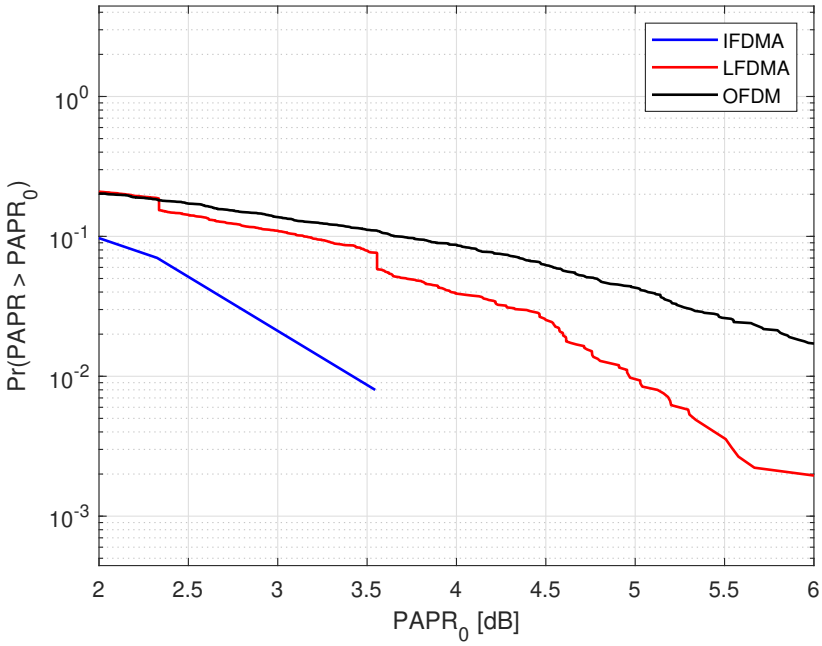

Figure 4-22: PAPR comparison of IFDMA (blue), LFDMA (red) and OFDM (black) with 16QAM.

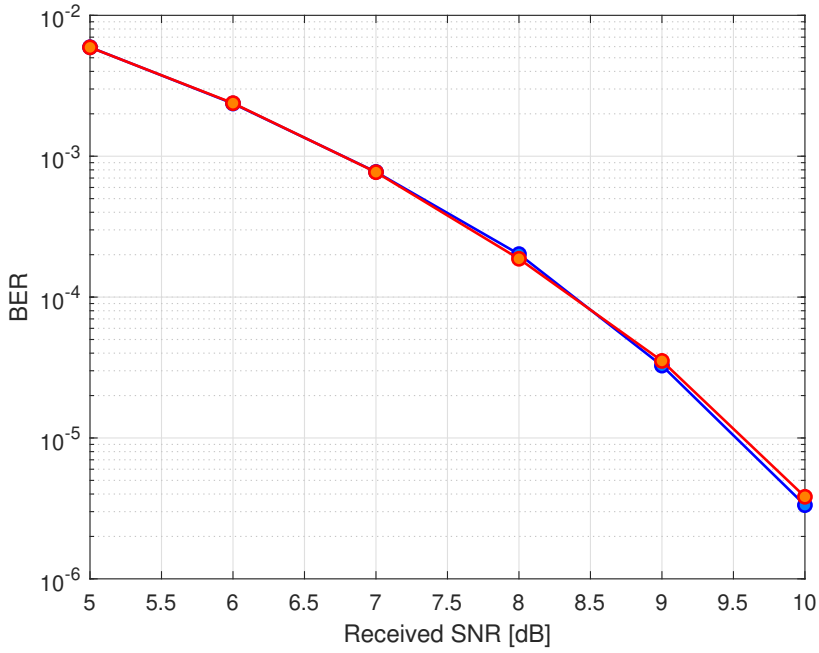

Figure 4-23: BER comparison of CP-OFDM (blue) and CP-DFT-s-OFDM (red) in AWGN channel.

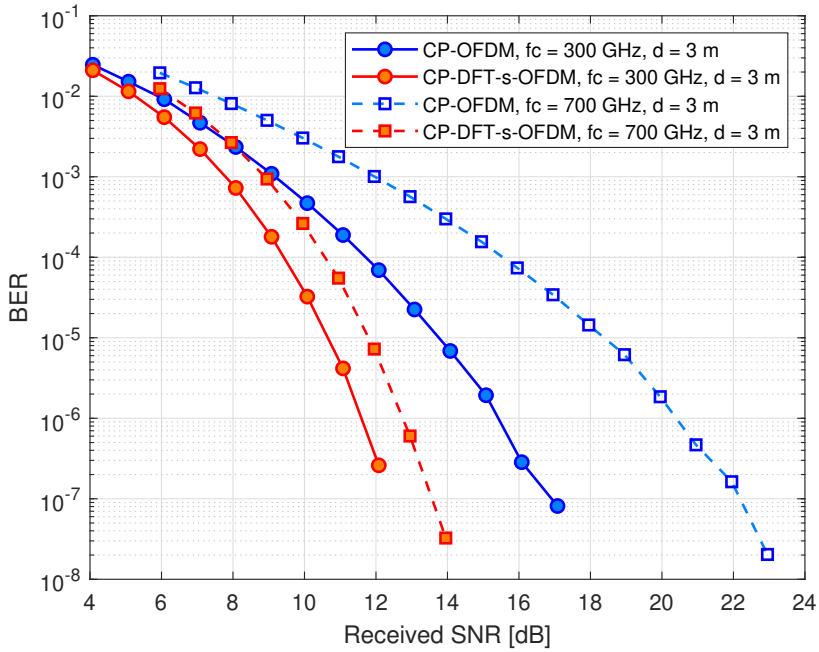

Figure 4-24: BER comparison of CP-OFDM (blue) and CP-DFT-s-OFDM (red) for two different carrier frequencies (300 GHz and 700 GHz) and $d = 3$ m

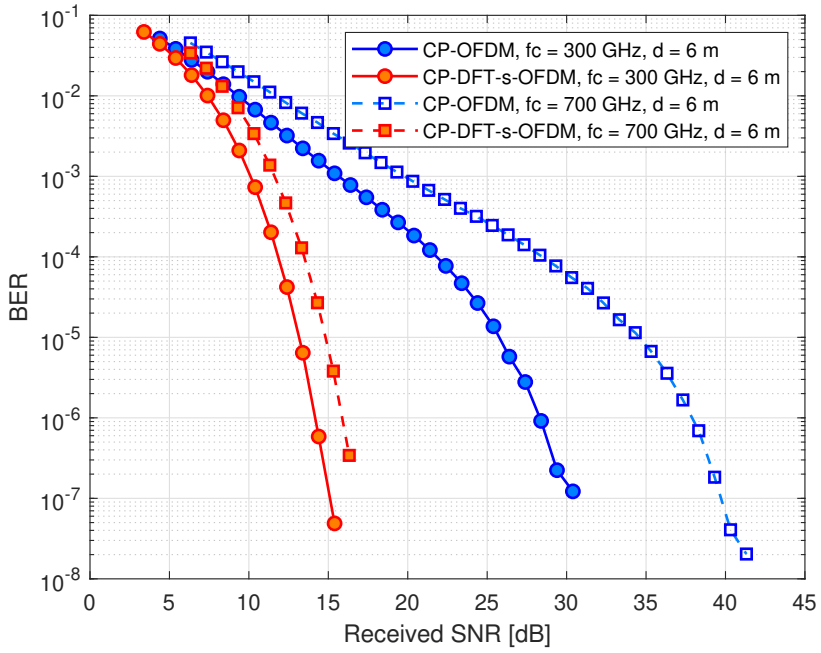

Figure 4-25: BER comparison of CP-OFDM (blue) and CP-DFT-s-OFDM (red) for two different carrier frequencies (300 GHz and 700 GHz) and $d = 6$ m

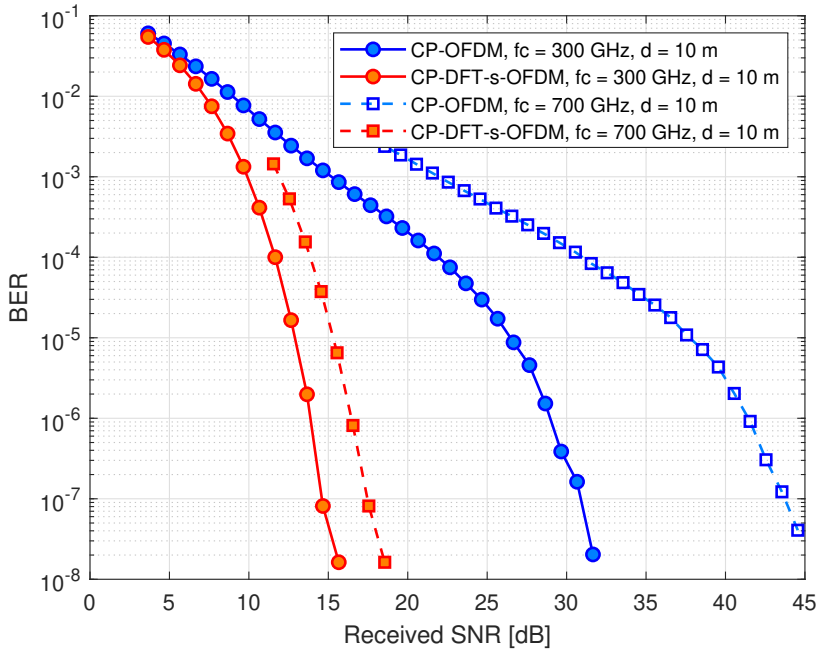

Figure 4-26: BER comparison of CP-OFDM (blue) and CP-DFT-s-OFDM (red) for two different carrier frequencies (300 GHz and 700 GHz) and $d = 10$ m

diversity, whereas CP-OFDM's performance is primarily determined by the worst subcarrier. CP-DFT-s-OFDM modulates the information bit in the time domain, which distributes it across numerous frequency components, resulting in improved performance.

Block error rate (BLER) is an interesting metric that can be preferred over BER in certain scenarios due to several reasons. First, BLER measures the error rate at the block level, which reflects the performance of a communication system over complete blocks of data, making it more relevant for higher-layer protocols or system-level performance. Second, BLER accounts for the impact of errors on entire blocks of data, making it more suitable for communication systems that employ error correction techniques. Finally, BLER provides a practical and realistic measure of system performance in real-world scenarios with varying channel conditions, interference, and noise. For these reasons, BLER curves are shown in addition to the BER curves.

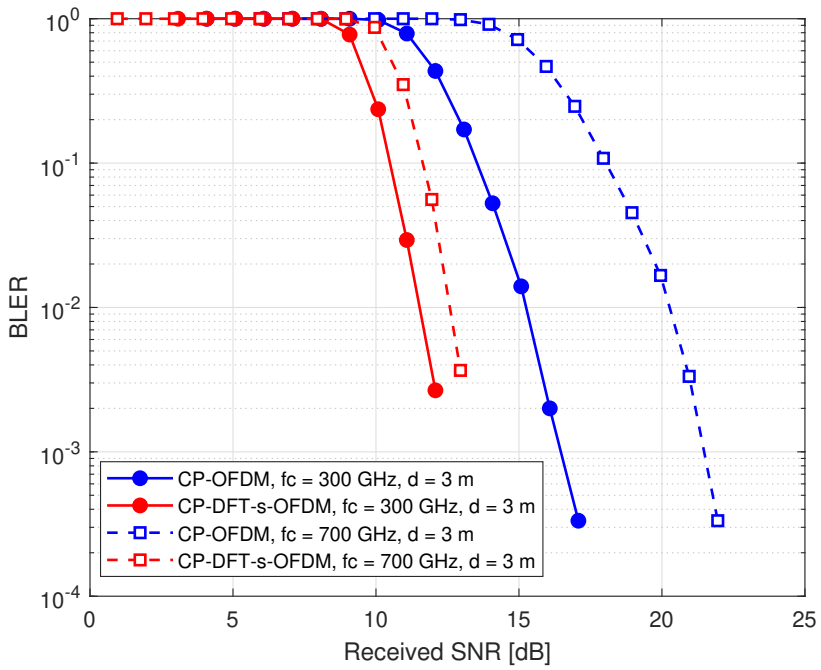

Figure 4-27: BLER comparison of CP-OFDM (blue) and CP-DFT-s-OFDM (red) for two different carrier frequencies (300 GHz and 700 GHz) and $d = 3$ m

The results presented in Figs. 4-27 to 4-29 clearly demonstrate that DFT-s-OFDM outperforms traditional OFDM in the simulated channels. This observation

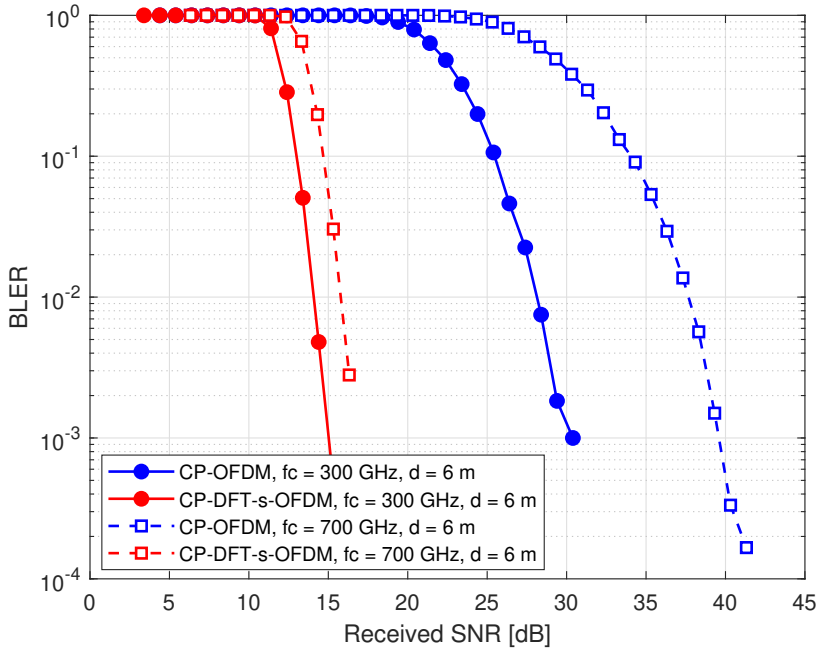

Figure 4-28: BLER comparison of CP-OFDM (blue) and CP-DFT-s-OFDM (red) for two different carrier frequencies (300 GHz and 700 GHz) and $d = 6$ m

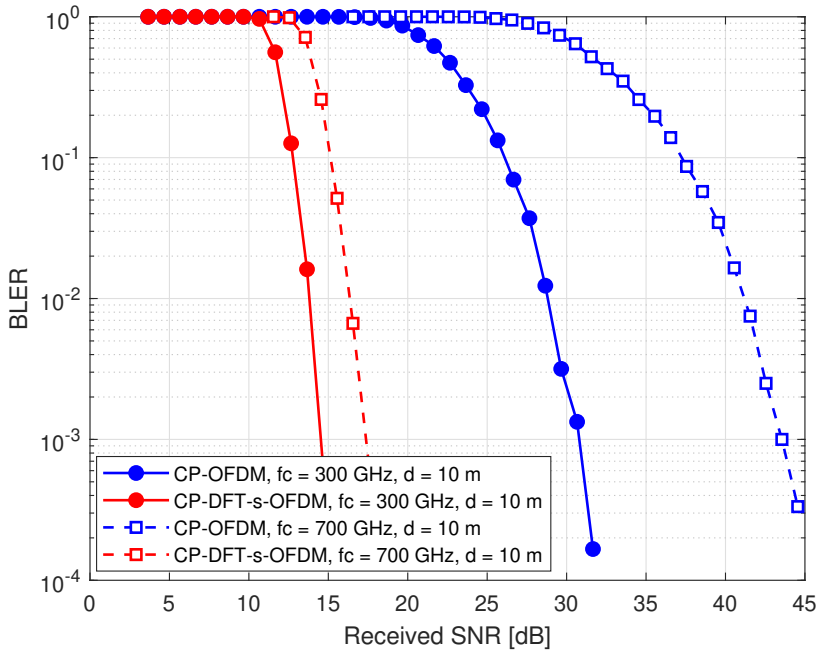

Figure 4-29: BLER comparison of CP-OFDM (blue) and CP-DFT-s-OFDM (red) for two different carrier frequencies (300 GHz and 700 GHz) and $d = 10$ m

is consistent with the well-known limitation of OFDM in terms of frequency diversity. As a result, channel coding becomes necessary for OFDM in order to compensate for this deficiency and improve its performance.

4.5 Coded CP-OFDM and DFT-s-OFDM

In this subsection, we investigate the performance of LDPC codes that are used in the 5G NR standard [60] on the performance of OFDM and DFT-s-OFDM in various channel conditions. LDPC coding is implemented to improve the frequency diversity of CP-OFDM, and we will explore the effects of two different coding rates i.e. $R = \frac{2}{3}$ and $R = \frac{1}{3}$, on the performance of both systems through simulation.

The simulation parameters are summarised in Table 4.7.

Table 4.7: Simulation parameters.

Parameter	Value
Carrier frequency (f_c)	0.3 and 0.7 THz
Transmission distance	3, 6, and 10 m
Number of objects in the room	4
Number of the walls	4
FFT Size	4096
CP Length	10% of FFT Size
Subcarrier spacing	2.44 MHz
Number of samples per pulse	8
Modulation	QPSK
Channel Coding	Uncoded LDPC with Rate = 2/3 LDPC with Rate = 1/3
Code Block (CB) size	Coding rate 2/3, CB = 5632 Coding rate 1/3, CB = 2880
Material of the surfaces	Wallpaper
Correlation Length of the surfaces	2.3 mm
RMS Height of the surfaces	0.13 mm
Refractive Index n_t when $f_c = 0.3$ THz	1.53 - j0.059
Refractive Index n_t when $f_c = 0.7$ THz	1.45 - j0.1

The BER curves in Fig. 4-30 were generated using LDPC coding with a coding rate of $R = \frac{2}{3}$. A comparison between this figure and Fig. 4-24 reveals a signifi-

cant reduction in the performance gap between CP-OFDM and CP-DFT-s-OFDM. This reduction is attributed to the fact that coded CP-OFDM utilizes frequency diversity, resulting in improved performance. In contrast, while CP-DFT-s-OFDM already employs frequency diversity, LDPC coding is not as effective in enhancing its performance as it is for CP-OFDM. Figures 4-31 to 4-35 also show the same trend that LDPC coding will reduce the performance gap between CP-OFDM and CP-DFT-s-OFDM. To further investigate this observation, we present BER and BLER curves for a strong coding rate of $R = \frac{1}{3}$. It is expected that for lower coding rates, i.e., stronger codes, the performance gap between CP-OFDM and CP-DFT-s-OFDM should decrease, which is indeed observed in Figs. 4-36 and 4-37. The same trend was observed when other channels mentioned in Table 4.7 were used. These observations show that OFDM needs a strong channel coding to catch the same performance as DFT-s-OFDM in THz channels simulated in this thesis.

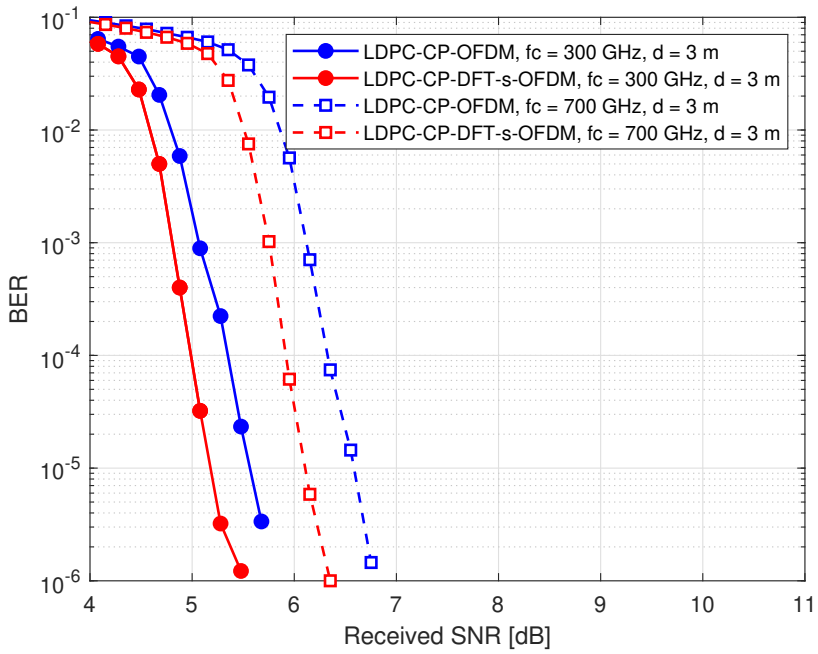

Figure 4-30: BER comparison of LDPC-CP-OFDM (blue) and LDPC-CP-DFT-s-OFDM (red) for two different carrier frequencies (300 GHz and 700 GHz) and $d = 3$ m. Coding Rate $= \frac{2}{3}$.

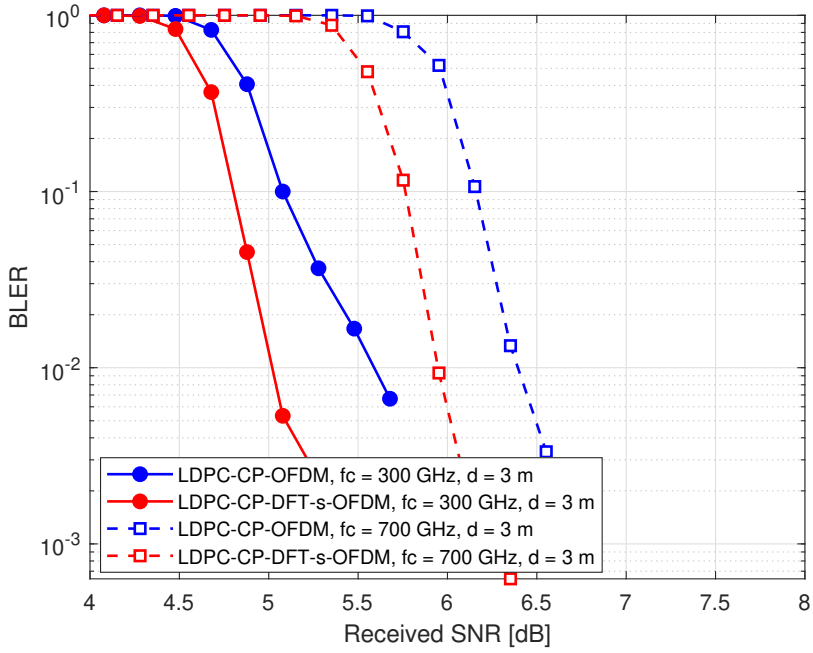

Figure 4-31: BLER comparison of LDPC-CP-OFDM (blue) and LDPC-CP-DFT-s-OFDM (red) for two different carrier frequencies (300 GHz and 700 GHz) and $d = 3$ m. Coding Rate $= \frac{2}{3}$.

4.6 Phase Noise Effect

In this section, we investigate the impact of phase noise on coded CP-OFDM and CP-DFT-s-OFDM in THz communication systems. To achieve this, we use the phase noise model described in Chapter 3, which we scaled up to THz frequencies using Leeson's equation [58]. As the carrier frequency increases, the phase noise levels also increase [58], and theoretically, for frequency multipliers with multiplication ratios of N, the phase noise deteriorates by $20\log_{10}N$ dB [61, 58]. In our simulations shown in Fig. 3-5, we observed that the phase noise of a 300 GHz frequency source is worse than that of a 70 GHz frequency source by around 12 dB, which underscores the severity of the problem.

Our previous sections highlighted that THz channels are highly frequency selective, and OFDM lacks frequency diversity, which led us to conclude that coded CP-DFT-s-OFDM will outperform coded CP-OFDM in THz channels. We also found that the PAPR of DFT-s-OFDM is much lower than that of OFDM, making it a

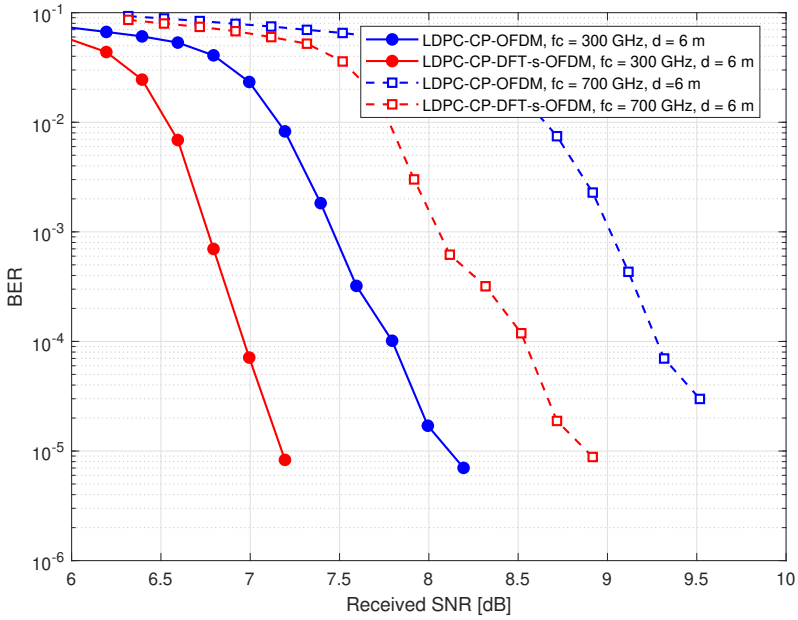

Figure 4-32: BER comparison of LDPC-CP-OFDM (blue) and LDPC-CP-DFT-s-OFDM (red) for two different carrier frequencies (300 GHz and 700 GHz) and $d = 6$ m. Coding Rate $= \frac{2}{3}$.

strong candidate for THz communication systems. However, one of the challenges of using high carrier frequencies is the significant increase in phase noise levels, which can severely impact system performance. Hence, it is crucial to investigate the robustness of CP-OFDM and CP-DFT-s-OFDM to phase noise and determine which one is more resilient. The coding rate will be set to $R = \frac{2}{3}$.

The BER curves depicted in Figs. 4-38 and 4-39 indicate that LDPC-CP-DFT-s-OFDM exhibits greater resilience to phase noise at high carrier frequencies (when PN effect is very severe on the system), such as 700 GHz, when compared to LDPC-CP-OFDM which is another advantage of LDPC-CP-DFT-s-OFDM over LDPC-CP-OFDM.

4.6.1 Phase Noise Estimation and Compensation

To ensure optimal system performance in THz band, phase noise must be estimated and compensated for. Excessive inter-carrier interference (ICI) is a major issue caused by phase noise in this frequency range. In order to maintain low latency in future

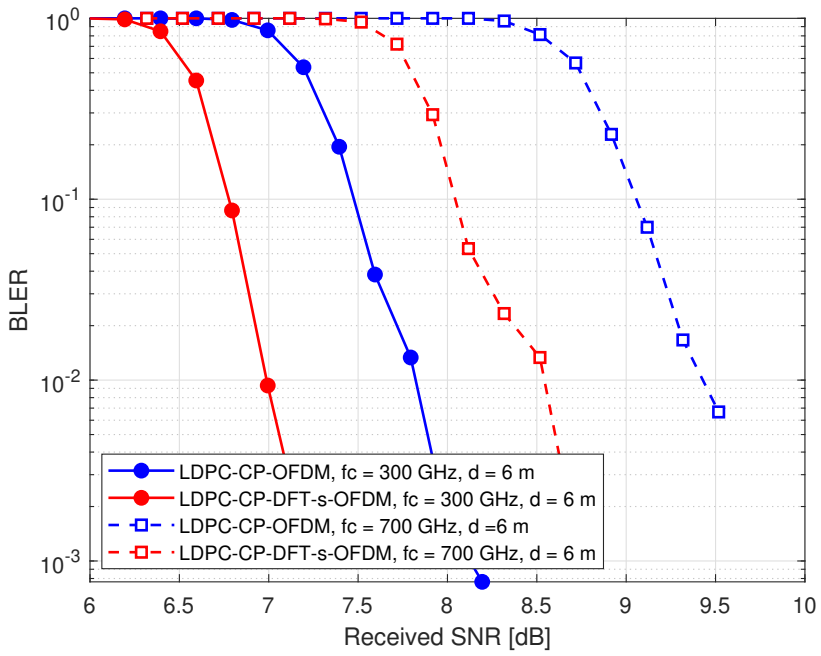

Figure 4-33: BLER comparison of LDPC-CP-OFDM (blue) and LDPC-CP-DFT-s-OFDM (red) for two different carrier frequencies (300 GHz and 700 GHz) and $d = 6$ m. Coding Rate $= \frac{2}{3}$.

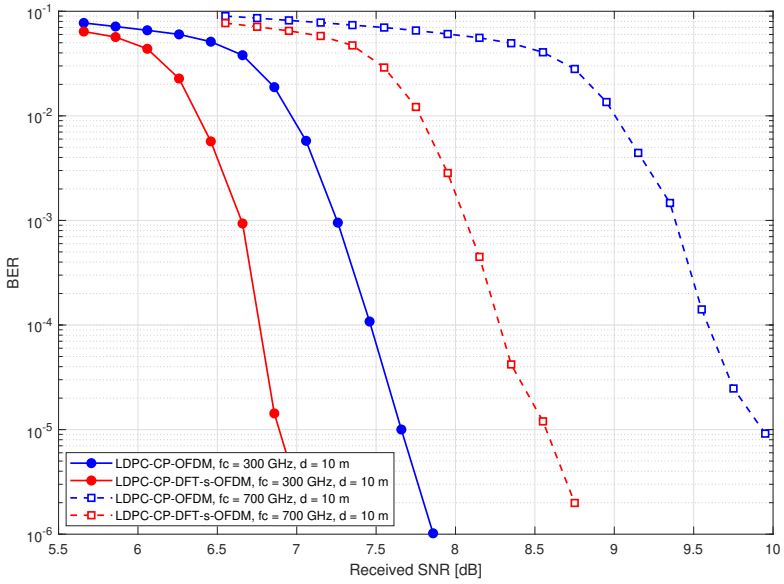

Figure 4-34: BER comparison of LDPC-CP-OFDM (blue) and LDPC-CP-DFT-s-OFDM (red) for two different carrier frequencies (300 GHz and 700 GHz) and $d = 10$ m. Coding Rate $= \frac{2}{3}$.

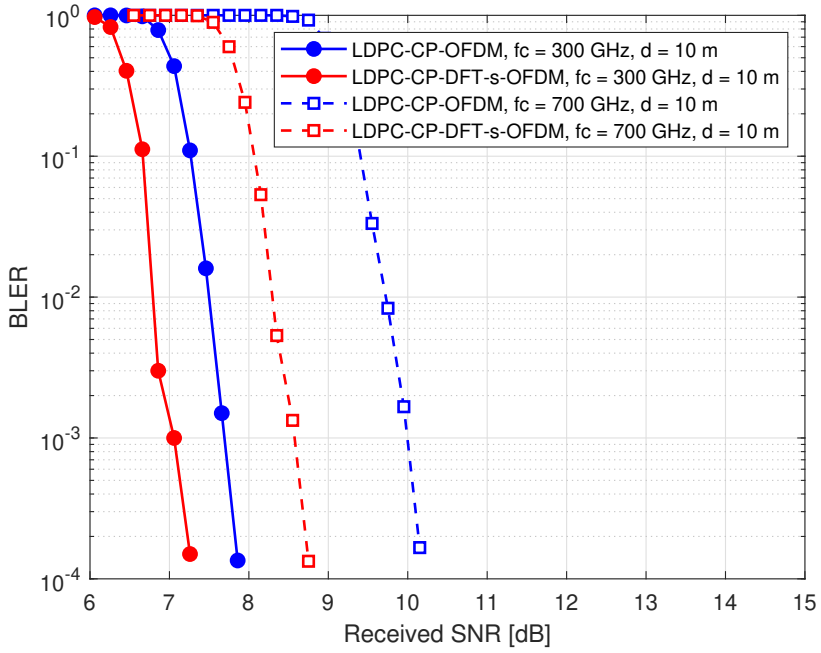

Figure 4-35: BLER comparison of LDPC-CP-OFDM (blue) and LDPC-CP-DFT-s-OFDM (red) for two different carrier frequencies (300 GHz and 700 GHz) and $d = 10$ m. Coding Rate $= \frac{2}{3}$.

6G networks, iterative algorithms for PN estimation and compensation may not be practical. Therefore, we suggest a modified version of a non-iterative method for PN estimation and compensation which was originally proposed in [62].

Phase noise is a dynamic phenomenon that rapidly varies over time. As a result, the complex exponential phase noise ($e^{j\phi}$) in the frequency domain can be considered a narrowband and strongly low-pass process[62]. Consequently, when estimating the PN complex exponential in the frequency domain (i.e., J in Eq. (3.29)), it is sufficient to estimate only the most dominant frequency domain components of the phase noise instead of all of them.

As mentioned in Chapter 3, the received OFDM signal in frequency domain after demodulation can be written as [62]

$$R[k] = X[k]H[k]J[0] + \sum_{l=0, l\neq k}^{N-1} X[l]H[l]J[k-l]_N + Z[k], k \in 0, 1, ..., N-1, \quad (4.6)$$

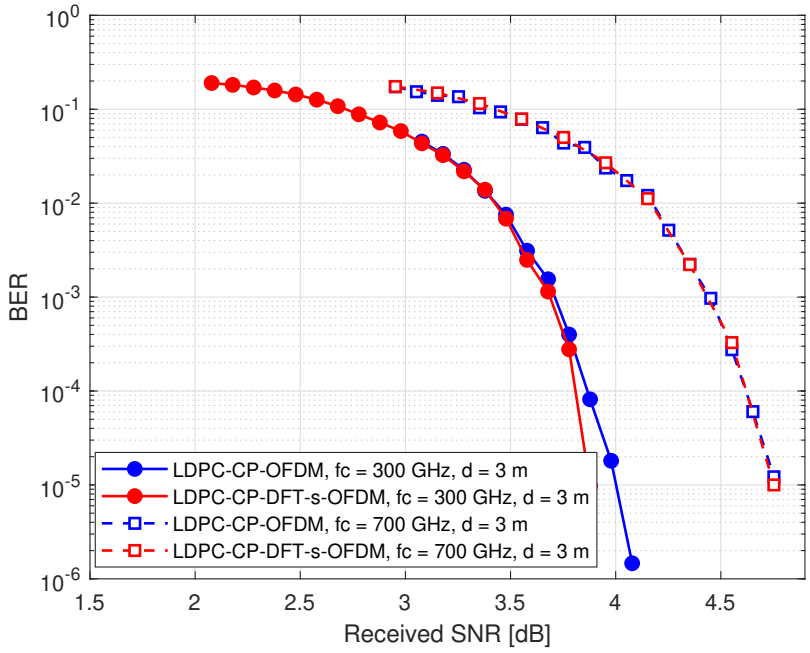

Figure 4-36: BER comparison of LDPC-CP-OFDM (blue) and LDPC-CP-DFT-s-OFDM (red) for two different carrier frequencies (300 GHz and 700 GHz) and $d = 3$ m. Coding Rate $= \frac{1}{3}$.

where J_l is written as in Eq. (3.29).

By considering only the most dominant frequency components located around the center of J, Eq. (4.6) can be simplified to [57]

$$R[k] = \sum_{l=-u}^{u} X[k-l]H[k-l]J[l] + Q_k \tag{4.7}$$

where Q_k includes both ICI from non-significant frequency components of the PN complex exponential and the additive noise. Then, for a set of subcarriers $k \in l_1, l_2, ..., l_p : p \geq 2u + 1$, we can write a set of linear equations as [57]

$$\mathbf{R}_p = \mathbf{Y}_{u,p}\mathbf{J}_u + \mathbf{Q}_p \tag{4.8}$$

where $\mathbf{R}_p \triangleq [R_{l_1}, R_{l_2}, \cdots, R_{l_p}]^T$, $\mathbf{J}_u \triangleq [J_{-u}, J_{-u+1}, \cdots, J_u]^T$, $\mathbf{Q}_p \triangleq [Q_{l_1}, Q_{l_2}, \cdots, Q_{l_p}]^T$, and $\mathbf{Y_{u,p}}$ is written as

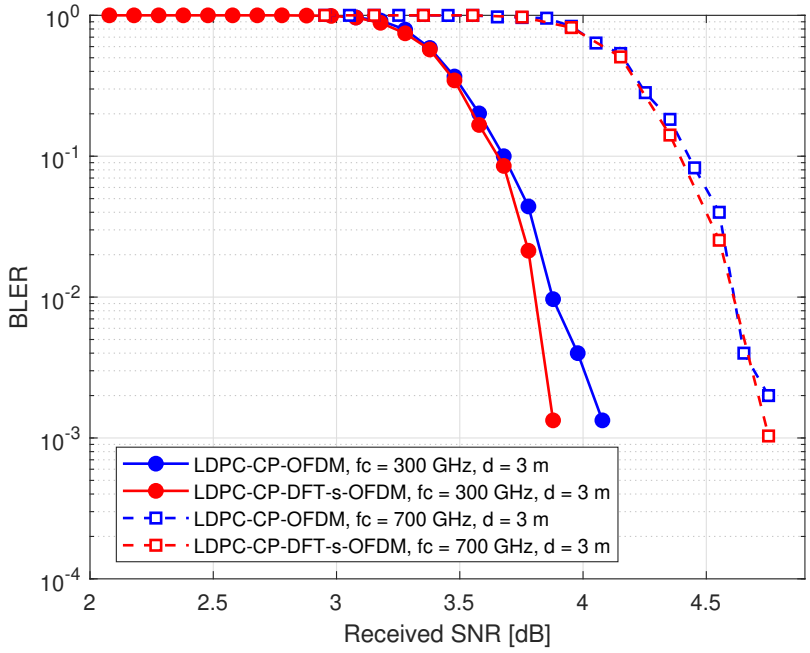

Figure 4-37: BLER comparison of LDPC-CP-OFDM (blue) and LDPC-CP-DFT-s-OFDM (red) for two different carrier frequencies (300 GHz and 700 GHz) and $d = 3$ m. Coding Rate $= \frac{1}{3}$.

$$\mathbf{Y_{u,p}} \triangleq \begin{bmatrix} Y_{l_1+u} & Y_{l_1+u-1} & \cdots & Y_{l_1-u} \\ Y_{l_2+u} & \ddots & \ddots & Y_{l_2-u} \\ \vdots & \ddots & \ddots & \vdots \\ Y_{l_p+u} & \cdots & \cdots & Y_{l_p-u} \end{bmatrix} \tag{4.9}$$

If we assume that the values of $\mathbf{Y_{u,p}}$ are known, which is true if the channel state information (CSI) is perfectly known and also the values of $X[k]$ at $k \in l_1, l_2, \cdots, l_p$ are known because they are the pilot subcarriers, we can write the least square (LS) approach mentioned in [62] to obtain the estimate of $\mathbf{J_u}$ as

$$\hat{\mathbf{J}}_u \triangleq [\hat{J}_{-u}, \cdots, \hat{J}_u]^T = (\mathbf{Y}_{u,p}^H \mathbf{Y}_{u,p})^{-1} \mathbf{Y}_{u,p}^H \mathbf{R}_p, \tag{4.10}$$

where $(\cdot)^T$ and $(\cdot)^H$ denote the transpose and conjugate transpose, respectively.

The proposed pilot allocation in [62] specifies that the pilot subcarrier indices are chosen as $[l_1, l_2, \cdots, l_p] = [n+u, n+u+1, \cdots n+b-u-1]$, where n is typically the

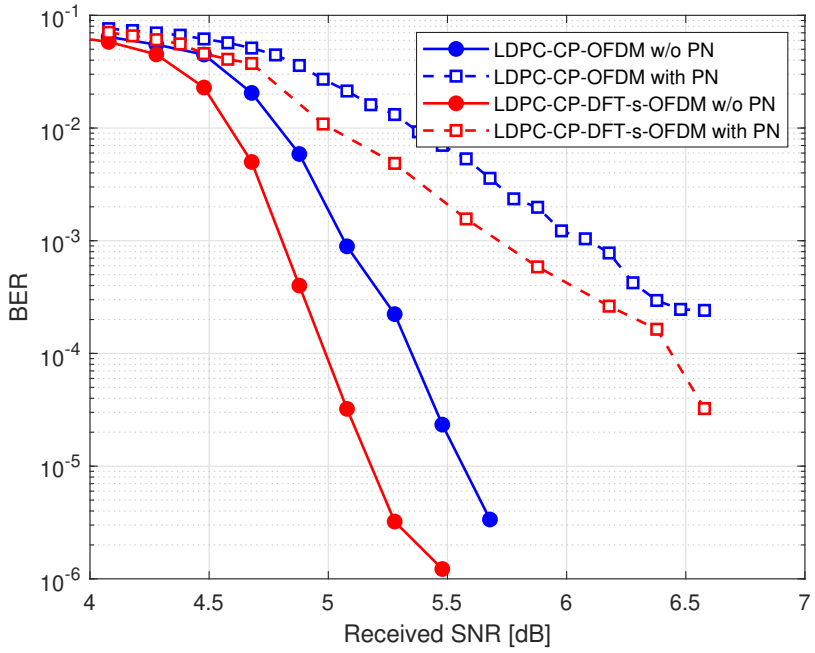

Figure 4-38: BER comparison of LDPC-CP-OFDM (blue) and LDPC-CP-DFT-s-OFDM (red) for two cases with and without PN. $f_c = 300$ GHz and $d = 3$ m. Coding Rate $= \frac{2}{3}$.

index of the center subcarrier of the received signal in the frequency domain, and b is the length of the subcarrier block, satisfying the condition $b \geq 4u + 1$ to ensure sufficient equations for solving the $2u + 1$ unknown components of J. The authors of [62] suggest using the equalized $\mathbf{R_{eq}}$ and $\mathbf{X}_{u,p}$ in Eq. (4.10) instead of $\mathbf{R}_p$ and $\mathbf{Y}_{u,p}$, respectively. After obtaining $\hat{\mathbf{J}}_\mathbf{u}$, using deconvolution to suppress the phase noise [57], the PN-compensated signal is expressed as

$$\hat{Y}[k] = \sum_{l=-u}^{u} R[k-l]\hat{J}[-l]^*, \tag{4.11}$$

where $(\cdot)^*$ denotes the complex conjugate of x.

The PN-compensated signal, $\hat{Y}$, must undergo equalization to detect the data bits. However, two issues can be addressed to improve system performance. Firstly, using the equalized received signal is unnecessary when the channel is known. If the equalized signal is used, additional equalization is needed after obtaining $\hat{Y}$ to enable bit detection. This redundant step introduces extra error, so it is better to use the

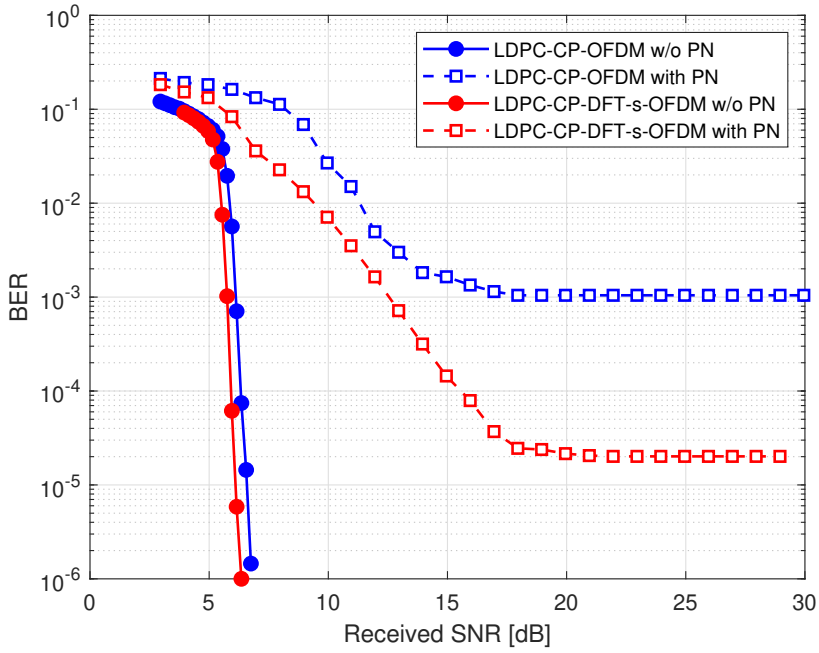

Figure 4-39: BER comparison of LDPC-CP-OFDM (blue) and LDPC-CP-DFT-s-OFDM (red) for two cases with and without PN. $f_c = 700$ GHz and $d = 3$ m. Coding Rate $= \frac{2}{3}$.

unequalized signal. Secondly, the deconvolution process misses the first and last $u-1$ subcarriers. When $u = 3$ in Eq. (4.11), subcarrier index k starts at 3, causing the first 2 subcarriers to be uncompensated for PN. This leads to degraded BER performance. To address this issue, we propose using a circular convolution (Cconv) function instead of deconvolution. This approach compensates all subcarriers, resulting in improved BER performance. To use the Cconv function instead of deconvolution, the inputs are the same with a minor difference: $\hat{\mathbf{J}}$ is zero-padded at the beginning and end to match the length of the received signal. This ensures that the energy of $\hat{\mathbf{J}}$ is concentrated around the center, making it a low-pass process.

To do the simulations, we need to find the best u for the PN model used. The simulation results below, show the BER after PN compensation against the value of u at a specific SNR. We choose the u that results in the lowest BER at SNR $=$ 11.07 dB. Based on the BER curve shown in Fig. 4-40, $u = 3$ results in the lowest BER. Increasing u from 1 to 3 will improve the BER but if u is bigger than a certain amount, the BER will get worse. Since b is fixed, increasing u means that we have

the same number of equations for a larger number of unknowns which is not good for the BER. However, u cannot be too small either as we need to estimate the dominant components of PN in frequency domain.

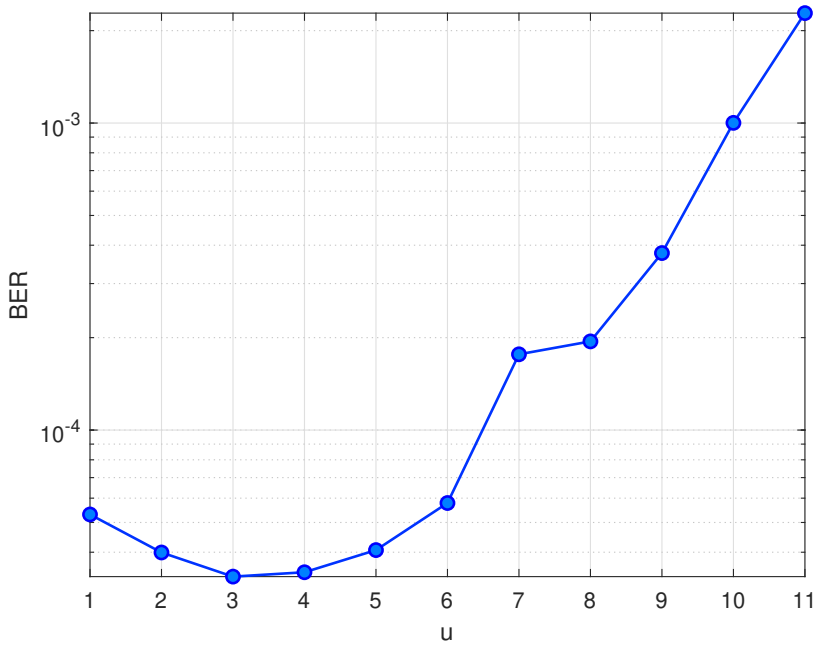

Figure 4-40: BER of LDPC-CP-DFT-s-OFDM at SNR = 11.07 dB when PN is compensated using the modifications mentioned in this section. $f_c = 300$ GHz and $d = 3$ m. Coding Rate = $\frac{2}{3}$.

Figures 4-41 to 4-45 were obtained using $(u = 3, b = 64)$ and perfect channel knowledge. It can be seen from these figures that using circular convolution will compensate the phase noise in various channels better.

Discussion on Simulation Results

In this chapter, a thorough analysis of the performance of two main THz waveform candidates, namely OFDM and DFT-s-OFDM, was presented. Based on the simulation results, DFT-s-OFDM showed to have more advantages than OFDM in terms of lower PAPR, better BER and BLER performance, and more resilience to the effect of phase noise.

There are multiple reasons why DFT-s-OFDM performed very well compared to

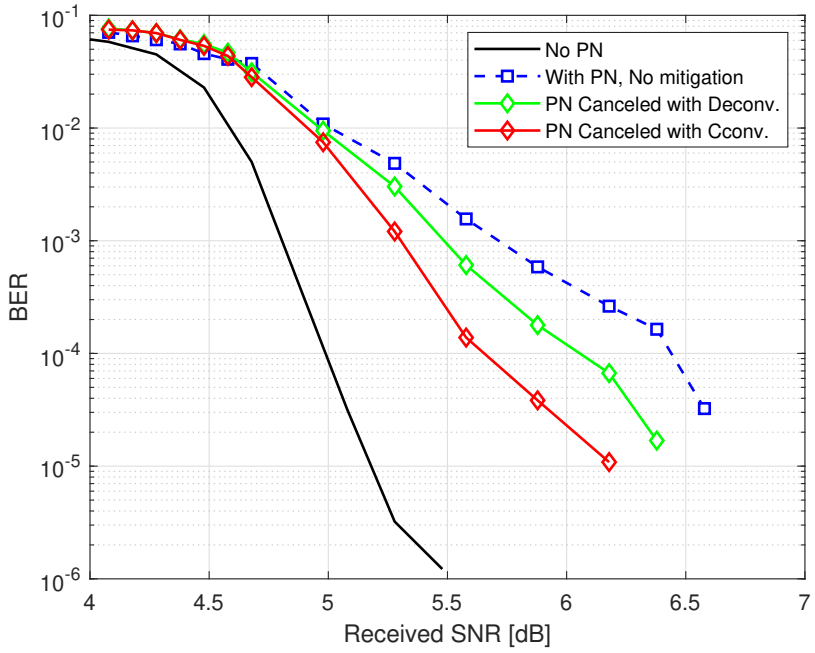

Figure 4-41: BER of LDPC-CP-DFT-s-OFDM. $f_c = 300$ GHz and $d = 3$ m. Coding Rate $= \frac{2}{3}$. $(u = 3, b = 64)$.

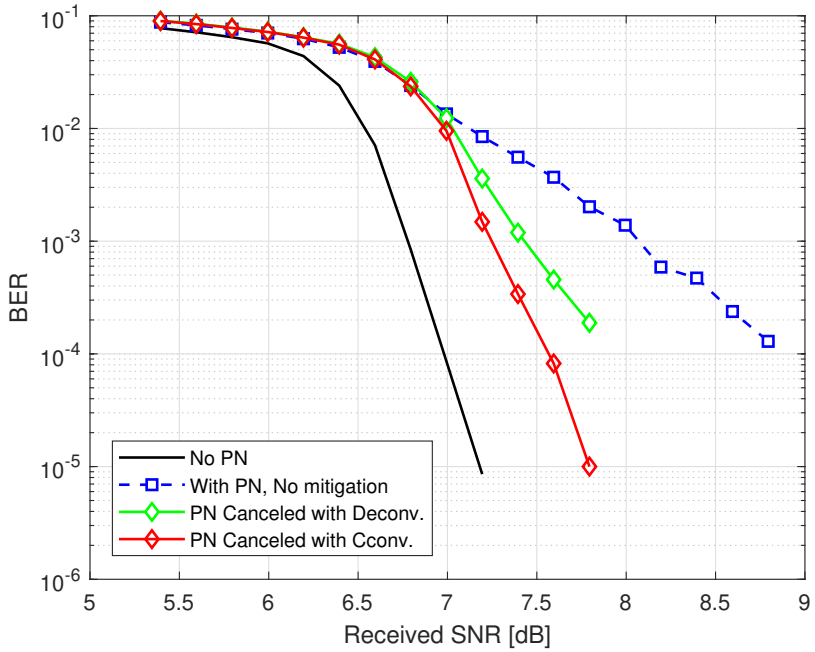

Figure 4-42: BER of LDPC-CP-DFT-s-OFDM. $f_c = 300$ GHz and $d = 6$ m. Coding Rate $= \frac{2}{3}$. $(u = 3, b = 64)$.

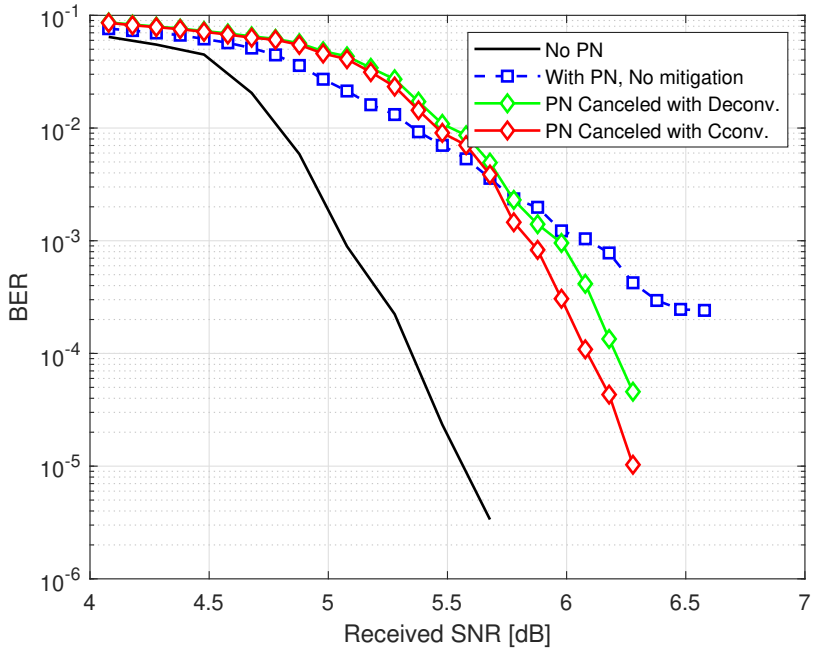

Figure 4-43: BER of LDPC-CP-OFDM. $f_c = 300$ GHz and $d = 3$ m. Coding Rate $= \frac{2}{3}$. $(u = 3, b = 64)$.

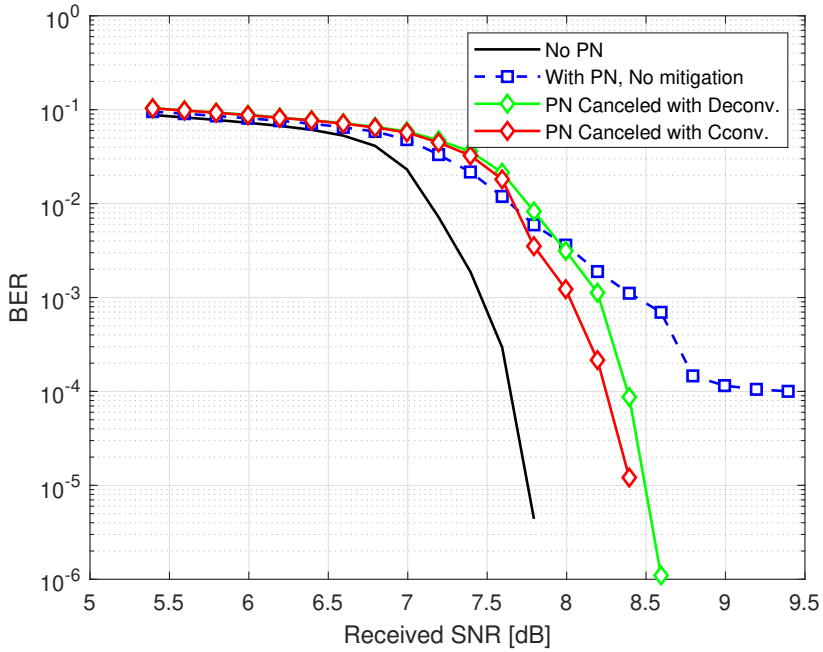

Figure 4-44: BER of LDPC-CP-OFDM. $f_c = 300$ GHz and $d = 6$ m. Coding Rate $= \frac{2}{3}$. $(u = 3, b = 64)$.

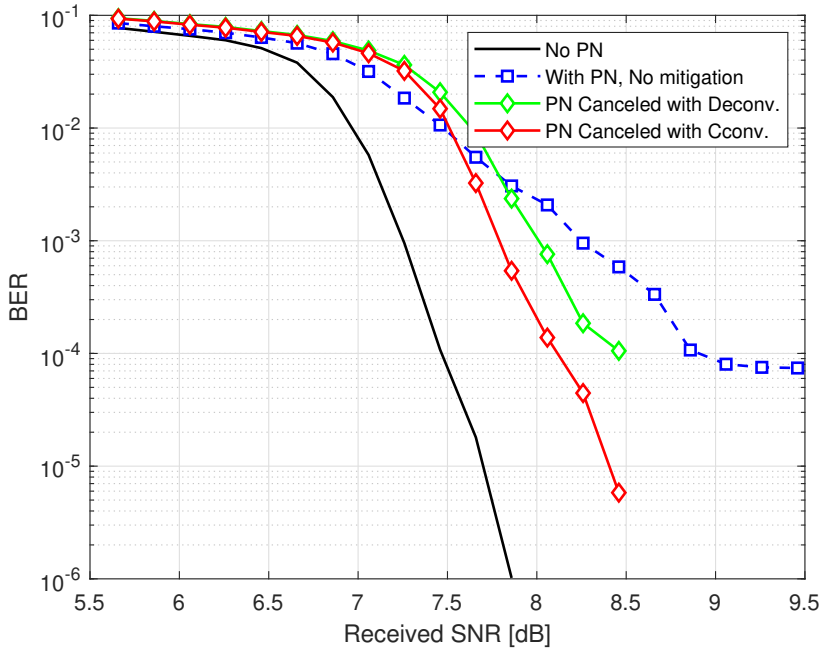

Figure 4-45: BER of LDPC-CP-OFDM. $f_c = 300$ GHz and $d = 10$ m. Coding Rate $= \frac{2}{3}$. $(u = 3, b = 64)$.

the OFDM in several THz channels simulated in this thesis. The main reason is that OFDM lacks frequency diversity which makes it not practical to be used without channel coding in extremely frequency selective channels such as THz channels. On the other hand, DFT-s-OFDM utilizes frequency diversity by its nature explaining the better performance. To confirm this theory a coding rate of $R = 2/3$ was used to compare the BER of OFDM and DFT-s-OFDM. It was observed that the performance gap reduced significantly especially for the channels with higher carrier frequencies (i.e., 0.7 THz) as those channels show more scattering effect. To further investigate this situation, a stronger coding rate of $R = 1/3$ was used. It was seen that in this case, both show a very similar BER meaning that OFDM can catch the performance of DFT-s-OFDM when a strong channel coding is adopted. We also observed that both DFT-s-OFDM and OFDM are affected by diffuse scattering in a THz channel, however, OFDM seemed to be more sensitive to the scattering effect.

The effect of phase noise on both OFDM and DFT-s-OFDM was simulated. It was seen that DFT-s-OFDM shows more resilience to the phase noise effect in terms

of having a lower error floor and in some cases no error floor when PN is very severe. It is apparent that the waveforms in the THz channels have to include some sort of phase noise estimation and compensation technique as the BER of the system when PN is present in the system is very high. This issue is less of a problem in lower band communications systems because they frequency of the local oscillators for those systems is not as high resulting in a much lower phase noise levels. A non-iterative phase noise estimation and compensation method was adopted which is a slightly modified version of the method in [62]. The simulation results showed the better performance of the proposed method in terms of achieving lower BERs for both OFDM and DFT-s-OFDM.

Chapter 5

Conclusion

In this chapter, a short summary of the main conclusions of this thesis are provided. Firstly, a channel model that accurately captures the unique features of THz frequencies was adopted from literature. The channel impulse responses showed that the THz channels suffer a lot from path loss. Unlike the channels in lower frequency bands, THz channels suffer from diffuse scattering as the surfaces appear as rough surfaces in THz frequencies and scatter the incident waves in multiple random directions. Keeping this phenomenon in mind, it is expected that THz channels be extremely frequency selective, especially when the carrier frequency is high and the distance between the transmit and receive antennas and the reflecting objects is very short. The frequency selectivity of the channel suggests that OFDM based waveforms which are widely used in the 4G LTE and 5G NR worth considering and studying for THz. The literature lacks a comprehensive study of OFDM in THz channels that use a correct channel model. Most of the studies are done in sub-THz channels which are not quite the same as THz. As OFDM is known to have a high PAPR, it is worth to compare its performance to other options with lower PAPR find out if higher PAPR is worth it or not. Therefore, this thesis has presented a comprehensive analysis of OFDM and DFT-s-OFDM (which has a much lower PAPR compared to OFDM) performance in THz channels, which can serve as benchmark results for future waveform designs. A simulation based approach was adopted to determine the best CP length as opposed to the conventional way that solely focuses on the maximum delay

spread of the channel. For several THz channels with small RMS delay spread, a CP length of 10% is sufficient. The performance of LDPC-OFDM and LDPC-DFT-s-OFDM has been compared, and for stronger coding like $\frac{1}{3}$ code rate, they show similar BER performance. For higher coding rates such as $\frac{2}{3}$, LDPC-DFT-s-OFDM slightly outperforms LDPC-OFDM due to better utilization of frequency diversity in highly scattered THz channels.

The proposed modified PN estimation and compensation method has shown better results than that in [62]. Overall, DFT-s-OFDM outperforms OFDM in terms of lower PAPR, better BER and more resistant to phase noise in the THz channels simulated in this thesis.

In future research, it would be valuable to investigate the performance of DFT-s-OFDM and single-carrier waveforms in a wider range of THz channel environments, including smaller/larger indoor environments and environments with varying levels of scattering. Furthermore, exploring joint phase noise and channel estimation methods would be beneficial, given the high sensitivity of THz systems to phase noise due to their high carrier frequencies.

Bibliography

[1] Theodore S. Rappaport, Yunchou Xing, Ojas Kanhere, Shihao Ju, Arjuna Madanayake, Soumyajit Mandal, Ahmed Alkhateeb, and Georgios C. Trichopoulos. Wireless communications and applications above 100 GHz: Opportunities and challenges for 6G and beyond. *IEEE Access*, 7:78729–78757, 2019.

[2] Mohammed Aladsani, Ahmed Alkhateeb, and Georgios C. Trichopoulos. Leveraging mmwave imaging and communications for simultaneous localization and mapping. In *ICASSP 2019 - 2019 IEEE International Conference on Acoustics, Speech and Signal Processing (ICASSP)*, pages 4539–4543, 2019.

[3] J. Ma, R. Shrestha, L. Moeller, and D. M. Mittleman. Invited article: Channel performance for indoor and outdoor terahertz wireless links. *APL Photon.*, 3(5):Art. no. 051601, Feb. 2018.

[4] Chong Han. *Physical Layer Solutions for Ultra-broadband Wireless Communications in the Terahertz Band*. PhD thesis, Atlanta GA, 2016.

[5] Technical specification group radio access network; study on supporting NR from 52.6 GHz to 71 ghz (release 17). Tech. Rep. 38.808 Version 2.0.0, 3GPP, Mar. 2021.

[6] Amir Mehdirezaei Khamse, Xiaodai Dong, and Nuwan Ferdinand. The scattering channel model for terahertz wireless communications. *IEEE Open Journal of the Communications Society*, 4:810–822, 2023.

[7] Theodore S. Rappaport, Shu Sun, Rimma Mayzus, Hang Zhao, Yaniv Azar, Kevin Wang, George N. Wong, Jocelyn K. Schulz, Mathew Samimi, and Felix Gutierrez. Millimeter wave mobile communications for 5G cellular: It will work! *IEEE Access*, 1:335–349, 2013.

[8] Alexandros-Apostolos A. Boulogeorgos, Angeliki Alexiou, Thomas Merkle, Colja Schubert, Robert Elschner, Alexandros Katsiotis, Panagiotis Stavrianos, Dimitrios Kritharidis, Panteleimon-Konstantinos Chartsias, Joonas Kokkoniemi, Markku Juntti, Janne Lehtomaki, Antonio Teixeira, and Francisco Rodrigues. Terahertz technologies to deliver optical network quality of experience in wireless systems beyond 5G. *IEEE Communications Magazine*, 56(6):144–151, 2018.

[9] Theodore S. Rappaport, Yunchou Xing, George R. MacCartney, Andreas F. Molisch, Evangelos Mellios, and Jianhua Zhang. Overview of millimeter wave communications for fifth-generation (5G) wireless networks—with a focus on propagation models. *IEEE Transactions on Antennas and Propagation*, 65(12):6213–6230, 2017.

[10] Technical specification group radio access network; study on scenarios and requirements for next generation access technologies (release 15). Tech. Rep. 38.913 Version 15.0.0, 3GPP, Jun. 2018.

[11] Theodore S. Rappaport, Robert W. Heath, Robert C. Daniels, and James N. Murdock. *Millimeter Wave Wireless Communications*. Upper Saddle River, NJ, USA: Prentice-Hall, 2015.

[12] George R. MacCartney and Theodore S. Rappaport. Millimeter-wave base station diversity for 5G coordinated multipoint (CoMP) applications. *IEEE Transactions on Wireless Communications*, 18(7):3395–3410, 2019.

[13] Thomas Kürner and Sebastian Priebe. Towards THz communications - status in research, standardization and regulation. *J. Infrared Millim. THz Waves*, 35(1):53–62, Aug. 2013.

[14] P.H. Siegel. Terahertz technology. *IEEE Transactions on Microwave Theory and Techniques*, 50(3):910–928, 2002.

[15] C. Han I. F. Akyildiz, J. M. Jornet. Terahertz band: Next frontier for wireless communications. *Phys. Commun.*, 12:16–32, Sep. 2014.

[16] Ting Wu, Theodore S. Rappaport, and Christopher M. Collins. Safe for generations to come: Considerations of safety for millimeter waves in wireless communications. *IEEE Microwave Magazine*, 16(2):65–84, 2015.

[17] Guidelines for evaluating the environmental effects of radio frequency radiation. *document FCC 96-326*, Aug. 1996.

[18] International Commission on Non-Ionizing Radiation Protection. Guidelines for limiting exposure to time-varying electric, magnetic, and electromagnetic fields (up to 300 GHz). *Health Physics*, 97(3):257–258, Sep. 2009.

[19] M.J.W. Rodwell, Y. Fang, J. Rode, J. Wu, B. Markman, S. T. Šuran Brunelli, J. Klamkin, and M Urteaga. 100-340 GHz systems: Transistors and applications. In *2018 IEEE International Electron Devices Meeting (IEDM)*, pages 14.3.1–14.3.4, 2018.

[20] M. Tonouchi. Cutting-edge terahertz technology. *Nature Photon.*, 1(2):97–105, 2007.

[21] James F. Harvey, Michael B. Steer, and Theodore S. Rappaport. Exploiting high millimeter wave bands for military communications, applications, and design. *IEEE Access*, 7:52350–52359, 2019.

[22] V. Petrov, D. Moltchanov, and Y. Koucheryavy. Applicability assessment of terahertz information showers for next-generation wireless networks. In *2016 IEEE International Conference on Communications (ICC)*, pages 1–7, 2016.

[23] Gordon E. Moore. Cramming more components onto integrated circuits. *Electronics*, 38(8), Apr. 1965.

[24] R. Kurtzweil. *The Age of Spiritual Machines: When Computers Exceed Human Intelligence*. New York, NY, USA: Penguin Books, 1999.

[25] H. Moravec. When will computer hardware match the human brain. *J. Evol. Technol.*, 1(1):10, 1998.

[26] Huihui Wang and T.S. Rappaport. A parametric formulation of the UTD diffraction coefficient for real-time propagation prediction modeling. *IEEE Antennas and Wireless Propagation Letters*, 4:253–257, 2005.

[27] Ojas Kanhere, Shihao Ju, Yunchou Xing, and Theodore S. Rappaport. Map-assisted millimeter wave localization for accurate position location. In *2019 IEEE Global Communications Conference (GLOBECOM)*, pages 1–6, 2019.

[28] D.M. Mittleman, R.H. Jacobsen, R. Neelamani, R.G. Baraniuk, and M.C. Nuss. Gas sensing using terahertz time-domain spectroscopy. volume 67, page 379–390, Sep. 1998.

[29] Himanshu Aggrawal, Peiyu Chen, M. Mahdi Assefzadeh, Babak Jamali, and Aydin Babakhani. Gone in a picosecond: Techniques for the generation and detection of picosecond pulses and their applications. *IEEE Microwave Magazine*, 17(12):24–38, 2016.

[30] D.M. Mittleman. Perspective: Terahertz science and technology. *Journal of Applied Physics*, 122(23):Art. no. 230901, Dec. 2017.

[31] M. J. W. Rodwell. Sub-mm-wave technologies: Systems, ICs, thz transistors. *Proc. Asia–Pacific Microw. Conf. (APMC)*, pages 509–511, Nov. 2013.

[32] Sai kiran Doddalla and Georgios C. Trichopoulos. Non-line of sight terahertz imaging from a single viewpoint. In *2018 IEEE/MTT-S International Microwave Symposium - IMS*, pages 1527–1529, Jun. 2018.

[33] Shihao Ju, Syed Hashim Ali Shah, Muhammad Affan Javed, Jun Li, Girish Palteru, Jyotish Robin, Yunchou Xing, Ojas Kanhere, and Theodore S. Rappaport. Scattering mechanisms and modeling for terahertz wireless communications. In *ICC 2019 - 2019 IEEE International Conference on Communications (ICC)*, pages 1–7, 2019.

[34] A. Velten, T. Willwacher, O. Gupta, A. Veeraraghavan, M. G. Bawendi, and R. Raskar. Recovering three-dimensional shape around a corner using ultra-fast time-of-flight imaging. *Nature Communications*, 3(745), Mar. 2012.

[35] M. O'Toole, D. B. Lindell, and G. Wetzstein. Confocal non-line-of-sight imaging based on the light-cone transform. *Nature*, 555(7696):338–341, Mar. 2018.

[36] F. Xu, G. Shulkind, C. Thrampoulidis, J. H. Shapiro, A. Torralba, F. N. C. Wong, and G. W. Wornell. Revealing hidden scenes by photon-efficient occlusion-based opportunistic active imaging. *Optical Express*, 26(8):9945–9962, Apr. 2018.

[37] Pawan Setlur, Tadahiro Negishi, Natasha Devroye, and Danilo Erricolo. Multipath exploitation in Non-LOS urban synthetic aperture radar. *IEEE Journal of Selected Topics in Signal Processing*, 8(1):137–152, 2014.

[38] Georgios C. Trichopoulos, H. Lee Mosbacker, Don Burdette, and Kubilay Sertel. A broadband focal plane array camera for real-time THz imaging applications. *IEEE Transactions on Antennas and Propagation*, 61(4):1733–1740, 2013.

[39] Gordon L. Stüber Ye Li. *Orthogonal Frequency Division Multiplexing for Wireless Communications*. Springer New York, NY, 2006.

[40] Behrouz Farhang-Boroujeny and Hussein Moradi. Ofdm inspired waveforms for 5G. *IEEE Communications Surveys Tutorials*, 18(4):2474–2492, 2016.

[41] Hyung G. Myung, Junsung Lim, and David J. Goodman. Single carrier FDMA for uplink wireless transmission. *IEEE Vehicular Technology Magazine*, 1(3):30–38, 2006.

[42] N. Moraitis and P. Constantinou. Indoor channel measurements and characterization at 60 GHz for wireless local area network applications. *IEEE Transactions on Antennas and Propagation*, 52(12):3180–3189, 2004.

[43] Sebastian Priebe, Marius Kannicht, Martin Jacob, and Thomas Kürner. Ultra broadband indoor channel measurements and calibrated ray tracing propagation modeling at THz frequencies. *Journal of Communications and Networks*, 15(6):547–558, 2013.

[44] Ho-Jin Song, Katsuhiro Ajito, Atsushi Wakatsuki, Yoshifumi Muramoto, Naoya Kukutsu, Yuichi Kado, and Tadao Nagatsuma. Terahertz wireless communication link at 300 GHz. In *2010 IEEE International Topical Meeting on Microwave Photonics*, pages 42–45, 2010.

[45] Y. Choi, JW. Choi, and J.M Cioffi. A geometric-statistic channel model for THz indoor communications. *Journal of Infrared, Millimeter, and Terahertz Waves*, pages 456–467, 2013.

[46] Chong Han, A. Ozan Bicen, and Ian F. Akyildiz. Multi-ray channel modeling and wideband characterization for wireless communications in the terahertz band. *IEEE Transactions on Wireless Communications*, 14(5):2402–2412, 2015.

[47] L.S. Rothman *etal*.. The HITRAN 2008 molecular spectroscopic database. *Journal of Quantitative Spectroscopy and Radiative Transfer*, 110(9):533–572, 2009.

[48] J. Jornet and I. Akyildiz. Channel modeling and capacity analysis for electromagnetic wireless nano-networks in the terahertz band. *IEEE Trans. Wireless Commun.*, 10(10):3211–3221, 2011.

[49] R M Goody and Y L Yung. *Atmospheric Radiation: Theoretical Basis*. Oxford University Press, 1989.

[50] Peter Beckmann and Andre Spizzichino. *The Scattering of Electromagnetic Waves From Rough Surfaces*. Artech House Publishers, 1987.

[51] R Piesiewicz and et al. Scattering analysis for the modeling of THz communication systems. *IEEE Trans. Antennas Propag.*, 55(11):3002–3009, 2007.

[52] Christian Jansen, Sebastian Priebe, Christoph Moller, Martin Jacob, Hanno Dierke, Martin Koch, and Thomas Kurner. Diffuse scattering from rough surfaces in THz communication channels. *IEEE Transactions on Terahertz Science and Technology*, 1(2):462–472, 2011.

[53] Martin Jacob, Sebastian Priebe, Robert Dickhoff, Thomas Kleine-Ostmann, Thorsten Schrader, and Thomas Kurner. Diffraction in mm and sub-mm wave indoor propagation channels. *IEEE Transactions on Microwave Theory and Techniques*, 60(3):833–844, 2012.

[54] Hong-Chuan Yang. *Introduction to Digital Wireless Communications*. Institute of Engineering and Technology, London, United Kingdom, 2017.

[55] John G. Proakis and Masoud Salehi. *Digital Communications 5th ed.* McGraw-Hill, Boston, USA, 2008.

[56] A. Mehrotra A. Demir and J. Roychowdhury. Phase noise in oscillators: a unifying theory and numerical methods for characterization. *IEEE Trans. Circuits Syst. I, Fundam. Theory Appl.*, 47(5):655–674, 2000.

[57] W. Rave D. Petrovic and G. Fettweis. Effects of phase noise on OFDM systems with and without PLL: Characterization and compensation. *IEEE Transactions on Communications*, 55(8):1607–1616, 2007.

[58] D.B. Leeson. A simple model of feedback oscillator noise spectrum. *Proceedings of the IEEE*, 54(2):329–330, 1966.

[59] Theodore S Rappaport. *Wireless communications: Principles and practice, second ed.* Pearson Education India, 2010.

[60] Technical specification 5G NR multiplexing and channel coding. TS 38.212 version 16.2.0 Release 16, 3GPP, Jun. 2020.

[61] F. Egan William. *Practical RF System Design*. John Wiley Sons, Inc., 2003.

[62] Ville Syrjälä, Toni Levanen, Tero Ihalainen, and Mikko Valkama. Pilot allocation and computationally efficient non-iterative estimation of phase noise in OFDM. *IEEE Wireless Communications Letters*, 8(2):640–643, 2019.